New Measurement Approaches to the Study of Secondary Organic Aerosol

by

Erik Helstrom

B.A. Physics, Columbia University, 2018

Submitted to the Department of Civil and Environmental Engineering
in partial fulfillment of the requirements for the degree of
DOCTOR OF PHILOSOPHY IN ENVIRONMENTAL CHEMISTRY
at the

MASSACHUSETTS INSTITUTE OF TECHNOLOGY

May 2025

Authored by: Erik Helstrom
Department of Civil and Environmental Engineering
May 9th, 2025

Certified by: Jesse H. Kroll
Peter de Florez Professor of Civil and Environmental Engineering, Professor of Chemical Engineering, Thesis supervisor

Accepted by: Heidi Nepf
Donald and Martha Harleman Professor of Civil and Environmental Engineering
Chair, Graduate Program Committee

New Measurement Approaches to the Study of Secondary Organic Aerosol

by
Erik Helstrom

Submitted to the Department of Civil and Environmental Engineering
on May 9, 2025 in partial fulfillment of the requirements for the degree of
DOCTOR OF PHILOSOPHY IN ENVIRONMENTAL CHEMISTRY

ABSTRACT

Aerosol particles constitute a class of atmospheric pollutants that are detrimental to human health and influence the Earth's climate. A significant fraction of aerosol mass is composed of organic material, produced by photochemical reactions of organic trace gases which form secondary organic aerosol (SOA). However, the large diversity of volatile organic compounds (VOCs) makes it challenging to identify all of the chemical reactions contributing to SOA formation. In addition to this chemical complexity, our ability to identify and measure all of the relevant organic compounds, especially species present in aerosol particles, is limited by challenges in efficiently sampling and detecting the various classes of molecules formed. Improving knowledge of the chemical behavior of aerosol will improve our ability to predict how changing emissions and chemical conditions will impact the formation and properties of particulate matter in the future.

This thesis will explore recent improvements in instrumentation and measurement techniques and apply them to laboratory studies of organic carbon and SOA. First, we adapt a technique for measuring total suspended carbon to laboratory chamber experiments, converting organic compounds with high temperature catalysis to carbon dioxide, which is then monitored in real time. This allows for a "top-down" constraint on the overall concentration of all organic species (including SOA) as experiments proceed, as some lower volatility products are lost to the surfaces of the laboratory chamber. Second, we compare the measurements of SOA from three chemical ionization mass spectrometers using different ionization and desorption methods to detect particle-phase species. Clear differences emerge in the detected formulas across instruments, highlighting variations in chemical sensitivities to different classes of compounds and the influence of fragmentation on the detected products. Finally, we explore how changing peroxy radical fate influences SOA formation by monitoring SOA composition with extractive electrospray ionization (EESI) mass spectrometry. Differences in particle-phase products, particularly nitrates, hydroperoxides, and dimers, make the dependence of initial SOA composition on peroxy radical pathways clear. Over time, we observe a convergence of SOA spectra formed under different peroxy radical regimes, suggesting the influence of secondary products and particle-phase chemistry, though some differences persist from the initial gas-phase peroxy radical fate. Overall, this thesis demonstrates improved tools for constraining and investigating VOC oxidation pathways leading to particle-phase organic species.

Thesis supervisor: Jesse H. Kroll
Title: Peter de Florez Professor of Civil and Environmental Engineering, Professor of Chemical Engineering

Acknowledgements

I would first like to thank Jesse Kroll, my advisor, for all the enthusiasm and expertise which I have enjoyed during my time in graduate school. Without his direction, it would not have been possible for me to gain both the technical proficiency and multi-disciplinary knowledge necessary to conduct research in organic atmospheric chemistry. I have greatly benefited from Jesse's mentorship and teaching, which both really allowed me to explore different problems in laboratory studies and always directed me towards useful questions and approaches, no matter how inconclusive or disoriented I felt my results looked at any given moment. I would also like to thank the members of my dissertation committee, Professors Colette Heald and Arlene Fiore. Their generous input and guidance helped to shape the directions of my research and to situate this thesis in a broader context. Without the time I spent working with Arlene prior to this PhD, I would not have found my way to atmospheric chemistry in the first place.

I could not have finished the work in this dissertation without the support of all of the members of the Kroll Group who I was fortunate to interact and collaborate with over the years: David Hagan, Mark Goldman, Josh Moss, Amanda Gao, Matthew Goss, Lesly Franco, Nadia Tahsini, Lexy LeMar, Seamus Frey, Isabel Albores, Drew Meyers, Will Sharpe, Kevin Nihill, Qing Ye, Tori Barber, Amy Hrdina, Hannah Kenagy, and Jia Jiang. Their expertise and assistance was essential to the smooth operation of the laboratory experiments described here. I would like to thank both Joy Domingo-Kame'enui and Steph Elkins, with whom I had the opportunity to explore various reactive nitrogen experiments. I would also like to thank the members of the Heald group who greatly contributed to my understanding of the atmosphere outside of the laboratory setting: Sid Pai, Tess Carter, Ishir Dutta, Olivia Norman, and Joe Palmo. I would like to thank the many scientists at Aerodyne Research Inc. who aided me in the operation of many of the instruments, particularly Manjula Canagaratna, Jordan Krechmer, and Anita Avery, whose patience with troubleshooting the EESI-ToF-MS finally enabled us to obtain a promising dataset. Similarly, I am indebted to Yaowei Li and Alex Zaytsev, who spent considerable time assisting in the operation and maintenance of the PTR instrument used in many chamber experiments during their time as graduate students in Frank Keutsch's group at Harvard. I would like to thank Abby Koss, who conducted the experiments analyzed in Chapter 3 before I even began my graduate studies. Finally, I want to thank the community at Parsons laboratory who have all fostered a friendly and social environment over the years.

Finally, I would like to thank all of my friends and family members, from those here in Boston to the ones scattered overseas, whose energy and support enriched and sustained me through this period of my life, and to whom I am endlessly grateful.

Contents

List of Figures

List of Tables

Chapter 1: Introduction

1.1 The chemistry of organic compounds in the atmosphere

The atmosphere is a chemically reactive environment whose local properties are determined by the presence of trace compounds. Two classes of compounds, ozone and aerosol particulate matter, have been recognized for their contribution to poor air quality since the identification of smog formation from emissions of volatile organic carbon species (VOCs) and nitrogen oxides (NO_x, $NO+NO_2$) (Haagen-Smit, 1952). Exposure to high concentrations of ambient aerosol is the most significant environmental risk factor for premature death worldwide (Landrigan et al., 2018; Pozzer et al., 2023). Aerosols and ozone are also climate forcers, influencing the balance of incoming UV and outgoing thermal radiation passing through the atmosphere (Fishman et al., 1979; Charlson et al., 1990; Pöschl, 2005). Decades of study investigating the processes controlling ozone and aerosol abundance have revealed a complex, multiphase, nonlinear system. Most reactions in the atmosphere are driven by the chemistry of radicals, which are generated by sunlight, combustion processes, and lightning (Anderson, 1987). Accurately describing the properties of this system and determining its sensitivity to changes in the biosphere, anthropogenic emissions, and the climate is essential for making projections of future atmospheric composition and its effects on society and ecosystems.

The chemistry of reactive organic carbon (ROC) is crucial for the overall reactivity of the atmosphere, and has controlling influences on both ozone and aerosol chemistry (Heald & Kroll, 2020). Organic emissions from the biosphere are ubiquitous, and many other classes of organic molecules are emitted during fossil fuel exploitation and the use of volatile chemical products. Once emitted, carbon-containing molecules undergo oxidation reactions with atmospheric radicals. This involves breaking higher energy carbon-hydrogen bonds or carbon-carbon bonds which are reformed as more stable carbon-oxygen bonds. The furthest extent of oxidation for a given carbon atom results in carbon dioxide. Though a substantial amount of carbon dioxide is formed from organic molecules in the atmosphere (Safieddine et al., 2017), much of the carbon in the atmosphere is instead removed by deposition (Bi & Isaacman-VanWertz, 2025). Many oxidation reactions facilitate the sequential addition of oxygen, as well as other inorganic atoms including nitrogen, sulfur, and chlorine. When these reactions proceed faster than fragmentation of the carbon skeleton, the resulting larger molecular structures and functional groups increase the polarity of the compound, lowering its volatility. The lowest volatility multifunctional products then deposit onto surfaces or condense into particles, generating secondary organic aerosol (SOA) pollution.

A key branching point in the oxidation of organic compounds is the fate of the peroxy radical (RO_2). The most prevalent oxidant in the atmosphere is the hydroxyl radical, OH (Orlando & Tyndall, 2012). ROC reactions with OH produce alkyl radicals, formed by the breaking of a chemical bond, which leaves a reactive open electron site. This is rapidly followed by the addition of gaseous oxygen (O_2), producing a peroxy radical (Atkinson, 1986). Peroxy radicals then can react bimolecularly with nitric oxide (NO), the hydroperoxyl radical (HO_2), cross reactions with other peroxy radicals, and nitrogen dioxide (NO_2). Some can undergo isomerization reactions, a

unimolecular rearrangement that produces a secondary alkyl and then peroxyl radical (Peeters et al., 2009). Figure 1.1 illustrates the RO_2 formation pathway and branching ratios leading to oxidized VOCs and SOA, which can react again to generate later generational products. The chemical formulas of the products from these different RO_2 pathways will differ, and the relative rates of these pathways rates will depend on the relative oxidant concentrations for a given air parcel. Therefore, the overall rates of SOA formation, as well as SOA composition, are likely to be impacted by oxidation conditions of the peroxy radicals.

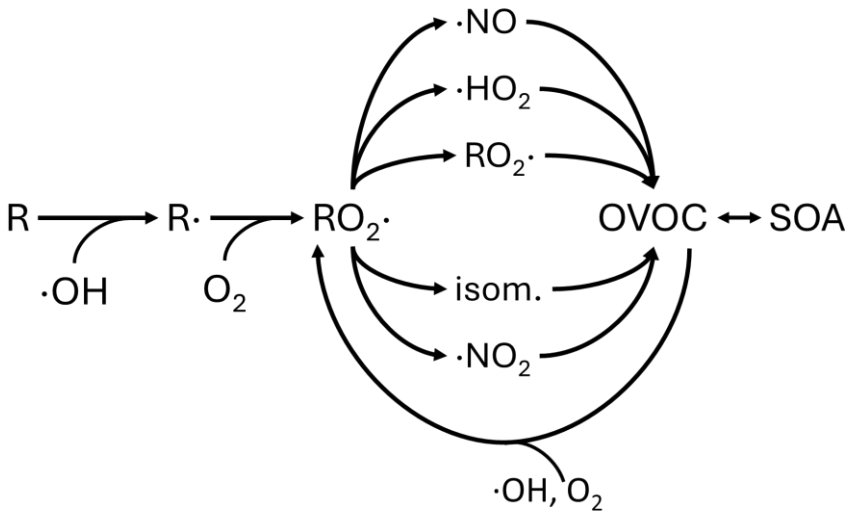

Figure 1.1: Schematic of VOC Oxidation

1.2 Laboratory measurements of organic carbon

Studies of reactive organic carbon in the laboratory provide the opportunity to isolate key reaction pathways and identify trends in chemical behavior. This has been accomplished by focusing on characteristic ROC systems, such as the most common biogenic and anthropogenic emissions, which may be generalized to represent chemistry of the atmosphere in model simulations. Laboratory studies have been traditionally performed to characterize the overall yield of carbon converted from an organic precursor to SOA. Because the composition of the aerosol also determines its toxicity and radiative impacts, and may indicate the chemical formation pathways producing SOA, more recent studies have attempted to identify specific particle-phase products. It has been estimated that there may be hundreds of thousands of organic species in the atmosphere, with a wide range of chemical behavior that eludes comprehensive measurement. Therefore, "carbon closure" experiments have also been attempted to assess current instrumentation's ability to track the evolution of organics through different stages of oxidation (Isaacman-VanWertz et al., 2017, 2018).

Measurements of atmospheric composition have to overcome the challenge of detecting trace levels of many different species, which also span a wide range of chemical properties. The most broad type of chemical measurements are elemental analysis techniques, where a property such as the total concentration of carbon is measured with no chemical specificity (Roberts et al., 1998; Maris et al., 2003). For identification of specific chemical pathways, online techniques are

highly valuable for monitoring the impact of atmospheric chemical processes with high time resolution, often occurring on a timescale of minutes to hours. Certain gas-phase species, such as ozone, NO_x, and CO_2 can be detected by gas analyzers, which quantify analyte concentrations by measuring the decrease in infrared light transmitted through a sampling cell due to interference of that species. Mass spectrometry techniques, which measure analytes by converting them to ions, ordering them by mass via manipulation through electric fields, enable versatile compositional measurements of a wide range atmospheric molecules. Time of flight mass spectroscopy has greatly increased the mass resolving power necessary to distinguish formulas with the same nominal masses (Junninen et al., 2010). The ability to ionize a given molecule determines how efficiently it will be detected with a mass spectrometer. Furthermore, higher energy techniques such as electron ionization tend to fragment the analytes sampled, prohibiting direct identification of the chemical formulas being measured. Chemical ionization mass spectrometry (CIMS) techniques manipulate ion-adduct chemistry to lower fragmentation rates and have permitted the direct detection of molecular species (Bertram et al., 2011). A proliferation of different ionization methods expanded the range of compounds which could be detected, including multifunctional, more oxidized, and intermediate- and lower-volatility species (Ehn et al., 2012; Lee et al., 2014a). Figure 1.2 (reproduced from Heald & Kroll, 2020) illustrates the increasing coverage of measurements over time with the expansion of available instrumentation.

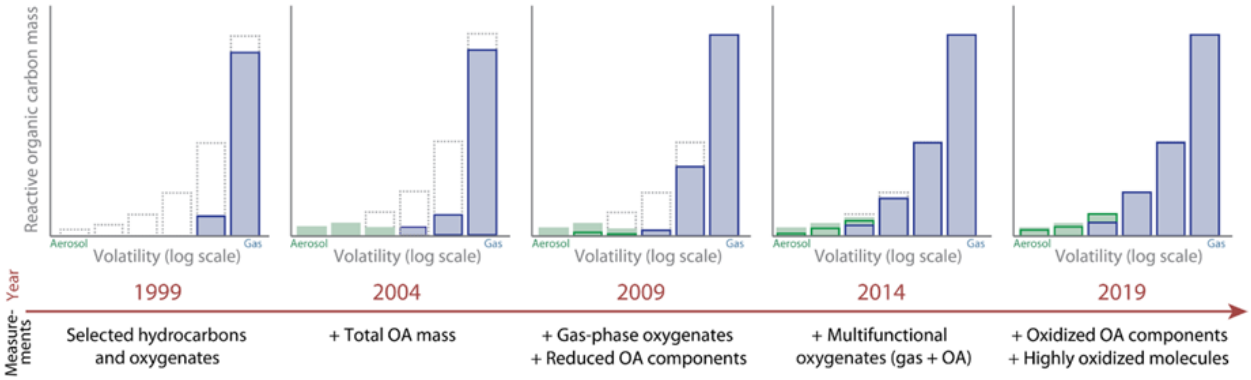

Figure 1.2: Timeline of available measurement coverage of different classes of reactive organic carbon species, classified by volatility. Reproduced from Heald & Kroll, 2020.

For aerosol composition, offline measurements have long been used for probing aerosol properties and mass loadings. This involves a filter collection followed by either gas chromatography or elemental analysis to characterize the particles (Johnson et al., 1981; Chow, 1995; Solomon & Sioutas, 2008). For mass spectrometric measurements of aerosols, the aerosol mass spectrometer (AMS) has been used to great effect in advancing online measurements of aerosol composition (DeCarlo et al., 2006). AMS measurements have been meticulously characterized with aerosol standards, enabling bulk aerosol quantification and speciation. However, the electron ionization method used in the AMS results in high fragmentation and cannot characterize individual products. This limitation motivated the adaptation of CIMS techniques to measurements of aerosol particles. Thermal desorption techniques have been coupled to CIMS in order to sample particle-phase species directly, though the high temperatures

involved can induce fragmentation of some species during vaporization (Lopez-Hilfiker et al., 2014; Eichler et al., 2015). Finally, techniques such as electrospray ionization have been used to further limit the impact of thermal fragmentation (Lopez-Hilfiker et al., 2019). Different particle CIMS instruments, implementing a variety of source ions, have been able to measure a wide range of organic species, but have not been as extensively characterized for measurements of the particle phase as for the gas phase.

Despite the advancements which have been made in atmospheric measurements, important gaps remain in our understanding of the oxidation systems commonly investigated in the laboratory. Though a complete accounting of carbon from precursor to a mixture of products has been achieved in chamber experiments, complications from deposition to the chamber walls are known but poorly constrained. Speciated measurements of aerosol species have greatly enhanced knowledge of the composition of SOA, but the comprehensiveness of these techniques, which are chemically selective, has not been thoroughly investigated for potential biases in the classes of aerosol which are detected. Lastly, while many studies of the formation, composition, and properties of aerosol have been conducted, there has been little systematic exploration of the impacts of gas-phase oxidation conditions on the identities of SOA components, especially with respect to conditions where multiple peroxy pathways are competitive.

1.3 Thesis Outline

This thesis will explore recent improvements in instrumentation and measurement techniques. It will assess their implications for laboratory and studies of the chemistry of organic carbon, focusing and applying some of these advances to characterize measurements of SOA composition, and connect particle-phase composition to the chemistry of peroxy radicals in the gas phase.

In Chapter 2, we adapt a technique for measuring total carbon to laboratory chamber experiments, which lack direct constraints on carbon losses to walls and surfaces. We use the principle of high temperature catalysis to rapidly convert reactive organic carbon into carbon dioxide, which is then compared to a reference measurement. This is a straightforward way to quantify the overall levels of carbon present in a system. The low levels of background carbon dioxide make it easier to measure the quantities of carbon typically studied in a laboratory setting. The high time resolution of this measurement additionally enables us to identify changes in the amount of carbon dioxide lost to surface deposition, and the mineralization to carbon dioxide from extended amounts of oxidation.

In Chapter 3, we compare the simultaneous measurements of multiple particle-phase chemical ionization mass spectrometers during chamber oxidation experiments in order to evaluate the relative differences in detection of individual SOA compounds. These comparisons assess the chemical identities detected in different instruments that can be determined from their chemical formulas. They identify overlaps between the particle-CIMS measurements, as well as key differences in the relative distributions of each instrument signal, with some ionization schemes favoring specific classes of products. These differences arise due to selectivity and fragmentation processes specific to the ionization and desorption methods used. Lastly, each

of the SOA measurements are compared with the more established but chemically nonspecific aerosol mass spectrometer, and relevant applications of different particle CIMS techniques are discussed.

In Chapter 4, we apply another novel method for measuring particle-phase species, Extractive Electrospray Ionization (EESI) mass spectrometry, to investigate the impacts of oxidation conditions on the composition of SOA from α-pinene, a common biogenic precursor. The series of experiments conducted span a range of oxidation conditions to vary RO_2 pathways. Specific product formulas measured in the SOA imply the influence of specific RO_2 pathways consistent with explicit chemical modeling of the RO_2 fates in illustrative experiments. Differences in particle composition across all experiments allow identification of trends in the behavior of atmospheric oxidation. The evolution of SOA composition as oxidation proceeds indicates increasing similarities in the products detected across experiments, but with some key features persisting. These results show that when adapting a simplified mechanism of SOA formation chemistry in earth system models, competition between multiple RO_2 fates, rather than a paradigm which assumes linear competition of NO with HO_2, will more accurately reproduce the chemistry of intermediate chemical regimes.

In conclusion, this series of studies demonstrates the importance of developing and characterizing chemical measurements for the study of aerosol chemistry and organic reactivity. They identify important metrics for assessing the performance of specific measurement techniques and expand the range of conditions to be considered upon designing future studies of organic photooxidation by demonstrating the ability to monitor differences in composition in those different chemical regimes. These advances will assist in the development of more precise investigations of atmospheric processes, leading to better parameterizations of aerosol formation and its properties.

Chapter 2: Development of a Total Suspended Carbon Instrument for Use in Laboratory Studies

2.1 Chapter Abstract

The oxidative processing of reactive organic carbon (ROC) involves a very large number of unique species. Measurements of an increasing range of organic compounds have improved our picture of the overall presence of ROC and its oxidation products in the atmosphere. However, in spite of this progress within the laboratory towards a complete accounting of the transformation of all precursor carbon, or carbon closure, the quantification of loss processes to the walls of the chamber remains incomplete. In order to measure total suspended carbon in chamber experiments, we adapt a "total carbon" technique originally developed by Veres et al., 2010 for calibration of field instruments. This measurement is performed by combining high temperature platinum and palladium catalysts to fully oxidize ROC to CO_2, followed by a differential CO_2 measurement to quantify the total carbon content. Here we characterize this setup (the "Oxycat") in detecting a range of gas- and particle-phase carbon-containing species over a range of relevant concentrations. Furthermore, we demonstrate the incorporation of the Oxycat in estimating wall loss from oxidation of ROC, the evolution of total suspended carbon over time, and the formation of secondary CO_2. The addition of this top-down carbon measurement provides a valuable constraint towards the quantification of wall loss and the assessment of the remaining gaps and overlaps between different ROC measurements.

2.2 Introduction

Organic compounds are key to the reactive chemistry of the atmosphere (Heald & Kroll, 2020). They undergo oxidation reactions to form pollutants such as secondary organic aerosols (SOA), which determine air quality and have important implications for the radiative budget of the atmosphere. Exposure to high concentrations of pollutants such as aerosols have important implications for human health. Aerosols scatter and absorb light, which combined with their impact on the formation of clouds influences the energy balance and climate of the earth. There is also an estimated 1300 TGs of carbon dioxide produced from the oxidation of methane and other reactive organic carbon (ROC) species in the atmosphere, making it a secondary source of atmospheric CO_2 (Safieddine et al., 2017).

Quantification of ROC compounds and their influence on the chemistry of the atmosphere is a difficult problem to resolve due to the large number of species that are emitted from a variety of sources (Goldstein & Galbally, 2007). Key emissions and their major oxidation products have been identified for some time, but there remain major gaps to a comprehensive understanding of all compounds present in the atmosphere (Isaacman-VanWertz et al., 2017). Major improvements have been made in the detection of oxidized products, but these can still be lost to the walls of sampling lines if they are low enough in volatility. Furthermore, it is not feasible to make measurements of all species that are quantified by calibration of authentic standards. Chemical ionization mass spectrometers, which are essential for measuring large classes of organic compounds, have highly variable calibration sensitivities resulting from the selectivity of

ion-adduct chemistry. One approach to characterizing reactive carbon in the atmosphere is to measure total organic carbon content by combining measurements from multiple instruments, whose sensitivities cover different classes of compounds. Studies creating a total carbon budget from multiple instruments have been performed in the laboratory and ambient environments (Hunter et al., 2017; Isaacman-VanWertz et al., 2018; Price et al., 2019), and syntheses of multiple studies have been used to constrain variation in reactive organic carbon on a regional scale (Heald et al., 2008).

When attempting to monitor the evolution of all organic carbon species in a laboratory chamber experiments, the impacts of deposition of low volatility species to the walls of the Teflon chamber and to the instrument sample line tubing must be considered. Losses of compounds to walls and sampling lines can serve as either a sink or a reservoir for species which will remain undetected while deposited. Some species may be volatilized at a later time after the phase equilibrium shifts, or products of photolytic or surface chemistry may be formed and emitted. This will influence the yields determined by chamber studies of SOA formation and potentially introduce contamination to the background concentrations in subsequent experiments. There have been a number of attempts at constraining the overall impact of chamber walls by measuring the loss rates of standard compounds (Yeh & and Ziemann, 2015) and oxidized products (J. E. Krechmer et al., 2016), as well as with varying aerosol loading (Nah et al., 2017) and temperature (L. He et al., 2024). However, these systems are not comprehensive and may not fully describe wall loss processes of the entire oxidation system or the variation between specific chambers.

Total observed organic carbon estimates from multiple instruments can constrain the budget of radical organic carbon from the “bottom-up”. In contrast, a “top-down” approach to measuring total organic carbon can help constrain this budget by making a single, chemically nonspecific measurement. Early studies which measured total carbon content converted reactive organic species to carbon dioxide and then methane, before measuring the concentration with a flame ionization detector (Roberts et al., 1998; Maris et al., 2003). Veres et al., 2010 adapted this technique to a carbon dioxide gas analyzer, simplifying the steps involved to only require oxidation to CO_2. Yang & Fleming, 2019 then applied this technique to sample ambient air at a monitoring station alongside a speciated measurement. More recently, this technique has been applied to ambient measurements of emissions from tar sands operations, wildfire plumes, and deposition rates (Hayden et al., 2022; M. He et al., 2024; K. Li et al., 2024; Liggio et al., 2025). Other catalyst based elemental analyses have been applied to nitrogen (Stockwell et al., 2018) chlorine (Furlani et al., 2023), and fluorine (R. Ye et al., 2024). Application of this measurement to a chamber has been performed, but mainly to quantify initial concentrations of total hydrocarbons (K. Li et al., 2021). To our knowledge, this approach to measuring total suspended organic carbon has never been used to monitor evolving TOC concentrations over the course of a laboratory study.

Here we apply the technique of combining high temperature catalysis with an optical CO_2 measurement to laboratory chamber studies in order to quantify total suspended carbon in real time. This instrument, the “OxyCat”, allows for monitoring of the introduction of total carbon at the beginning of an experiment, as well as continuous tracking of the transformed carbon in the

chamber, which is expected to decrease due to dilution, conversion from organics to CO and CO_2 ("mineralization"), and partitioning of semi-volatile and low volatility species. The total carbon measurement therefore can aid in determinations of overall carbon closure and estimations of wall loss processes, whose characterization is essential to calculating aerosol yields and accurately describing the behavior of the ROC system.

2.3 Methods

A visualization of the components of the setup is shown in Figure 2.1. The technique converts ROC to CO_2 and then detects the enhancement above background CO_2 concentrations, following the approach by Veres et al., 2010 for verifying concentrations of gas standard calibrants at parts-per-million Carbon (ppmC) levels. We sample air through a packed platinum and palladium catalyst (Shimadzu) in a gas purifier furnace (Supelco). After passing through a cooling coil, the CO_2 formed is measured by the differential CO_2/H_2O analyzer (LI-7000, LiCor). The LI-7000 measurement is based upon attenuation of the infrared signal, which is sensitive to oxygen gas, water vapor, and CO_2, as well as the temperature and pressure of the two cells. After subtracting for the differential attenuation due to O_2 (assumed to be at atmospheric concentrations) and H_2O, the analyzer calculates the concentration present in both the reference and sample cells at 5Hz resolution. The difference in CO_2 between the two cells then provides a measurement of total suspended carbon content. Particle filters are placed in front of both cells to prevent interference from particulate matter sampled in the reference line.

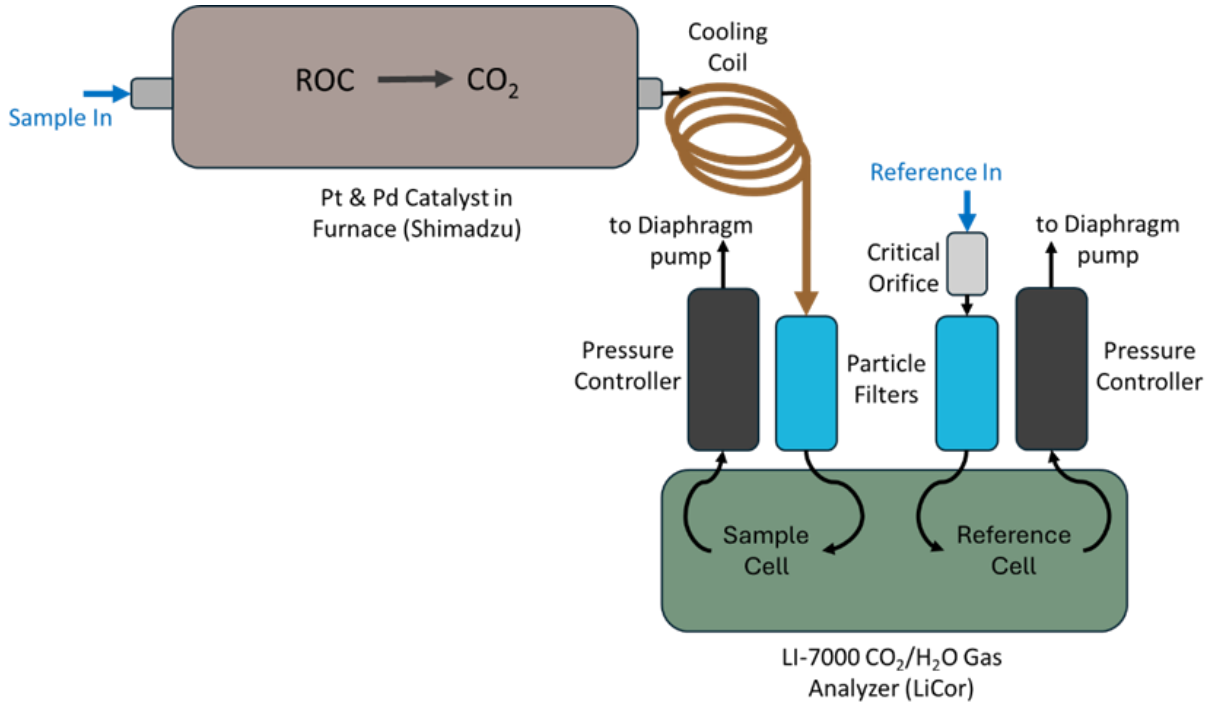

Figure 2.1: Schematic of components of oxycat setup. ROC is sampled and converted to CO_2 by passing through a 600C catalyst, followed by a CO_2 gas analyzer. Pressure is controlled directly downstream of the measurement. Air is continually sampled through both cells by a pump.

One challenge posed by the specific gas analyzer implemented is that although the pressure of the gas sampled in each optical cell is necessary for determining the CO_2 concentration, only a single pressure sensor calculates this parameter, which is applied to both cells. The high temperature region of the catalyst creates a local pressure high which limits flow downstream to the CO_2 instrument. In order to regulate the pressure between both cells as closely as possible, two pressure controllers were placed immediately downstream of the instrument outputs, which use solenoid valves to restrict available flow to the backing pumps. A critical orifice was used to constrict the flow through the reference line in a comparable manner to the catalysis line. This created equal flow and pressure conditions in both cells, limiting the differential delay in detecting changes of CO_2 and TOC caused by differing flow rates.

Calibration of the span of the instrument is stable for many years of continuous measurement. However, the zero point of the instrument tends to drift by up to a few ppm CO_2, and so recalibration of the analyzer with an ultra-zero air (UZA) standard was essential for resetting the zero point. This is carried out by flowing a constant stream through a mass flow controller from a UZA calibration standard tank to both the reference and sample lines. The UZA overflow is open to a vent line in order to avoid pressurizing the gas analyzer. The zero point is adjusted with the LI-7000 after CO_2 concentrations stabilize, usually on a scale of 10-20 minutes. TOC is then calculated from the difference between the catalyst sampling cell and the reference cell.

In order to characterize the response of the total carbon measurement, we calibrate the TOC measured by the OxyCat when sampling different reactive carbon species: carbon monoxide (CO), α-pinene ($C_{10}H_{16}$), isoprene (C_5H_8), 1-butanol ($C_4H_{10}O$), and levoglucosan ($C_6H_{10}O_5$). Each compound was introduced into a 150 L Teflon chamber at high parts-per-billion Carbon (ppbC) concentrations. As the compound was diluted by replacement flow from a zero-air generator, the decay in concentration was sampled by the OxyCat and a chemically specific measurement when available. CO was introduced by continuous flow from an analytical standard cylinder. α-pinene (98% purity), isoprene (99.5% purity), and 1-butanol (99.9% purity), calibrations were introduced by liquid injection gas-tight syringe. A proton transfer reaction-mass spectrometer (PTR3), calibrated to a standard solution of these 3 VOCs, sampled these compounds. Levoglucosan is a particle-phase standard, so a 150 g/L solution dissolved in water was flowed through an atomizer and then a dryer to produce particles in the chamber, which were additionally sampled by a scanning mobility particle sizer (SMPS).

Laboratory chamber experiments were performed with the OxyCat to test how the measurement monitors the evolution of ROC. In one experiment, ozonolysis was used to convert α-pinene into oxidized products and generate SOA. This was done by introducing ammonium sulfate seed aerosols to serve as surface area for SOA to condense on, followed by a gas syringe injection of α-pinene, and then the generation of ozone by UV photolysis of oxygen with a mercury lamp. Other experiments used the Oxycat to probe the evolution of VOCs in the presence of commercial air cleaners (Q. Ye et al., 2021). In these experiments, limonene and toluene were added to the laboratory chamber, and an air cleaner placed within the chamber was operated, while concentrations of gas- and particle-phase species were monitored with a suite of mass spectrometers. Lastly, in order to observe the evolution of ROC over long oxidation

exposures, chamber experiments with isoprene were conducted in which UVC lights were used to generate high concentrations of OH from photolysis of ozone in the presence of water vapor. In all experiments, the OxyCat TOC measurement was directly sampling from the chamber.

2.4 Results and Discussion

2.4.1 TOC Standard Calibrations

Figure 2.2a and 2.2b show the decay curve of the TOC signal corresponding to carbon monoxide and the estimation of the expected concentration resulting from constant dilution of the chamber. Figure 2.2c plots a calibration curve of these two timeseries, averaged over every 2 minutes. The vertical error bars represent the 95th percentile estimation of the TOC measurement arising from variation in the background TOC concentration, which can be seen to fluctuate over a period of 20-40 minutes. At high concentrations up to 1000 ppbC, there is close agreement between the reference standard and the total carbon content detected within the error bars introduced. The limit of detection of the instrument is shown to be around 50-100 ppbC due to the drift in the zero point of the estimation. Below these concentrations, the uncertainty of the TOC background caused by instrument fluctuations from the CO_2 analyzer obscures any signal from CO. This low frequency noise is the primary limitation on a more precise estimation of TOC levels.

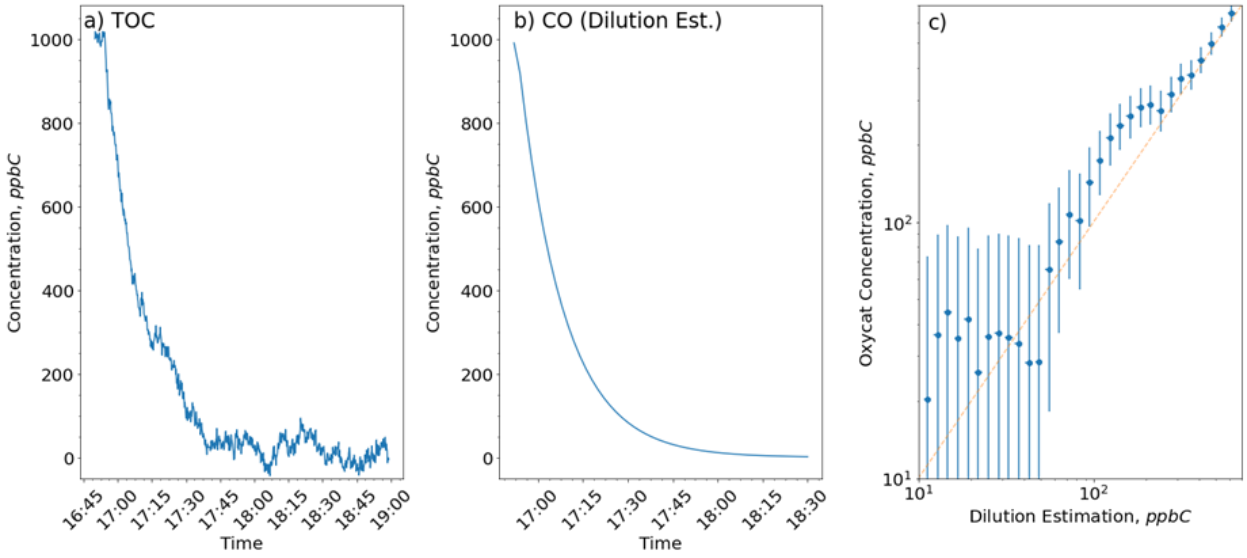

Figure 2.2: Carbon monoxide calibration a) timeseries of TOC signal decay, b) dilution estimation of the CO concentration, and c) calibration curve.

Figures 2.3, 2.4, and 2.5 show the calibration timeseries and calibration curves for α-pinene, isoprene, and 1-butanol respectively. The α-pinene timeseries detected in the PTR shows a good agreement with the TOC estimation. This results in a linear calibration curve from 100-500 ppbC, with the fluctuations in the background TOC estimation again obscuring quantification of concentrations below 50-100 ppbC. The isoprene and 1-butanol TOC calibrations are also well matched by the timeseries behavior of the PTR reference measurement. For these compounds, a combination of low reference instrument signal and uncertainty in calibration of the reference

instrument leads to a discrepancy in the accuracy of the TOC instrument. The likely source of the disagreement between PTR measurements of isoprene and concentrations of TOC detected is inaccuracies in the calibration of the PTR reference measurement. However, semi-volatile species which might partition to the sampling lines before reaching the catalyst should be more thoroughly investigated.

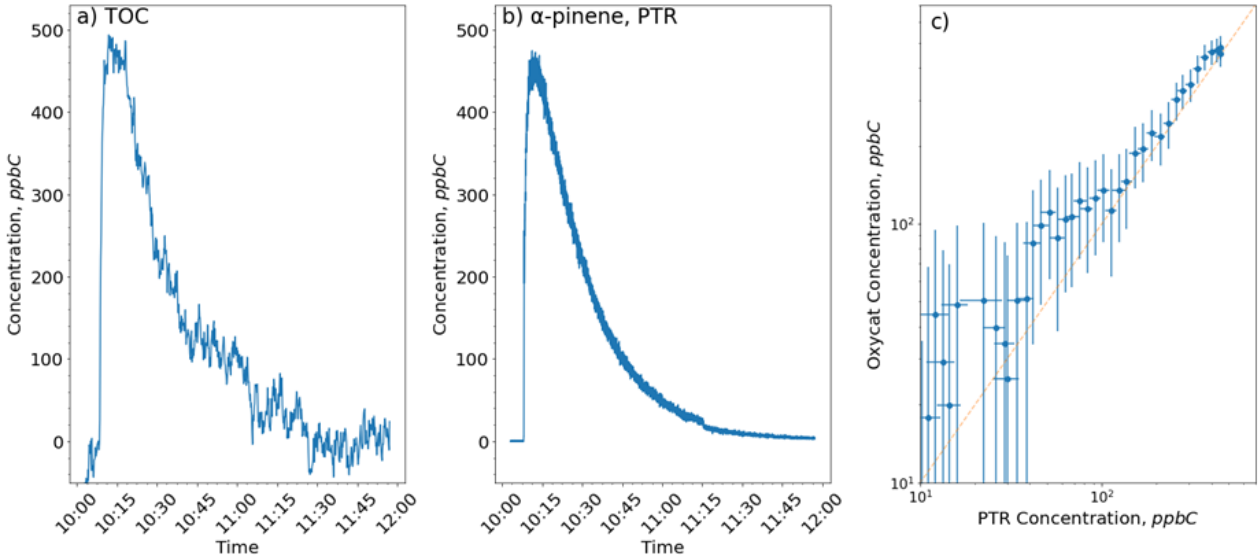

Figure 2.3: α-pinene calibration a) timeseries of Oxycat TOC, b) PTR reference timeseries, and c) calibration curve.

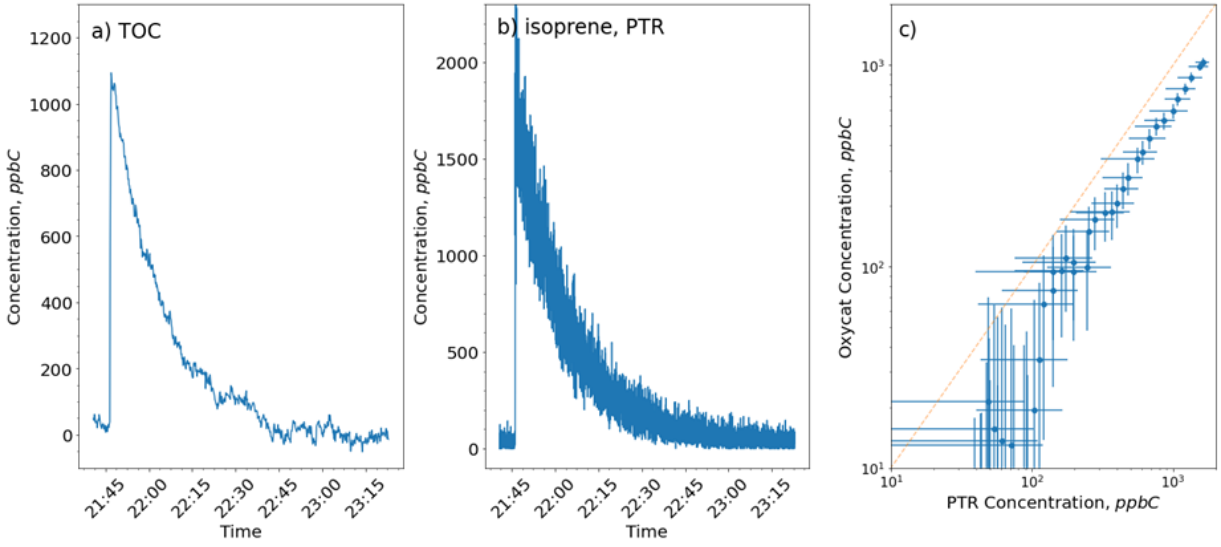

Figure 2.4: Isoprene calibration a) timeseries of Oxycat TOC, b) PTR reference timeseries, and c) calibration curve.

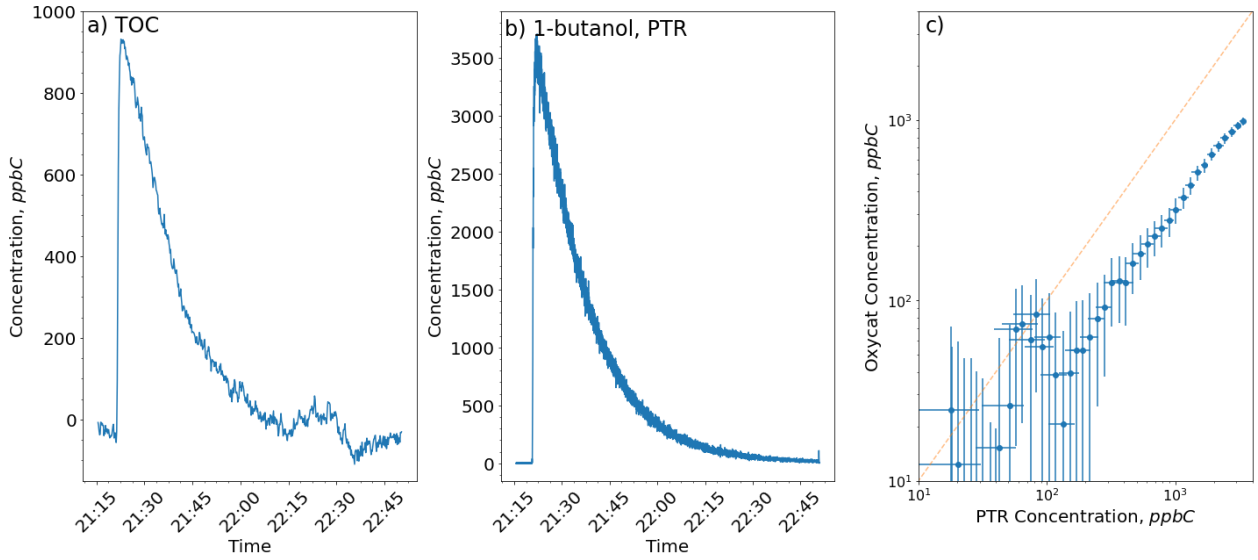

Figure 2.5: 1-butanol calibration a) timeseries of Oxycat TOC, b) PTR reference timeseries, and c) calibration curve.

Figure 2.6 shows the calibration time series and calibration curves for levoglucosan with the SMPS as a reference measurement. The levoglucosan concentration measured by the SMPS matched the concentration of TOC detected in the Oxycat, again suggesting complete conversion of the organic carbon to CO_2. However, there was a delay of several minutes in the increase of the signal followed by a delay in the decay of the signal relative to the SMPS measurement. This suggests that the particle mass was not quickly converted to CO_2. It is possible that the particle mass impacting the catalyst was pyrolyzed to black carbon rather than fully oxidized to CO_2, and that it took a longer period of time for this material to pass through the catalyst. This effect may be because of the large concentrations of particles that were present (in exceedance of 1000 $\mu g/m^3$), which correspond to highly polluted concentrations of particulate matter, and are 1 to 2 orders of magnitude higher than the SOA concentrations typical generated in laboratory experiments. To identify the extent of the time delay, we can correct the TOC time series in Figure 2.6a with a decaying transient function, as shown in Equations 2.1 and 2.2. It should be noted that the decrease in signal noise implied by this correction during the decreasing segment shows that it should not be used to imply greater precision in the instrument than in the original time series.

$$TOC_{increasing} = \frac{TOC}{1 - e^{-t/\tau_{inc}}} \quad (2.1)$$

$$TOC_{decreasing} = TOC * e^{-t/\tau_{dec}} \quad (2.2)$$

When correcting for a signal lag with a time constant of 700 seconds when particle concentrations are increasing and 1000 seconds when particle concentrations are decreasing, the time behavior of the increase and decrease with particle concentrations more closely matches the SMPS signal. The red scatter points in Figure 2.6b demonstrate a slight improvement in the calibration curve after correcting for, but the delay in the signal makes this calculation less

reliable than the gas-phase calibration curves. The time delay more generally suggests that quantification of particle phase TOC can only be calculated over long averaging periods.

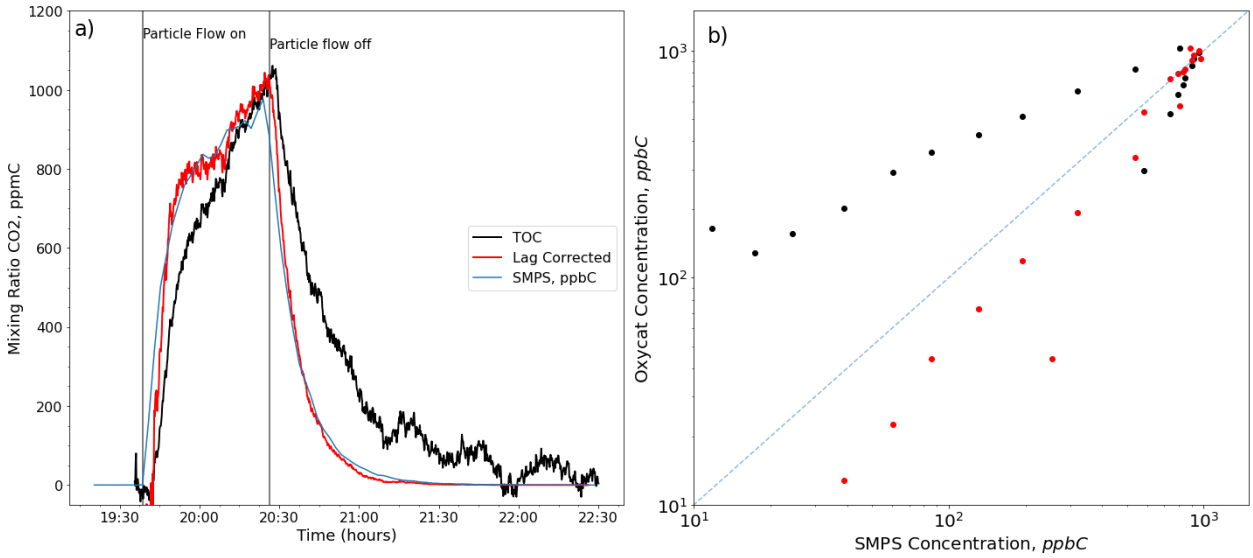

Figure 2.6: Levoglucosan calibration a) timeseries of concentration in chamber measured by both TOC and the SMPS, including a correction for lag with a 700 second time constant for increasing particle concentration and a 1000 second time constant for the decreasing particle concentration. b) calibration curve for the original TOC signal (black) and after correcting for time delay (red).

2.4.2 Evolution of TOC in laboratory experiments

Figure 2.7 shows the OxyCat timeseries during an oxidation experiment of alpha pinene. 750 ppbC of precursor was introduced to the environmental smog chamber. Following the onset of photochemistry, the carbon in the system was converted oxygenated organics and VOC. Assuming that all carbon content introduced at time one is preserved, the difference in TOC signal over time should be due to dilution resulting from replacement of instrument sampling flows. losses of semivolatile species to walls and inlet surfaces, and conversion to CO_2. Very little carbon should be mineralized at these oxidant concentrations and so is unlikely to represent much of the TOC signal loss in this experiment. The measured losses of carbon after correction for dilution can therefore be mainly attributed to conversion of VOC to semivolatile and low volatility species partitioning to the chamber walls. The time series in Figure 2.7 shows the evolution of TOC in the chamber after correction for dilution. In this experiment, we estimate a rate of approximately 10-40% loss to chamber walls, with 20% dilution of TOC levels within an hour of the initiated chemistry.

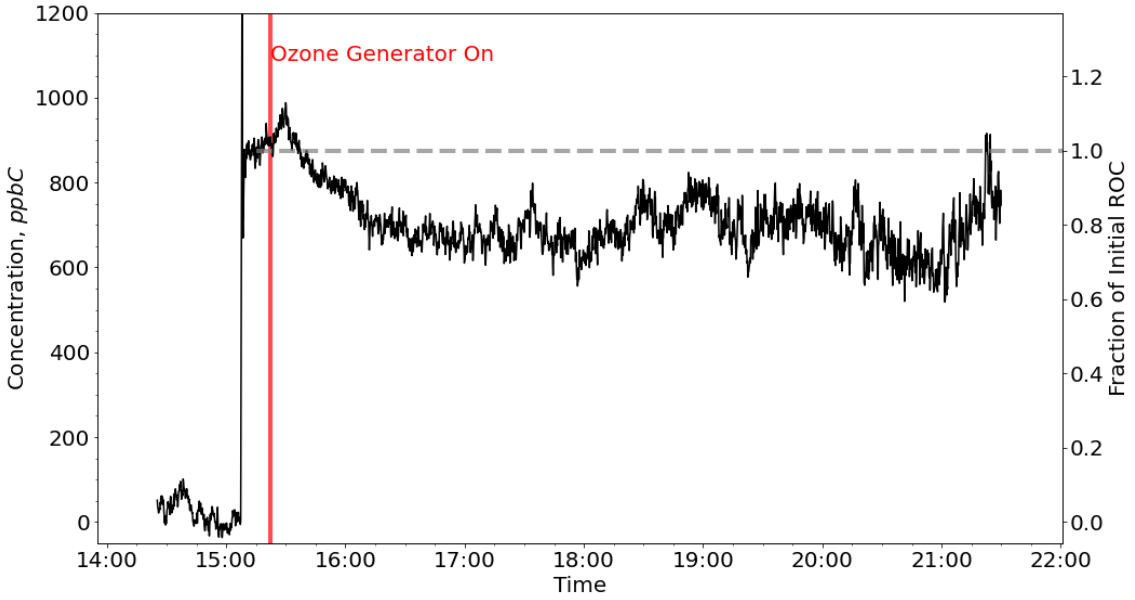

Figure 2.7: α-pinene ozonolysis experiment. After an initial concentration of precursor is added at the start of the total carbon content decreases faster than dilution, suggesting wall losses of up to 20% within an hour of formation, and 10-40% by the end of the experiment. Inefficient conversion of SOA to TOC should also be considered a possible factor for the decrease in TOC.

Figure 2.8 shows an additional application of the Oxycat to laboratory studies of air cleaner chemistry. In these experiments, limonene and toluene were introduced into the chamber, while different commercial air cleaners were in operation. Because the TOC measurement and the speciated VOC time series agree closely, and the reference CO_2 signal remains relatively constant, we conclude that the removal of carbon from the system was physical in nature rather than chemical. Oxidation of the VOCs by the air cleaners would have resulted in a more constant TOC measurement or increased the reference cell concentration of CO_2 over time if oxidation proceeded all the way to mineralization.

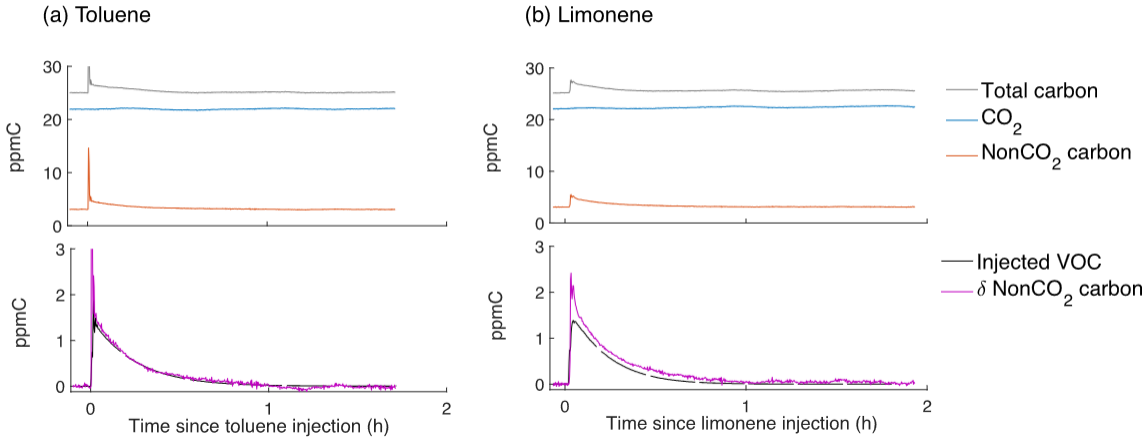

Figure 2.8: VOC removal by commercial air cleaner. Reproduced from Ye et al., 2021

Secondary CO_2 production can also be measured by changes in the concentration of the reference cell relative to the sample cell. At sufficiently high oxidation exposures, conversion of organic compounds to CO and then CO_2 is expected. This mineralization of ROC can be completed on the scale of weeks to months if depositional processes do not remove the carbon from the atmosphere first. This production is an important if relatively small source of atmospheric CO_2. Figure 2.9 demonstrates an experiment with high levels of oxidation which results in complete removal of ROC from the system over a few minutes. The black time series shows the increase in TOC following injection of isoprene to a smog chamber, represented by an increase in the CO_2 measurement downstream of the catalyst. Then, the conversion of the compounds to CO_2 results in an increase in reference CO_2 (blue), restoring the difference between the reference and catalyst channels (red), but at a higher baseline reflective of the increase in carbon content. This result suggests that for studies of longer-term oxidation (the equivalent to weeks or months in the atmosphere), the increase in CO_2 measured in the reference channel can estimate secondary CO_2.

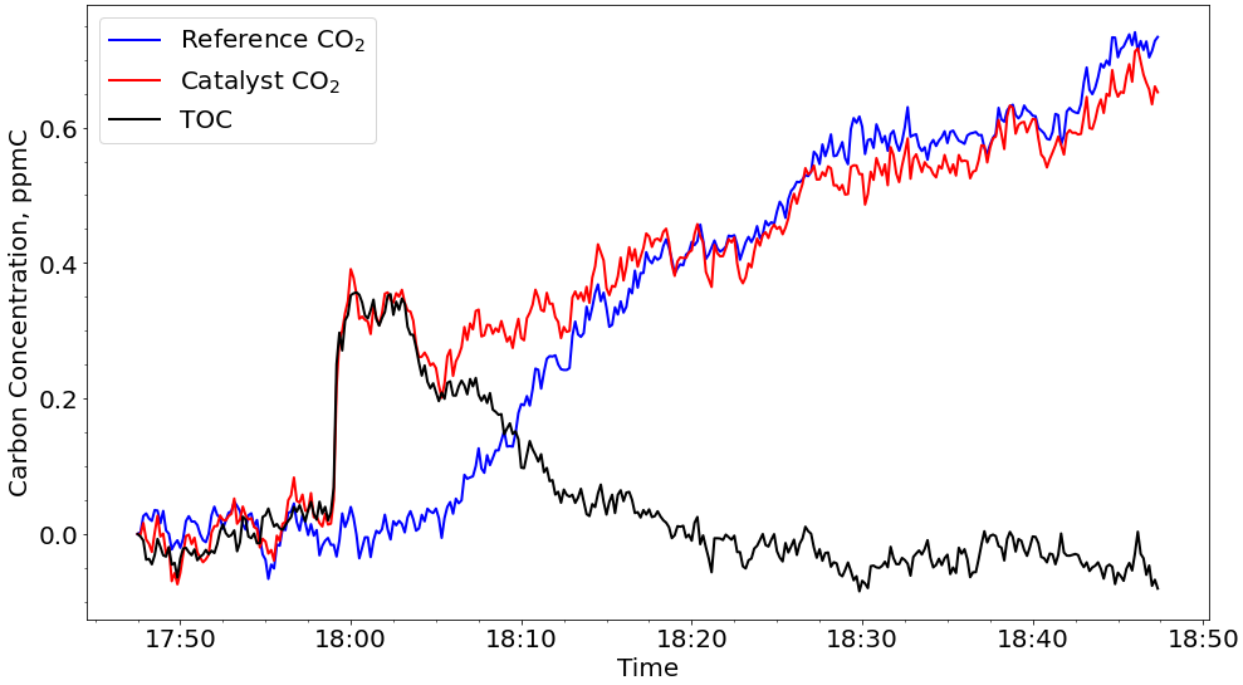

Figure 2.9: Secondary CO_2 production during a long-term isoprene aging experiment. After TOC is introduced, rapid chemistry converts carbon into CO_2, causing the baseline measurement to rise. Zero points of both reference and catalyst CO_2 signals were adjusted for visualization.

One effect that was discovered when applying this concept to chamber experiments was the drift in background CO_2 levels, which resulted in an increased CO_2 concentration in both measurements, but without a change in the differential measurement. This is most likely due to diffusion of CO_2 from the laboratory through the Teflon bag, which is diluted at higher flow rates of clean air to the Teflon chamber during periods of cleaning, but rises during the lower total flow rates used during batch mode experiments. While this effect nominally leaves the estimation of TOC intact, it complicates any estimation of secondary CO_2 as shown in Figure 2.9. After the TOC

is entirely converted to CO_2, CO_2 concentrations continue to rise in the chamber on an order of magnitude similar to the ROC concentration originally introduced. Mitigation of this effect is therefore desirable for any further studies of secondary CO_2 production. One manner in which this could be achieved is to lower CO_2 concentrations in the enclosure around the laboratory chamber – a reduction in the differential CO_2 gradient from over 400ppm in ambient conditions should decrease the magnitude of the change between the two steady states present at different pressures.

2.5 Conclusions

This measurement represents a real-time method for monitoring concentrations of total suspended carbon, which is a valuable tool for estimating the overall concentration of VOCs introduced into the laboratory chamber and for estimating wall losses. The high temperature catalyst can efficiently convert different classes of ROC to CO_2 and the differential gas analyzer is precise enough to track changes in ROC content on the order of 50 ppbC or greater. Typical chamber experiments involve 100-1000 ppbC of carbon, making this an applicable measurement technique for laboratory applications. The low levels of absolute CO_2 enable efficient measurements with time resolution high enough to constrain wall loss processes. Stabilizing the pressure within both cells allowed for a more consistent measurement and lowered high frequency noise in the CO_2 measurement. However, the persistence of a fluctuation on the order of 20-40 minutes across the CO_2 recordings as shown above limit further precision in tracking the evolution of ROC.

Tubing is required in order to deliver concentrations of VOCs and their oxidation products to the catalyst – unfortunately, even limited lengths of sampling line appear to have an appreciable impact on the loss of semivolatile species, especially particle-phase species, which will deposit even faster if charged. Ideally minimal tubing would connect the chamber to the catalyst in order to prevent underestimations of TOC. However, further minimizing tubing length to the OxyCat would require relocation of the high temperature catalyst furnace to inside the environmental chamber. Additionally, the observed lag in the TOC measurement for particle loadings introduces uncertainty to estimates of total carbon whenever high aerosol concentrations are involved. Adding a particle filter upstream of the catalyst could limit the TOC measurement to gas phase species, which could then be combined with a quantitative measurement of total organic aerosol by an Aerosol Mass Spectrometer to determine TOC without this effect.

An advantage of laboratory conditions in our study is the ability to remove background CO_2, methane, and CO from our measurement of TOC, which must be accounted for in ambient mesurements. This makes changes in the differential CO_2 due to TOC much easier to track. A measurement of total carbon is a valuable constraint on carbon content, especially if it can detect semi-volatile species and particle-phase organics with minimal losses in the sampling line. Quantifying every compound is infeasible in most contexts, even if all of the carbon can be measured, so there will be large uncertainties on the total carbon content of complex oxidized mixtures. Some work has suggested that deposition fates in chamber studies may more closely mimic the atmosphere, where deposition processes also serve as a chemical fate for much ROC

(Bi & Isaacman-VanWertz, 2025). Regardless, it is important to constrain the overall rates of wall loss by generally improving the availability of constraints on total organic carbon. This study demonstrates the applicability for tracking total organic carbon in real time in laboratory chambers. Better quantification of loss processes will serve to better constrain the chemical systems that are produced and monitored in a laboratory setting.

Chapter 3: Intercomparison of Secondary Organic Aerosol Composition Measurements from Multiple Online Mass Spectrometers

3.1 Chapter Abstract

Chemical ionization mass spectrometry combined with thermal desorption techniques has enabled the identification of a wide variety of organic aerosol species, greatly enhancing knowledge of aerosol composition. However, the selectivity of different chemical ionization schemes may influence the characterization of organic aerosol composition measured by a single mass spectrometer. Here we compare the measurement of laboratory-generated secondary organic aerosol by 3 chemical ionization mass spectrometers coupled to two desorption methods: "chemical analysis of aerosol online" inlet coupled with proton transfer reaction (CHARON-PTR-ToF-MS), and ammonium ionization (CHARON-NH_4-CIMS), and Filter Inlet for Gases and AEROsols coupled with iodide ionization (FIGAERO-I-CIMS). We see clear differences between the formulas detected in each instrument. The PTR tends to identify species with smaller carbon numbers and fewer oxygens, and the I-CIMS detects more oxygenated species, with carbon number formulas closer to the precursor, as well as the most nitrates and higher carbon number molecules. NH_4-CIMS detects a range of species intermediate to the other two instruments. The differences in formulas detected appear to be driven by fragmentation and selectivity of the ionization scheme, rather than desorption. However, some impacts of thermal vaporization cannot be ruled out. Despite differences in the formulas detected, agreements in the average oxidation state of the three CIMS suggest that there are not major biases in the chemical properties of the aerosol measured, which is also consistent with the Aerosol Mass Spectrometer. The differences between ionization scheme and rates of fragmentation are important to consider when interpreting a single spectrometric measurement as a representation of the entire composition of sampled aerosols.

3.2 Introduction

Organic compounds constitute a dominant fraction of aerosol particle mass globally, influencing the properties the Earth's atmosphere (Murphy et al., 2006). The presence of aerosols modifies the radiative balance of the atmosphere, both directly through scattering or absorption of light, and indirectly through participation as cloud condensation nuclei (IPCC, 2023). As a pollutant, the burden of atmospheric particulate matter on human health is estimated to be responsible for up to 8 (5.9-10) million premature deaths a year, the current largest environmental risk factor for excess mortality (Burnett et al., 2022). A majority of organic aerosol is formed from the oxidation of volatile organic compounds (VOCs), which can either nucleate new particles or condense onto existing aerosol mass (Zhang et al., 2007; De Gouw & Jimenez, 2009). These lower-volatility compounds are produced from the oxidation of potentially tens of thousands of different species, varying considerably in chemical formula, structure, functionalization, reactivity and properties (Goldstein & Galbally, 2007; Ziemann & Atkinson, 2012; Calvo et al., 2013). Links between formation conditions/key compounds and emergent aerosol properties relevant to both climate and health responses continue to be explored in studies of aerosol composition (Vogel et al., 2016; Shrivastava et al., 2017; Pye et al., 2021; Liu et

al., 2023; Dobracki et al., 2025). Accurately determining the relationship between the formation and properties of SOA, as well as developing and implementing accurate mechanistic models of SOA requires comprehensive characterization of its chemical composition, in both field measurements and laboratory studies.

Mass spectrometry is an essential tool for studying the properties and impacts of both VOCs and SOA. Since achieving sufficient mass resolving power to separate molecules at the same nominal mass and limits of detection relevant for atmospheric concentrations, time-of-flight mass spectrometers (ToF-MS) have enabled real time simultaneous compositional measurements of ambient trace gases (Blake et al., 2004; Junninen et al., 2010) and aerosols (Jimenez et al., 2003). Most commonly, the aerosol mass spectrometer (AMS) has been used to great effect in advancing knowledge of aerosol composition (DeCarlo et al., 2006). The electron ionization beam and the high temperature of evaporation applied in the AMS are known to induce high levels of ion- and thermal-fragmentation. Extensive characterization of this fragmentation and comparison to calibration standards have permitted the AMS to be used as a bulk measurement which measures a large range of organic and inorganic molecules in real time, relating these elemental ratios to portions of the absolute mass loadings sampled. Compositional information about organic aerosol generated from AMS data is based upon the analysis of smaller fragments in aggregate, each with differing levels of carbon, hydrogen, oxygen, and nitrogen atoms (Canagaratna et al., 2007; Aiken et al., 2008; Canagaratna et al., 2015). Therefore, while AMS data can characterize aerosol composition and provide information about sources through positive matrix factorization and tracer analysis, specific formulas for organic molecules cannot be deduced directly from AMS measurements alone (Zhang et al., 2007).

Chemical ionization mass spectrometry (CIMS), a technique which charges analyte molecules by reaction with ionized reagents, is an effective and easily adaptable method for measuring atmospheric compounds. Low interaction energies of the ion-molecule chemistry decrease fragmentation rates and permit the direct detection of molecular species, which has been applied extensively to gas-phase organic compounds (Bertram et al., 2011). A wide variety of ionization schemes have been implemented in different mass spectrometers, including but not limited to: proton transfer reaction (Sunner et al., 1988; Breitenlechner et al., 2017), ammonium (Lindinger et al., 1998), iodide (Huey et al., 1995), nitrate (Jokinen et al., 2012), nitric acid and oxygen (Blake et al., 2006; Jordan et al., 2009), benzene (Ketkar et al., 1991), acetate (Veres et al., 2008) and bromide (Sanchez et al., 2016; Rissanen et al., 2019). Analyte molecules are then mainly detected as ions with the combined mass of the measured species plus the reagent ion used, or as a protonated version of the measured species. The introduction of these varied ionization schemes has resulted in an enhanced ability to detect multifunctional organic compounds.

Thermal desorption enables CIMS techniques to be applied to aerosol species with lower levels of ion-induced fragmentation. Two main approaches have been applied – the first involves a filter collection phase followed by a desorption phase where a heated carrier gas evaporates the particle material into an ionizable gas. This technique, the Filter Inlet for Gases and AEROsols (FIGAERO) (Lopez-Hilfiker et al., 2014) has been deployed in a number of field campaigns (Lee et al., 2016; Mohr et al., 2017; W. Huang et al., 2019) and laboratory studies (D'Ambro et al., 2017;

Takeuchi & Ng, 2019; Q. Ye et al., 2019; Zaytsev, Koss, et al., 2019). It provides a window for gas-phase CIMS operation during filter collection and then sorts the aerosol species by volatility by slowly ramping the desorption gas temperature and sampling the evaporated components. A second strategy removes gaseous vapors through use of a charcoal denuder and then volatilizes the particle material through a high temperature inlet region (Hellén et al., 2008; Holzinger et al., 2010; Salvador et al., 2016). This technique was applied in the "chemical analysis of aerosol online" (CHARON) inlet (Eichler et al., 2015), which has been used in a number of laboratory studies of SOA formation, as well as in ambient and aircraft monitoring campaigns (Müller et al., 2017; Piel et al., 2019; Tan et al., 2021; Reinecke et al., 2024; Song, Gkatzelis, et al., 2024). In contrast to the FIGAERO inlet, the CHARON inlet provides higher time resolution and avoids the possible biases of filter collection. However, the desorbing temperature must be optimized between more thorough desorption of lower volatility compounds and decomposition of more thermolabile ones.

Every chemical ionization setup will be more or less efficient in detecting certain analytes depending on the favorability of adduct formation or proton transfer with that reagent. This chemical specificity therefore potentially leads different CIMS to detect different classes of compounds with varying sensitivity. In order to understand the impact and coverage of the chemically selective CIMS measurements, direct comparisons of co-located measurements are valuable in demonstrating the overlaps and gaps between multiple instruments. Previous studies have examined the areas in chemical space measured by different CIMS techniques in the gas and particle phase in terms of the volatility, carbon number, elemental ratios, and oxidation state of the measured compounds (Aljawhary et al., 2013; Isaacman-VanWertz et al., 2017; Riva et al., 2019). Others have assessed the performance of a single aerosol-CIMS by use of aerosol calibration standards (Leglise et al., 2019), in comparison to the AMS (Cai et al., 2024; Chen et al., 2024), with different desorption techniques (Gkatzelis et al., 2018), with gas chromatographic techniques coupled to CIMS (Timkovsky et al., 2015; Thompson et al., 2017; Y. Huang et al., 2020), and in comparison to electrospray ionization (Xin et al., 2024). However, to our knowledge, there has not been a comparison of the chemical distribution of different online particle-CIMS measurements, or a direct comparison of the FIGAERO and CHARON inlets.

In order to assess differences in the selectivity and comprehensiveness of different CIMS techniques, we present multiple simultaneous online SOA measurements from a series of laboratory chamber studies. In these experiments, secondary organic aerosol was generated by oxidation of a single VOC precursor. Four instruments for measuring particle-phase composition are compared: a "chemical analysis of aerosol online" (CHARON) inlet Proton Transfer Reaction-Mass Spectrometer (CHARON-PTR-MS), a CHARON-Ammonium-CIMS (CHARON-NH_4-CIMS), an Iodide-CIMS with a Filter Inlet for Gases and Aerosols (FIGAERO-I-CIMS), and an aerosol mass spectrometer (AMS). Using the formulas obtained from the spectra in each instrument, we evaluate chemical properties such as the oxidation state and elemental composition of the detected products as a distribution. The differences in the distribution of organic aerosol species observed arise from changes in selectivity, potentially resulting from both the differences in ionization and desorption technique. We lastly consider the comprehensiveness of each of these CIMS measurements in the context of AMS measurements, using oxidation state as a measure of

the extent of chemical aging of the aerosol. An understanding of these differential sensitivities is essential for designing and interpreting studies of aerosol composition.

3.3 Methods

Particle-phase data was collected during a series of SOA formation experiments using the MIT environmental chamber (Koss et al., 2020). The 7.5 m^3 Teflon chamber was continually provided with VOC-free air from an AADCO generator at a rate of 15 L/min. Experiments were performed at 20°C and 2-2.3% relative humidity. In each experiment, ammonium sulfate particles were introduced to serve as seed aerosol, followed by the dilution tracer hexafluorobenzene. The VOC precursor for a given experiment was then introduced by syringe injection, and nitrous oxide (HONO) was added as an OH precursor. Once initial concentrations were measured, oxidation was initiated by the photolysis of HONO to produce OH by 40 W UVB lights with a spectral peak at 350 nm surrounding the chamber. Experiments lasted an average of 7 hours, with additional introduction of HONO aliquots during the experiments to facilitate further oxidation. Results below focus on two experiments, the oxidation of α-pinene and 1,2,4-Trimethylbenzene (TMB), which represent a common biogenic and anthropogenic precursor, respectively.

Particle composition was monitored using three CIMS-based techniques. The first instrument combined the "chemical analysis of aerosol online" (CHARON) inlet with a PTR3 mass spectrometer operating in H_3O^+ and NH_4^+ ionization mode. The CHARON inlet was set to continuously sample in particle-phase mode, which removes gas-phase species by adsorption to a charcoal denuder, followed by high temperature desorption of the transmitted aerosol at 180°C (Eichler et al., 2015). In H_3O^+ mode (referred to hereafter as PTR), $(H_2O)H_3O^+$ clusters serve as the reagent ion, reacting with species whose proton affinity is higher than water to produce protonated ions; this is particularly effective at measuring a wide range of hydrocarbons and some oxidized VOCs (Lindinger & Hansel, 1997). The PTR3 instrument used is sensitive to sub parts-per-billion concentrations of hydrocarbons and monofunctional aldehydes, alcohols, ketones, and organic nitriles (Breitenlechner et al., 2017). In NH_4^+ mode (afterwards NH_4-CIMS) (with $(H_2O)NH_4^+$ clusters serving as the primary ion) detected aerosol compounds as ammonium ion adducts. This ionization scheme is able to detect oxygenated organic molecules with multiple functional groups. Relative to H_3O^+, this results in detection of relatively larger, more oxygenated species (Zaytsev, Breitenlechner, et al., 2019). Switching between the two ionization settings was automated to alternate approximately every 3'45", effectively collecting two independent datasets of particle composition data over the course of the experiments.

An Iodide-ToF-MS was deployed with a FIGAERO inlet (Lopez-Hilfiker et al., 2014, 2016). As described above, the FIGAERO switches between gas-phase sampling with filter collection and aerosol-phase thermograms at approximately 30-minute intervals. During particle sampling to the I-CIMS, the desorption gas slowly ramped up over 15 minutes from 30-160°C. Due to a lack of volatility information in the other CIMS, the distribution of product volatility was not included in this analysis. Iodide CIMS is sensitive to multifunctional organic compounds, highly oxidized molecules, and organic nitrates, owing to the additional vibrational modes provided by the functional groups to stabilize the ion-analyte cluster. Conversely, this ionization scheme is

insensitive to non-oxygenated hydrocarbons, and only weakly sensitive to monofunctional ketones, aldehydes and alcohols (Lee et al., 2014b, 2016; Lopez-Hilfiker et al., 2016). Analyte peaks were fitted for organic masses with a single iodide adduct whose time-series behavior produced a thermogram pattern during the ramp cycles. Intensity of the signal was determined by integrating the thermogram area during the ramp cycle. Possibly due to a cold zone in the sampling setup, a correction was applied to many thermograms to remove an artifact attributable to a gas-phase signal (Appendix Section 3.A.1, Figure 3.A.1).

Total organic aerosol mass and sulfate seed concentrations were monitored using the Aerosol Mass Spectrometer (DeCarlo et al., 2006). AMS calibration was performed using ammonium nitrate as a standard (Koss et al., 2020). Elemental ratios and average oxidation state were calculated using both the Aiken and Improved Ambient corrections (Aiken et al., 2008; Canagaratna et al., 2015). The Aiken calculation corrects for biases in the O:C and H:C ratios measured from known particle-phase standards, and the Improved Ambient calculation additionally corrects for two fragments, H_2O^+ and CO^+, with high ambient signal interference. Maximum organic aerosol mass loadings were 1.6 μg/m^3 in the trimethylbenzene experiment and 14.6 μg/m^3 for the α-pinene experiment. The AMS measurement in each experiment is assumed to measure the elemental composition from the entire SOA mass sampled without selectivity for certain classes of compounds.

3.4 Results and Discussion

3.4.1 CIMS Product Spectra

Hundreds of products were detected in both experiments by each of the 3 CIMS techniques. To account for differences in sampling, a single FIGAERO-I-CIMS thermogram spectrum was compared to the average of the CHARON-PTR-MS and CHARON-NH_4-CIMS time-series during that same FIGAERO collection cycle. This window corresponds to the maximum organic signal detected in the AMS, approximately 3.5-4.5 hours into each experiment, with 96% and 87% decay of α-pinene and trimethylbenzene, respectively (Figures 3.A.2 & 3.A.3). Carbon number weighted enhancements of each product signal were compared after subtracting background concentrations. The normalized carbon distributions show the fractional contributions of each product to the total product signal in each instrument. Differences between these distributions for different classes of compounds correspond to differences in instrument selectivity.

The α-pinene SOA spectra detected by the 3 CIMS techniques are overlaid and individually visualized as Generalized Kendrick Analysis (GKA) plots in Figure 3.1. GKA is a modification of a mass defect plot that can separate of odd and even masses into positive and negative GKA values, cleanly separating organic mononitrates and non-nitrogen containing species (Appendix Section 3.A.2, Alton et al., 2023). Formulas with multiple nitrogen atoms were a negligible fraction of detected ions. The distributions generally cluster in four regions of GKA vs mass space. The largest cluster corresponds to functionalized and fragmented products of the precursor ($C_{10}H_{16}$) with no nitrogen atoms ($C_{2\text{-}10}H_yO_z$, upper left). In addition to this region, there are organic nitrates ($C_{2\text{-}10}H_yNO_z$, lower left) and higher carbon number compounds with and without nitrogen, respectively ($C_{11\text{-}22}H_yN_{0\text{-}1}O_z$, upper and lower right). The three CIMS detect many species in

common (Figure 3.1a) but there are clear differences reflected in the mass ranges of each instrument. In the α-pinene experiment, 80% of the carbon-weighted signal (10^{th}-to 90^{th} percentiles) in the monomer region is between m/z values of 58-196 for the PTR – this distribution shifts to 122-216 for the NH_4-CIMS, and m/z 166-265 for the I-CIMS. For 1,2,4-TMB, these ranges are m/z 48-160, 88-212, and 146-277, for the PTR, NH_4-CIMS, and I-CIMS, respectively (Figure 3.A.4). Two effects may be contributing to the differences in the mass ranges in each ionization scheme. The first is differences in ionization sensitivity, where more oxygenated products (which have higher masses) are less likely to be ionized in the PTR. The larger mass/more functionalized products are more sensitive to detection by NH_4-CIMS, and I-CIMS is sensitive only to the most oxygenated compounds. Conversely, I-CIMS appears insensitive to smaller, less oxygenated products. The second possible effect is that the larger, more functionalized species sampled and in the PTR fragment during ionization and then detected as smaller masses. The difference between the lower mass range in the PTR and NH_4-CIMS spectra which share the CHARON inlet suggests ionization rather than thermal desorption drives the changes observed in lower mass products. The absence of smaller masses in the I-CIMS spectrum suggests minimal fragmentation effects from the FIGAERO but could also be due to low sensitivity to smaller compounds.

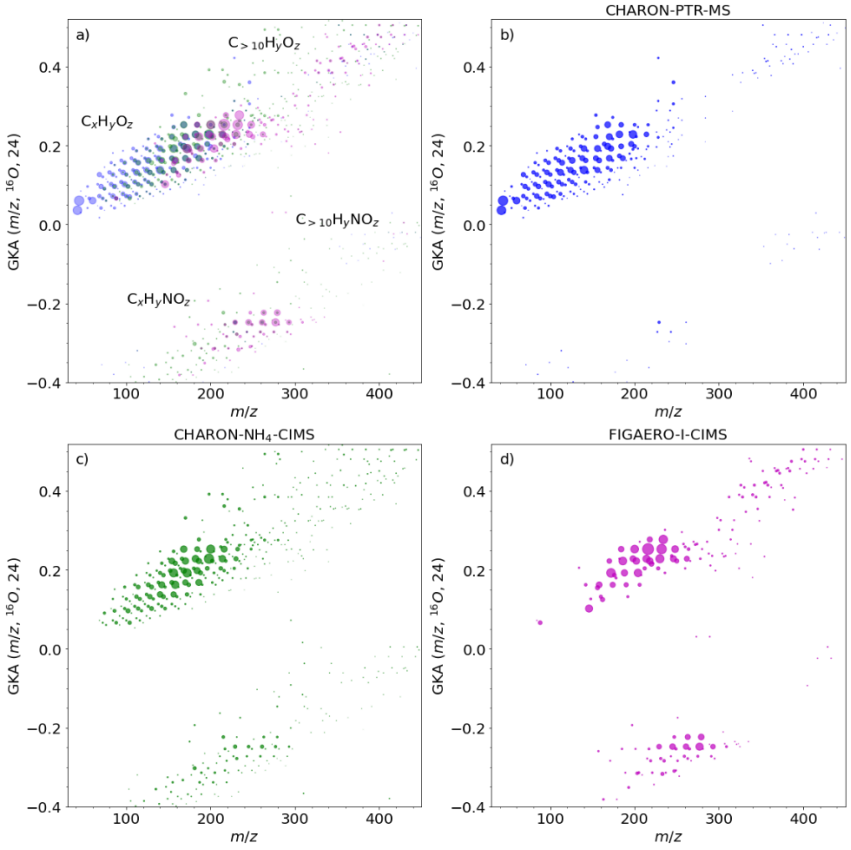

Figure 3.1: Generalized Kendrick Analysis plot of α-pinene SOA (without H^+, NH_4^+, or I^- adduct) for a) three CIMS techniques overlaid, b) PTR-MS, c) NH_4-CIMS, and d) I-CIMS. Positive GKA values correspond to even number masses ($C_xH_yO_z$) and negative with odd masses ($C_xH_yNO_z$). Circle size corresponds to the carbon weighted fraction of total ion signal.

3.4.2 Elemental Distributions

Figure 3.2 shows carbon, hydrogen, and oxygen number histograms detected by the three CIMS techniques for the α-pinene oxidation experiment. As in Figure 3.1, signals are weighted by carbon number and normalized to total instrument signal. SOA compounds detected in the PTR occupy a range from $C_{2\text{-}10}$, with an average carbon number of 7.1 (Figure 3.2a top). The PTR carbon number distribution suggests high levels of fragmentation, because the C_2 compounds present will not have low enough volatilities to partition into the particle-phase but comprise 10% of the carbon-weighted instrument signal. C_{10} compounds, which have not lost carbon atoms to fragmentation during oxidation or detection, make up only 14% of the PTR signal. The NH_4-CIMS distribution has a higher average carbon number of 8.7, with a greater proportion of $C_{7\text{-}10}$ compounds, reflecting a much lower rate of fragmentation than the PTR distribution. In the I-CIMS, C_{10} compounds comprise more than 50% of instrument signal, implying minimal instrument fragmentation, with $C_{7\text{-}9}$ compounds contributing a smaller but significant fraction, each more than 5% of the overall signal. Particle-phase compounds with 7-10 carbon atoms are consistent with prior mechanistic and chamber studies of SOA composition from α-pinene (Eddingsaas et al., 2012; Mutzel et al., 2016).

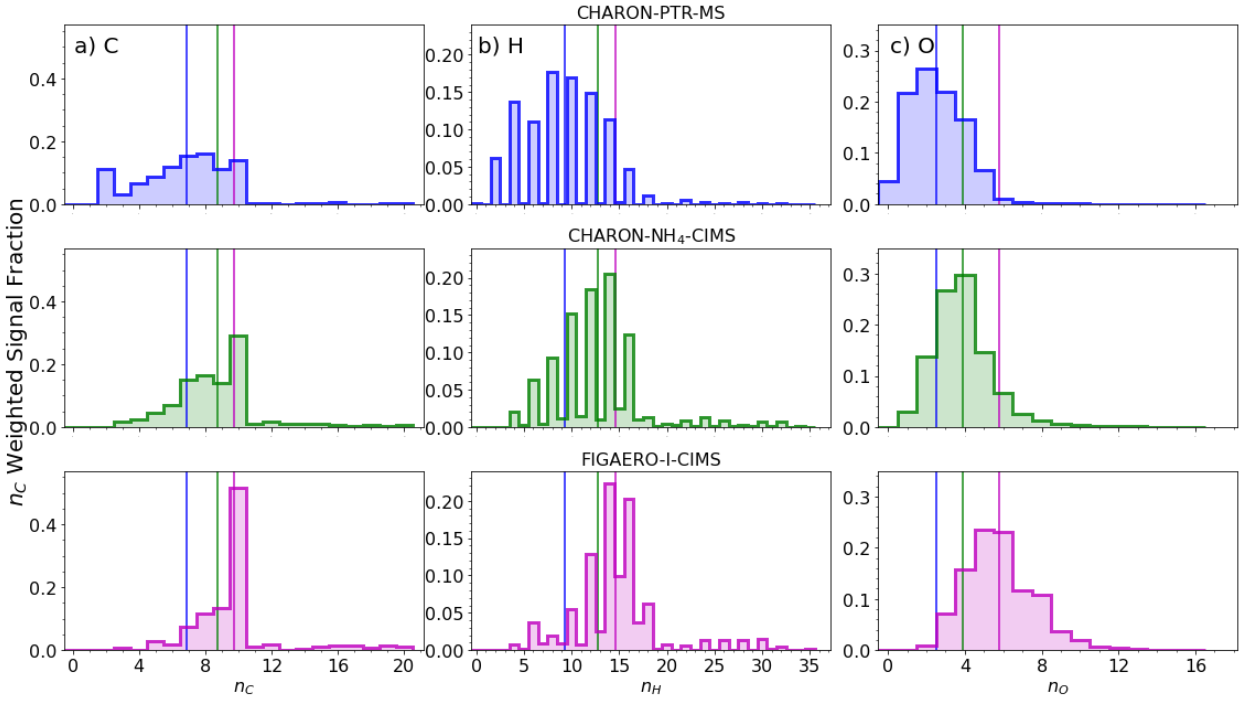

Figure 3.2: Product distributions of a) carbon, b) hydrogen, and c) oxygen number collected by CHARON-PTR-MS (top row), CHARON-NH_4-CIMS (middle), and FIGAERO-I-CIMS (bottom) in the α-pinene oxidation experiment. Color coded distribution averages for each instrument are represented as vertical lines. Fraction of total signal is weighted by the carbon number of each formula.

The hydrogen number distributions for each instrument are presented in Figure 3.2b. The products detected are closed shell compounds, which require an even number of hydrogens for hydrocarbons without nitrogen. Therefore, only the organic nitrates contribute odd hydrogen

numbers to the distribution. The main differences in hydrogen number distributions broadly correspond to the differences in carbon number distribution. The loss of carbon skeleton atoms implies corresponding losses of hydrogens bonded to each carbon atom. In the PTR, the average hydrogen number is 9.2, with some compounds containing as few as 2 hydrogens. The NH_4-CIMS detects some low hydrogen number compounds but has a higher average hydrogen number of 12.6. The products detected in the I-CIMS mostly have 12-18 hydrogens (an average of n_H=14.7), with some H_{15} or H_{17} organic nitrates contributing a significant portion of the instrument signal. There are some products with more than 20 hydrogens detected mainly in the NH_4-CIMS and I-CIMS, which correspond to the higher carbon number compounds discussed in the GKA plot. The differences in average hydrogens again reflect the increased influence of fragments in the products detected by the PTR and to a lesser extent the NH_4 and I-CIMS.

Figure 3.2c shows the oxygen number distributions detected by the three CIMS. Like the carbon number distribution, there are clear differences between the different measurements. The PTR-MS mostly detects compounds with fewer than 6 oxygens. Highly oxygenated molecules, typically defined as products with more than 6 oxygens (Bianchi et al., 2019) contribute only 1% to the overall instrument signal. PTR-MS studies with a CHARON inlet similarly report this range of oxygen number products (Song, Saathoff, et al., 2024). The NH_4-CIMS mainly detects compounds with 2-6 oxygens, with 12% of the instrument weighted signal corresponding to HOMs. The I-CIMS distribution detects compounds with 3-10 oxygens, measuring the largest fraction of HOMs (54% of signal) of the 3 CIMS. The averages again are distinct, with an average of 2.5 oxygens in the PTR, 3.9 in the NH_4-CIMS and 5.8 oxygens in I-CIMS. The relative difference in the carbon number and oxygen number distributions suggests that NH_4-CIMS and PTR detects a smaller range of the multifunctional C_{10} compounds measured by the I-CIMS, owing to a combination of thermal- and ion-fragmentation and selectivity effects.

Similar elemental distributions are observed in the 1,2,4-TMB experiment (Figure 3.A.5). The peak of the carbon number distribution in the I-CIMS is centered around n_C=9 rather than 10, reflecting the carbon number of 1,2,4-TMB (C_9H_{12}). Due to the lower initial hydrogen number of the precursor formula, the hydrogen number histogram is slightly shifted to lower n_H. The oxygen number distributions showed that less oxygenated products were detected in the PTR, with more oxygenates detected in the NH_4-CIMS, and HOMs comprising a dominant fraction of instrument signal in the I-CIMS.

3.4.3 Organic Nitrates

Nitrogen-containing species are detected in each CIMS. Figure 3.3 shows the GKA region from Figure 3.1 corresponding to organic nitrates from α-pinene SOA. There are large differences in the relative amounts of organic nitrates detected. Only a few species are detected by the PTR, comprising only 2% of the overall carbon weighted signal in the α-pinene experiment, mostly present in the compound $C_{10}H_{15}NO_5$ (m/z = 229.095, GKA=-0.248, Figure 3.3b). In contrast, both the NH_4-CIMS and I-CIMS detect several nitrogen-containing products, covering a wide range of formulas. Nearly 20% of the instrument signal in the I-CIMS is attributed to nitrogen containing species. The most prominent formulas in each signal are detected in both NH_4-CIMS and I-CIMS, consisting of $C_{10}H_{15}NO_{5\text{-}9}$ (GKA = -0.248) and $C_{10}H_{17}NO_{7\text{-}8}$ (GKA = -0.224), but there are key differences between the two in the relative abundance of the different products. The NH_4-CIMS

$C_{10}H_{15}$ organic nitrates are roughly equal in signal, with the most prominent being $C_{10}H_{15}NO_5$. By contrast, $C_{10}H_{15}NO_8$, followed by $C_{10}H_{17}NO_8$, is most prominent in the I-CIMS. The 1,2,4-TMB GKA distributions in Figure 3.A.4 corroborate the near absence of organic-nitrates with the PTR, detection of more nitrates with the NH_4-CIMS, and major nitrate signal in the I-CIMS.

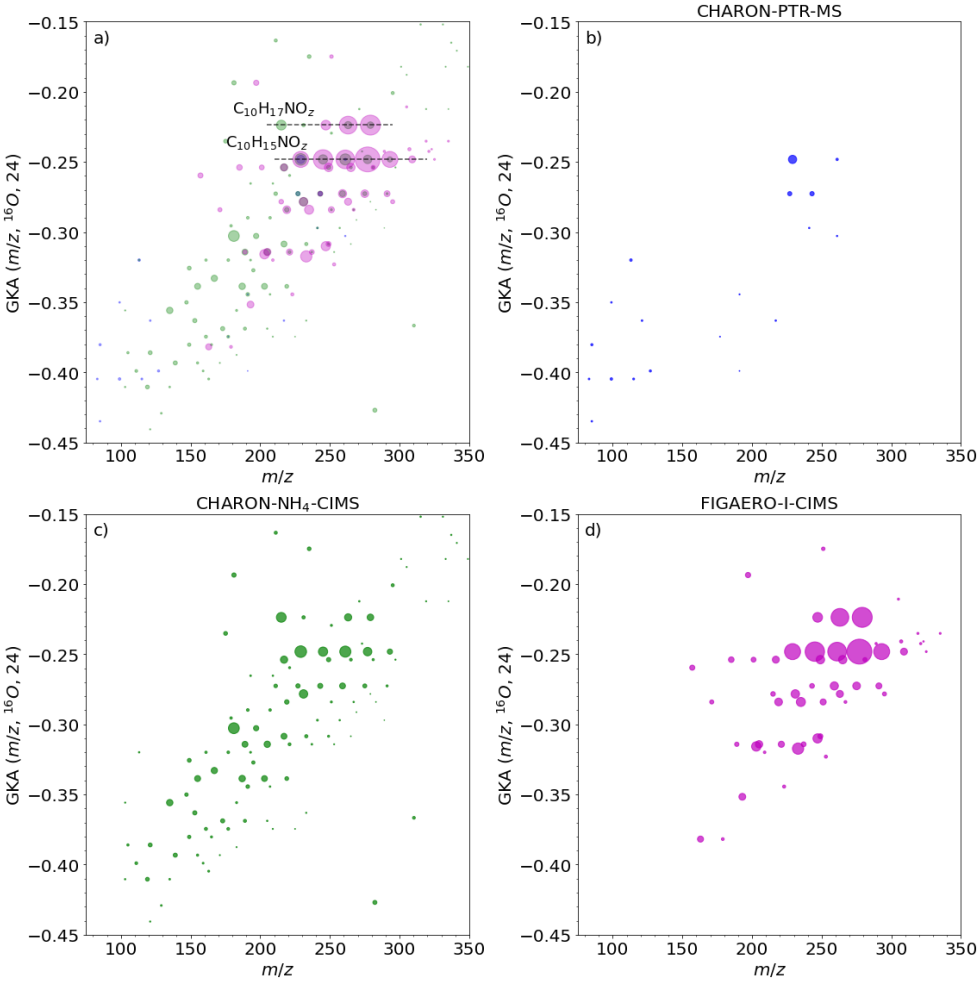

Figure 3.3: $C_{2\text{-}10}H_yNO_z$ region of α-pinene SOA GKA plot, showing relative abundance of nitrogen-containing species of a) 3 CIMS techniques overlaid, b) PTR-MS, c) NH_4-CIMS, and d) I-CIMS.

The discrepancies between instruments in detection of nitrogen containing species and the relative signal intensities of specific nitrates have two potential drivers: the first is that the CHARON inlet may be thermalizing more nitrate functional groups than the FIGAERO, and the second is that ionization selectivity influences the detection of organic nitrates. The NH_4-CIMS and PTR use the same inlet scheme, so the lack of organic nitrates detected in the NH_4-CIMS but not in the PTR must be primarily related to differences in ionization. In prior toluene and 1,2,4,-TMB oxidation experiments using the NH_4-CIMS, organic nitrates with similar oxygen numbers to this study were detected (Zaytsev, Koss, et al., 2019). Prior studies using a CHARON-PTR-MS for particle-phase analysis have reported on some ambient nitrogen containing aerosol species, but the products detected contained fewer than 6 oxygens (Müller et al., 2017; Peng et al., 2023).

Ionization effects therefore seem to dominate the differences in detection of the more oxygenated organic nitrates produced in the α-pinene experiment and measured by the I-CIMS.

3.4.4 Dimers

A second prominent category of compounds which are detected by all CIMS instruments are higher carbon number compounds, formed from cross reactions of organic species. Figure 3.4 shows the GKA region from Figure 3.1 corresponding to $C_{11\text{-}22}H_yO_z$ species. For all instruments, the total signal in this region is a small fraction relative to the monomeric compounds. The PTR detects the fewest species in this region. The NH_4-CIMS detects a larger range of ions, and I-CIMS most clearly detects specific dimer species (shown by the larger circle sizes). $C_{>10}$ compounds contribute 2%, 9, and 10% of carbon weighted instrument signal to the PTR, NH_4-CIMS, and I-CIMS, respectively. If limited to $C_{>15}$ compounds, this fraction becomes 1%, 4%, and 7% of the overall signal, highlighting the greater detection of higher carbon number products by the I-CIMS, consistent with the visualization in Figure 3.4. Analogous to the differences between detection of organic nitrates, the common inlet in the PTR and NH_4-CIMS suggests differences in ionization mode are responsible for the limited detection of higher carbon number species in the PTR.

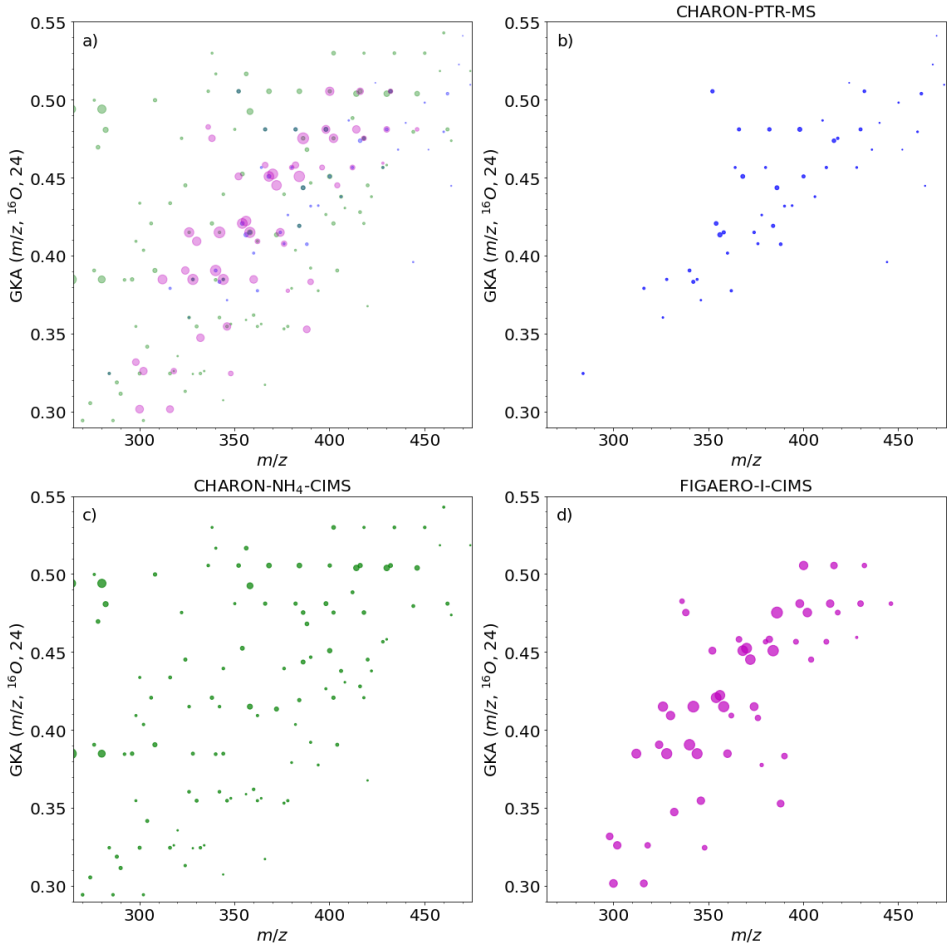

Figure 3.4: GKA plot of α-pinene SOA from m/z 300-500, showing relative abundance of dimers ($C_{11\text{-}22}H_yO_z$) for a) 3 CIMS techniques overlaid, b) PTR-MS, c) NH_4-CIMS, and d) I-CIMS.

3.4.5 Oxidation State

To compare the ensemble of measurements between different instruments, bulk properties of the distribution are a valuable metric for similarity. This can be especially useful for comparison to fragmented measurements such as the AMS, which nevertheless determines information about the chemical properties of the aerosol without direct detection of the parent components. One metric the extent of chemical processing of organic species is the average oxidation state, $\overline{OS_C}$, of the carbon atoms in a given molecule, which can be calculated from the elemental ratios of the compound formula:

$$\overline{OS_C} = 2\frac{O}{C} - \frac{H}{C} - 5\frac{N}{C} \qquad (3.1)$$

The higher the average oxidation state of the aerosol, the more oxidation the carbon has undergone during formation and aging. Equation 3.1 assumes that each oxygen functional group has an oxidation state of -2, each hydrogen has an oxygen state of +1, and each nitrogen an oxidation state of +5. These assumptions do not peroxide functional groups, but the errors introduced by the presence of peroxides is small for larger carbon molecules (Kroll et al., 2011).

Figure 3.5 shows the oxidation state histograms for the three CIMS instruments and their average oxidation states for the α-pinene SOA (a) and 1,2,4-TMB SOA (b). Average oxidation state measured by the AMS as calculated from the Aiken and Improved Ambient calculations, indicated by the brown and red vertical lines, respectively. Differences in the relative abundance of species at specific oxidation states is clear from the differences in the top, middle, and bottom histograms. However, the average oxidation state of the three CIMS measurements for the α-pinene experiment broadly agree with each other and with the AMS estimations. The agreement in average oxidation states suggests differences among the various techniques (which differ in terms of fragmentation, detection of organic nitrates and HOMs, and larger MW species) do not have a large impact on the calculation of average oxidation state, likely due to the smaller signal of the higher-carbon number species and the similarity between average oxidation states of molecules containing and lacking nitrate functionalization. This implies that the selectivity of each technique does not reflect biases in sampling more or less oxidized or reduced organic species. The distribution of average oxidation states is somewhat more separated in the 1,2,4-trimethylbenzene experiment, but still there is overall agreement between the 3 instrument histograms, as well as with the improved ambient $\overline{OS_C}$ value from the AMS. There are more differences between the 3 CIMS techniques in individual elemental ratios (Figures 3.A.6,3.A.7) reflecting the different degrees of oxygenation and fragmentation, as well as double bond equivalency per carbon (Figures 3.A.8,3.A.9, primarily an effect of fragmentation differences) but the CIMS and AMS all measure SOA with roughly the same the degree of oxidation.

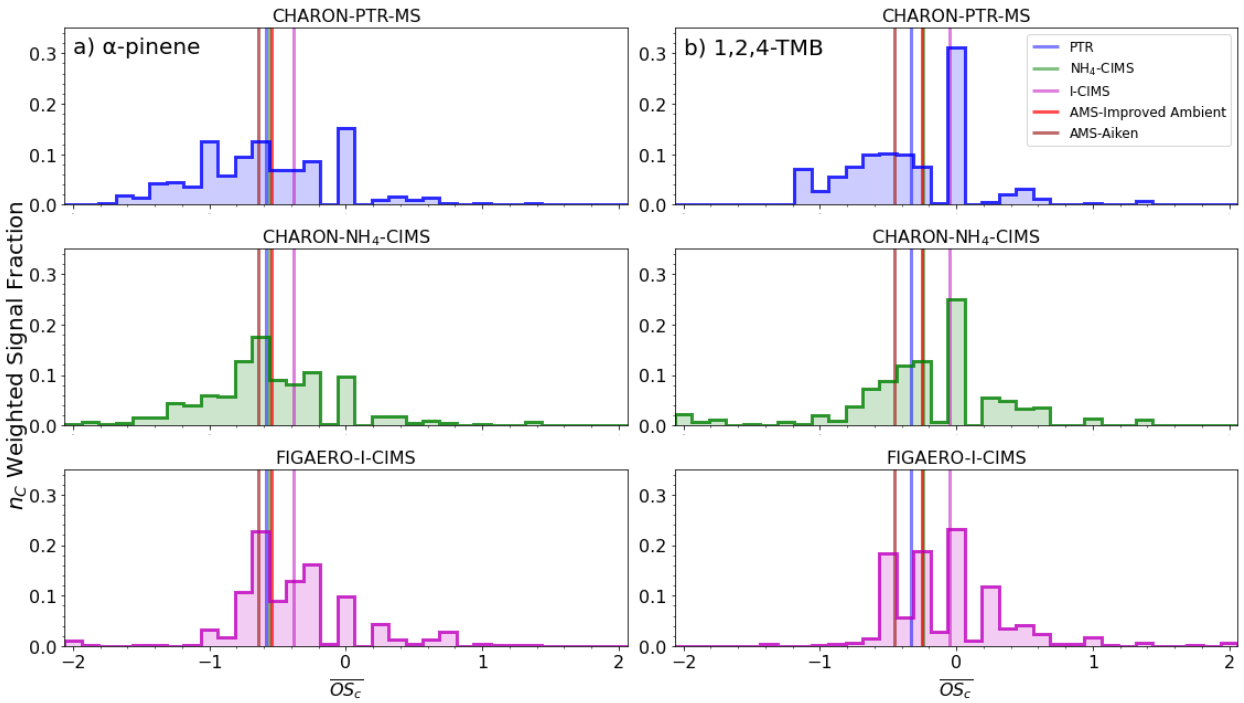

Figure 3.5: Oxidation state histograms of the a) α-pinene and b) 1,2,4-trimethylbenzne SOA. The three CIMS distributions roughly correspond to gaussian distributions around an average oxidation state value. The average oxidation state in AMS measurements, derived from the Aiken et al., 2007 and Improved Ambient methods are presented for comparison.

3.5 Conclusions and Future Work

We measured composition of SOA in laboratory oxidation experiments of α-pinene and 1,2,4-trimethylbenzene with 3 chemical ionization mass spectrometers, comparing the formulas and elemental properties of the species measured in each instrument. The distribution of products detected suggested differences in the chemical selectivity and extent of fragmentation between the CHARON-PTR-MS, CHARON-NH_4-CIMS, and FIGAERO-I-CIMS. The PTR detected primarily smaller molecular weight compounds with few functional groups, as suggested by the low oxygen number and limited organic nitrate signals. The small carbon numbers of these formulas imply that fragmentation during ionization produced the ions detected. The NH_4-CIMS detected more oxygenated compounds, organic nitrates, and higher carbon number compounds than the PTR. The carbon number distribution also implied lower levels of fragmentation. The I-CIMS detected higher molecular weight, multifunctional compounds, including organic nitrates and higher carbon-number compounds. Minimal fragmentation appeared to take place in the I-CIMS measurement. The differences in thermal desorption methods may have produced some effects on the composition of species detected but were not extensively probed in these experiments. Though different CIMS techniques for measuring aerosol produce markedly differing mass spectra through a combination of fragmentation and chemical selectivity, a key chemical property, average oxidation state, largely agrees between instruments for the chamber derived SOA we analyzed in this study, suggesting that selectivity of different compounds does not appear to impact the properties of SOA recorded in the different CIMS. One important

limitation of the characterizations in this study is that only two fresh SOA systems were assessed. Further characterization of biases towards more or less oxidized species could be probed by measuring SOA derived from more diverse VOC precursors, as well as more aged aerosols.

This study combined measurements using three ionization modes and two desorption techniques, introducing the possibility for both the differences in ionization and thermalization to influence the species which were detected. In order to better separate the influence of each, comparisons of multiple ionization schemes should be performed with the same desorption method, and the FIGAERO and CHARON inlets should be compared on two CIMS with the same ionization scheme. These sets of comparisons would isolate the influence of thermalization from ionization and more clearly identify the biases and limitations resulting from each component of a given particle-CIMS setup, refining the picture of the resulting chemical selectivity.

Further improvements to monitoring aerosol composition with CIMS have been achieved in recent years. The need to reduce thermal fragmentation has led to new sampling techniques being applied to CIMS measurements, such as Extractive Electrospray Ionization and the Vaporization Inlet for Aerosols (Lopez-Hilfiker et al., 2019; Zhao et al., 2024). However, a persistent limitation of CIMS techniques is the lack of generalizable calibrations. Sensitivities to individual classes of compounds vary by multiple orders of magnitude, and authentic standards are only available for select compounds. This lack of calibration makes the AMS measurements essential for aerosol quantification and speciation, in spite of its bulk properties being deficient for analysis of individual organic aerosol species. Future comparisons of multiple particle-phase measurements should focus on the possibility of using direct calibrations to impose constraints on the overall concentration (in terms of carbon content as well as particle mass) contributions of different classes of compounds, which will better indicate the relative strengths and biases of individual measurement techniques. A calibrated carbon closure comparison of total aerosol mass will constrain the relative abundance of key particle compounds and better characterize the significance of specific aerosol formation pathways.

Particle-CIMS techniques are a major advancement in the study of atmospheric organic carbon, permitting more focused study into mechanisms of particle formation and identification of species of interest, such as highly oxygenated molecules, organic nitrates, and higher carbon number accretion products. The selectivity of different ionization techniques directly impacts which compounds are detected, as demonstrated in this study. Because of the high costs and labor-intensive demands of operating and analyzing data from a CIMS, targeted studies of aerosol chemistry and composition will be best served by choosing an ionization scheme most equipped to measure the important products, a decision which will be often made before any data is collected. For example, if a study is interested in the formation of organic nitrates, NH_4-CIMS or I-CIMS will be most useful, whereas PTR-MS may not be able to detect multifunctional nitrate species. Similarly, studies of HOMs are likely to detect a number of compounds more efficiently by using I-CIMS. However, an experiment reporting on the composition of aerosol with only this instrument will be unlikely to report a significant contribution from less oxygenated products, whether or not they were formed or present in that system. There is necessarily a pre-biasing of results when choosing specific ionization schemes to report on distributions of compounds sensitive to that ionization scheme. These studies should be careful not to overemphasize the

impact of their results without considering contributions from unmeasured products to the entire chemical system. Meta-analyses of measurements from a given instrument across studies, and simultaneous deployment of multiple CIMS techniques should be used when possible, in order to corroborate and contextualize the conclusions derived from a single CIMS.

3.A Appendix

3.A.1 FIGAERO operation

FIGAERO-I-CIMS data was processed in Tofware version 4.0.1. Analyte peaks were fitted to masses which could represent carbon containing iodide adduct ions whose time-series behavior produced a thermogram pattern during the ramp cycles. Intensity of the signal was determined by integrating the thermogram area during the ramp cycle. Possibly due to a cold zone in the sampling setup, an erroneous gas-phase signal was observed during the beginning of the ramp cycle, superimposed upon the commonly gaussian thermogram signal. This was removed from the integrated signal intensity by fitting and subtracting a biexponential function from the affected timeseries (Figure 3.A.1).

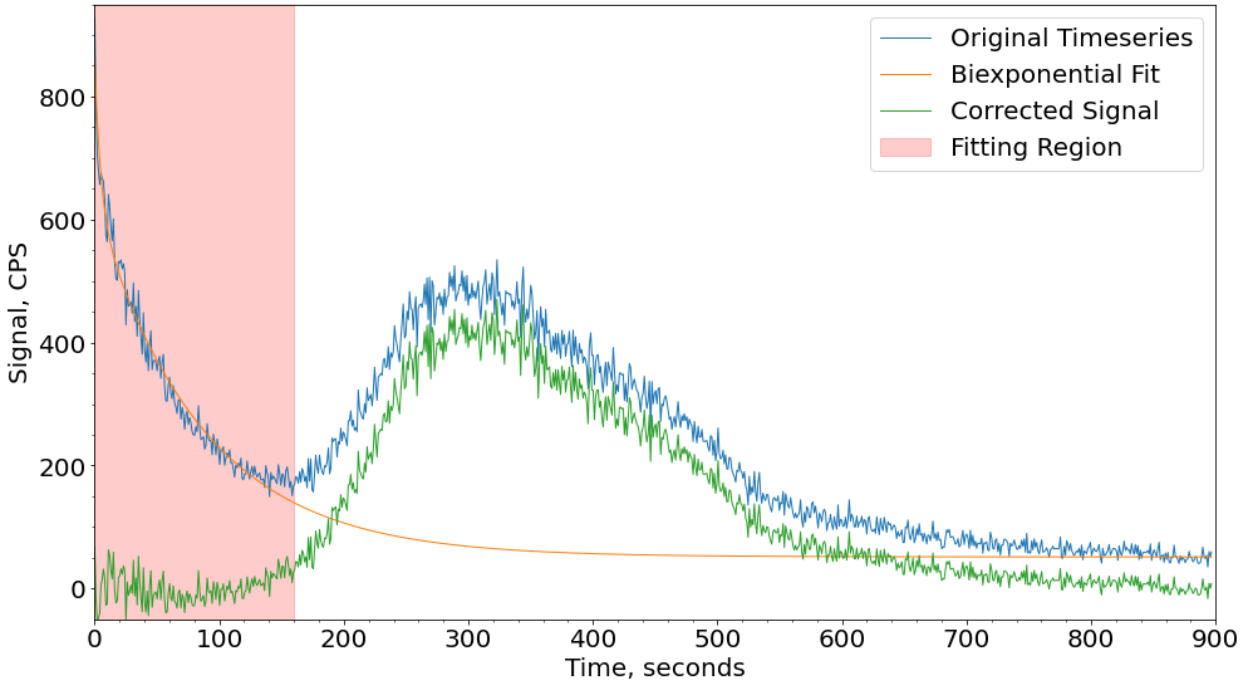

Figure 3.A.1: Example Correction for Transient Background. A biexponential function (orange) was fitted to the FIGAERO time series (blue) in the red shaded region and then subtracted to produce the gaussian trace (green) which was integrated to calculate instrument signal.

3.A.2 Precursor Decays

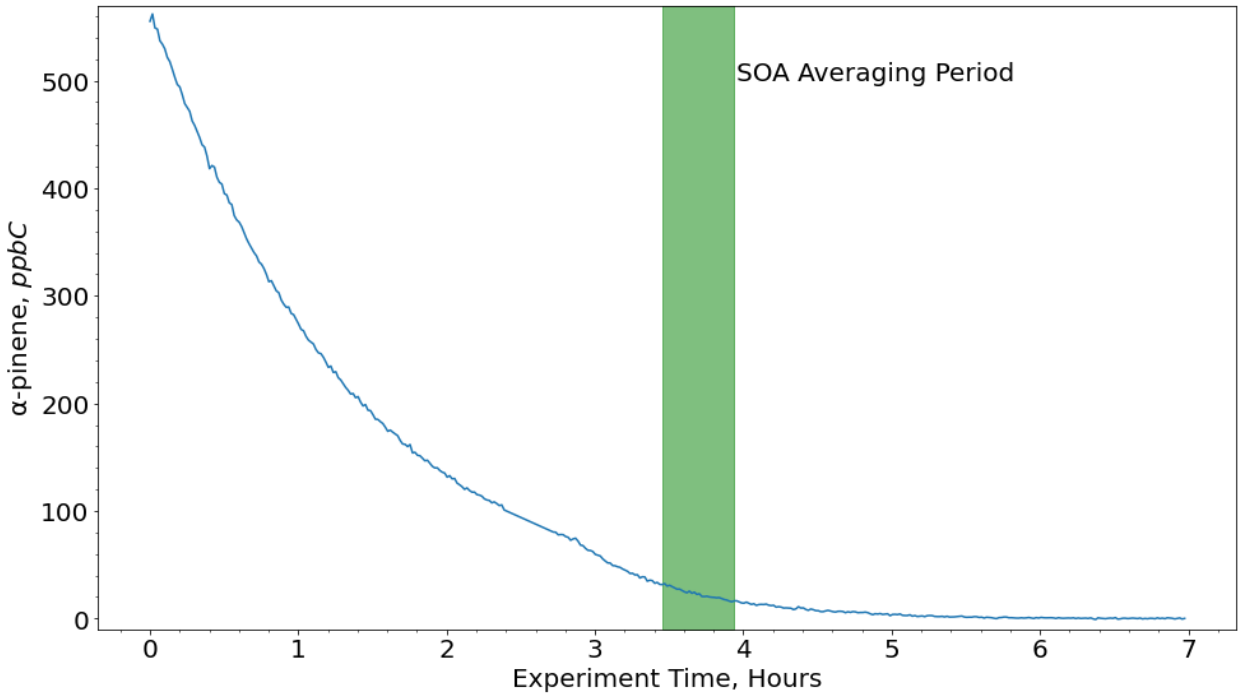

Figure 3.A.2: α-pinene precursor decay measured by the Vocus-PTR. Composition averages represent the green shaded region.

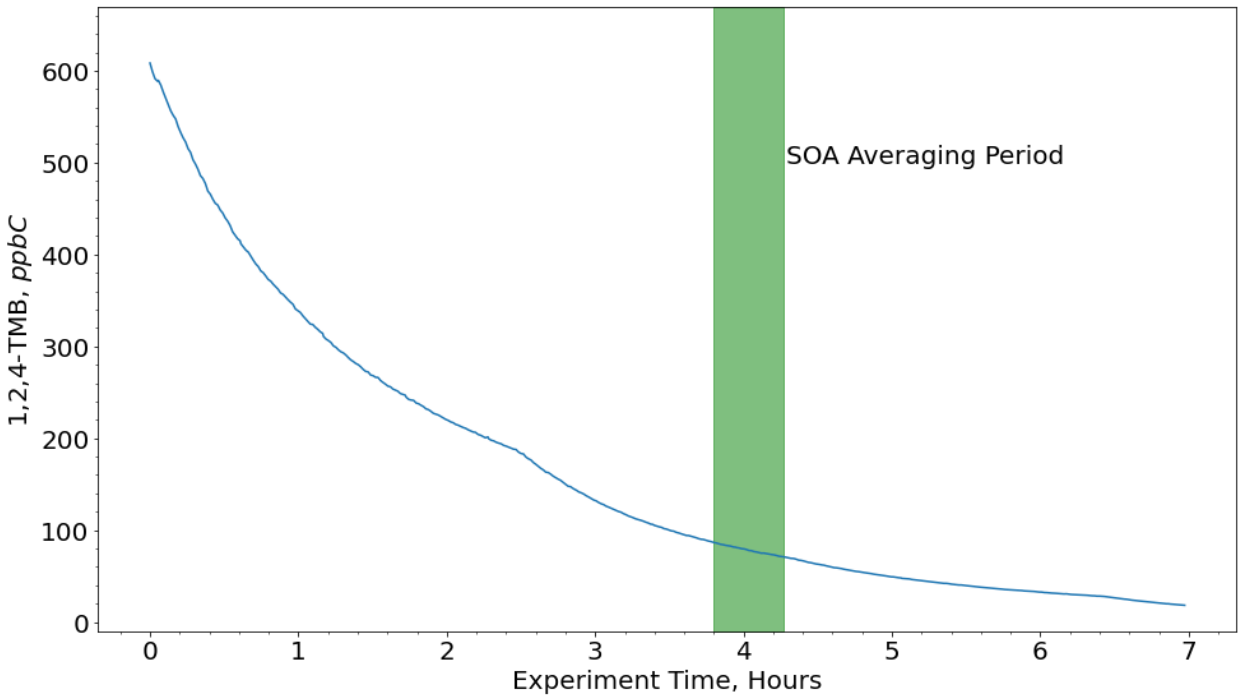

Figure 3.A.3: 1,2,4-trimethylbenzene precursor decay measured by the Vocus-PTR. Composition averages represent the green shaded region.

3.A.3 Generalized Kendrick Analysis

Visualization of mass spectral composition can be aided by calculating a "resolution enhanced Kendrick mass defect" (REKMD), separating small offsets from unit mass that represent key differences in formula against a single mass-to-charge axis. The REKMD is calculated as

$$REKMD\left(\frac{m}{z}, R, X\right) = \frac{m}{z} \times \frac{X}{R} - round\left(\frac{m}{z} \times \frac{X}{R}\right) \qquad (3.A.1)$$

where X is chosen to be 24 and R is ^{16}O or 15.995 (represented as GKA(m/z, ^{16}O, 24) (Alton et al., 2023).

3.A.4 Trimethylbenzene SOA Results and Elemental Analysis

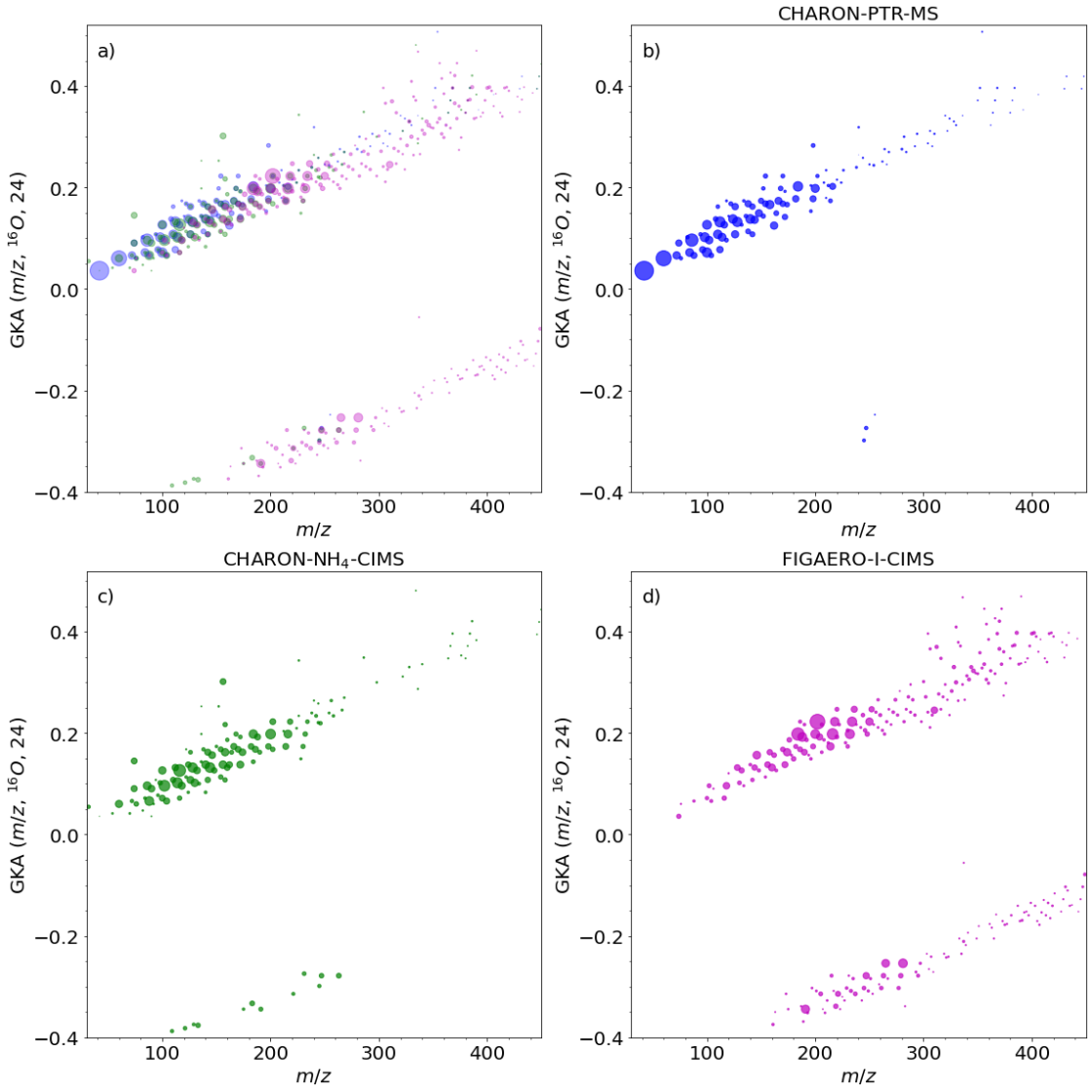

Figure 3.A.4. Generalized Kendrick Analysis plot of 1,2,4-Trimethylbenzene SOA (without H+, NH4+, or I-adduct) for a) three CIMS techniques overlaid, b) PTR-MS, c) NH4-CIMS, and d) I-CIMS. Positive GKA values correspond to even number masses (CxHyOz) and negative with odd masses (CxHyNOz). Circle size corresponds to the carbon weighted fraction of total ion signal.

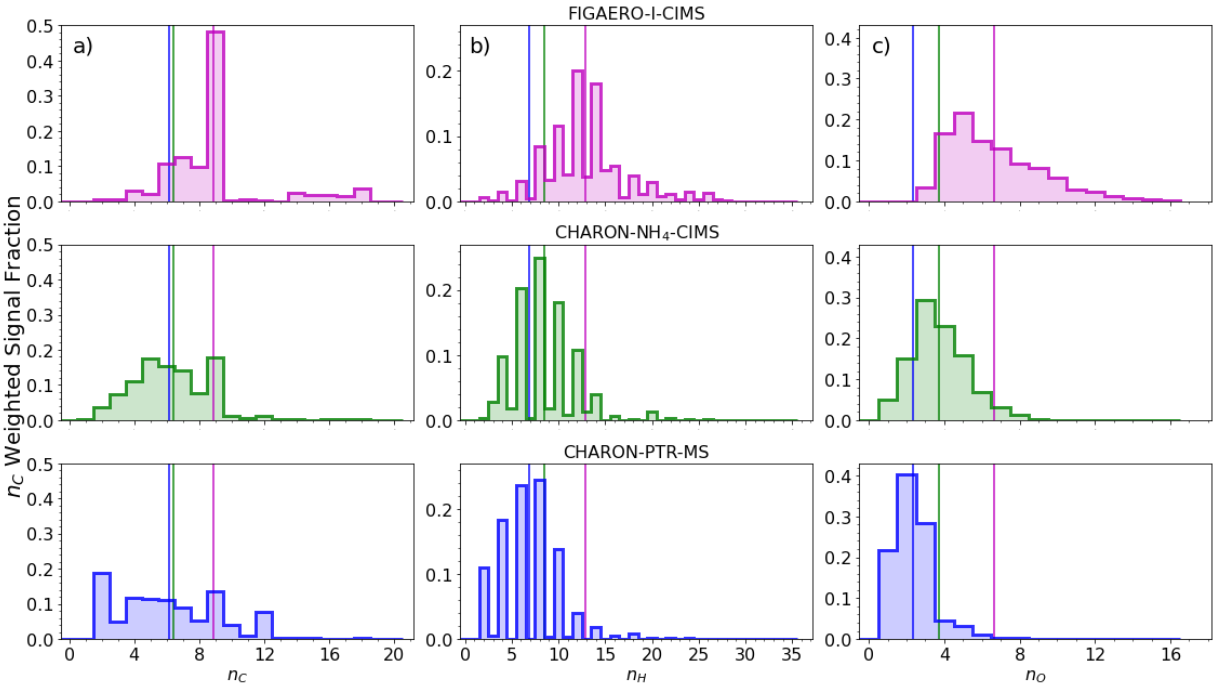

Figure 3.A.5. Product distributions of a) carbon, b) hydrogen, and c) oxygen number detected by FIGAERO-I-CIMS (top row), CHARON-NH4-CIMS (middle), and CHARON-PTR-MS (bottom) in the 1,2,4-TMB oxidation experiment.

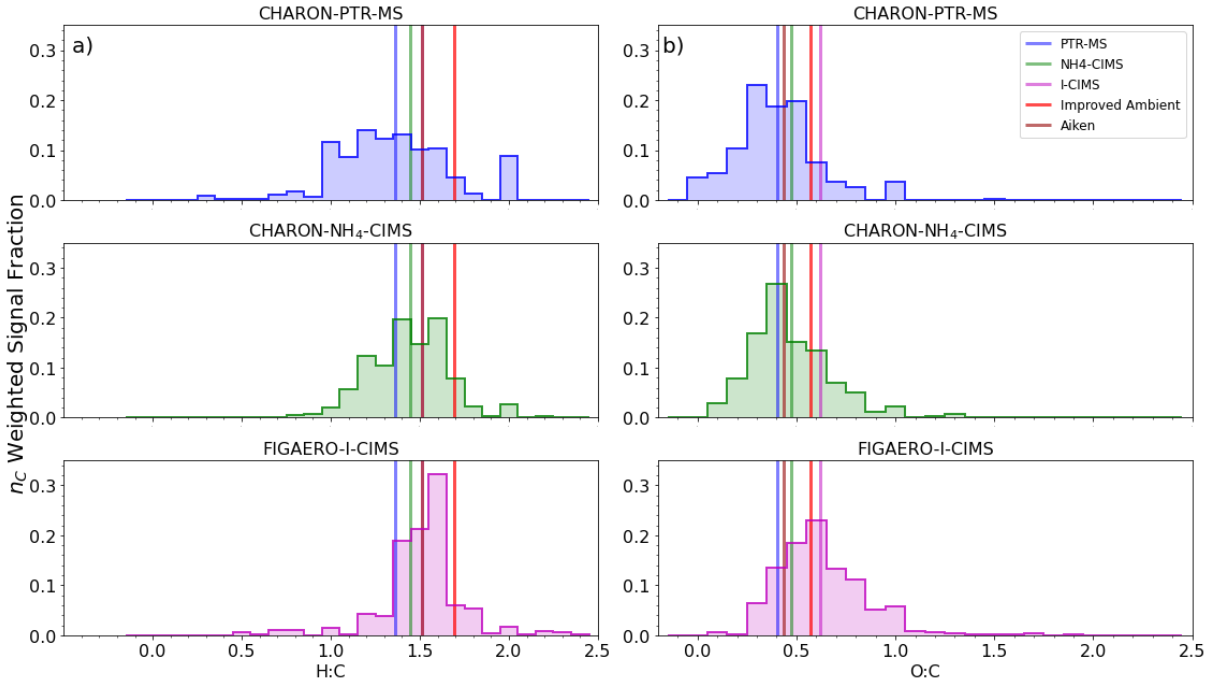

Figure 3.A.6. a) H:C and b) O:C Histograms in the α-pinene oxidation experiment for CHARON-PTR-MS, CHARON-NH4-CIMS, and CHARON-PTR-MS. Averages are indicated by vertical lines for each distribution, along with the calculated AMS O:C ratio given by both the Aiken et al., 2008 and Improved Ambient calculations.

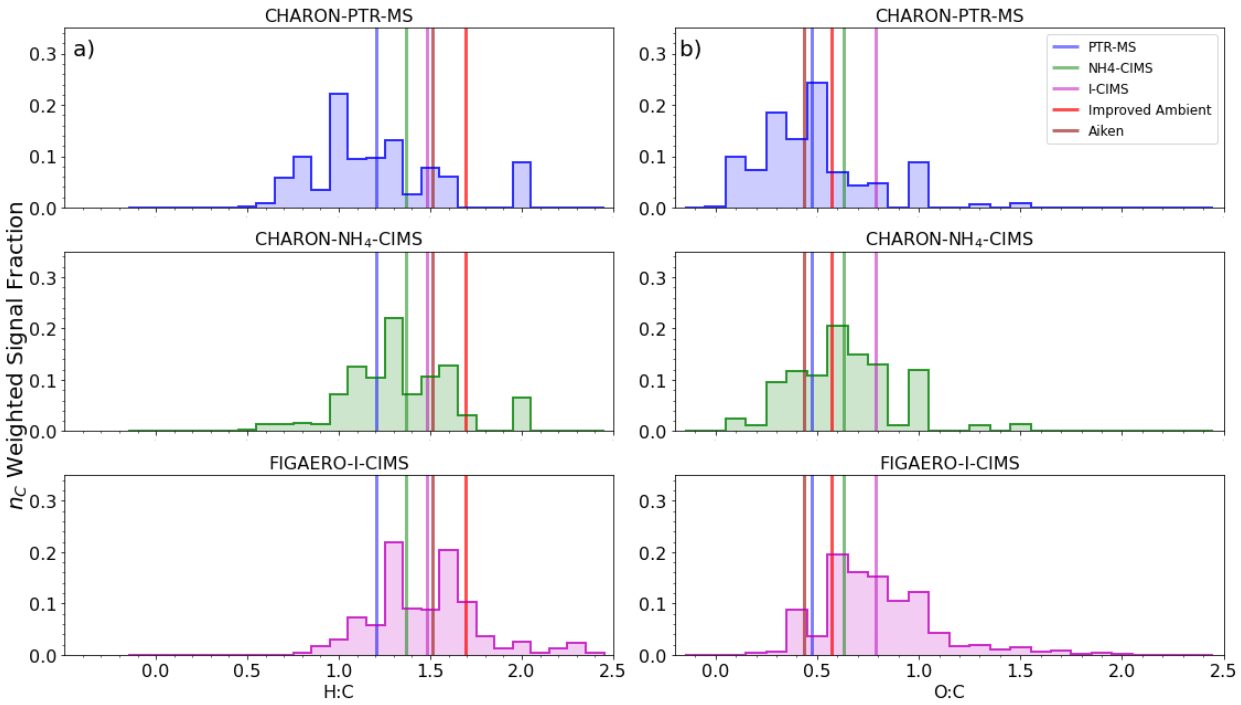

Figure 3.A.7: a) H:C and b) O:C Histograms in the 1,2,4-Trimethylbenzene SOA experiment for CHARON-PTR-MS, CHARON-NH4-CIMS, and CHARON-PTR-MS. Averages are indicated by vertical lines for each distribution, along with the calculated AMS O:C ratio given by both the Aiken et al., 2008 and Improved Ambient calculations.

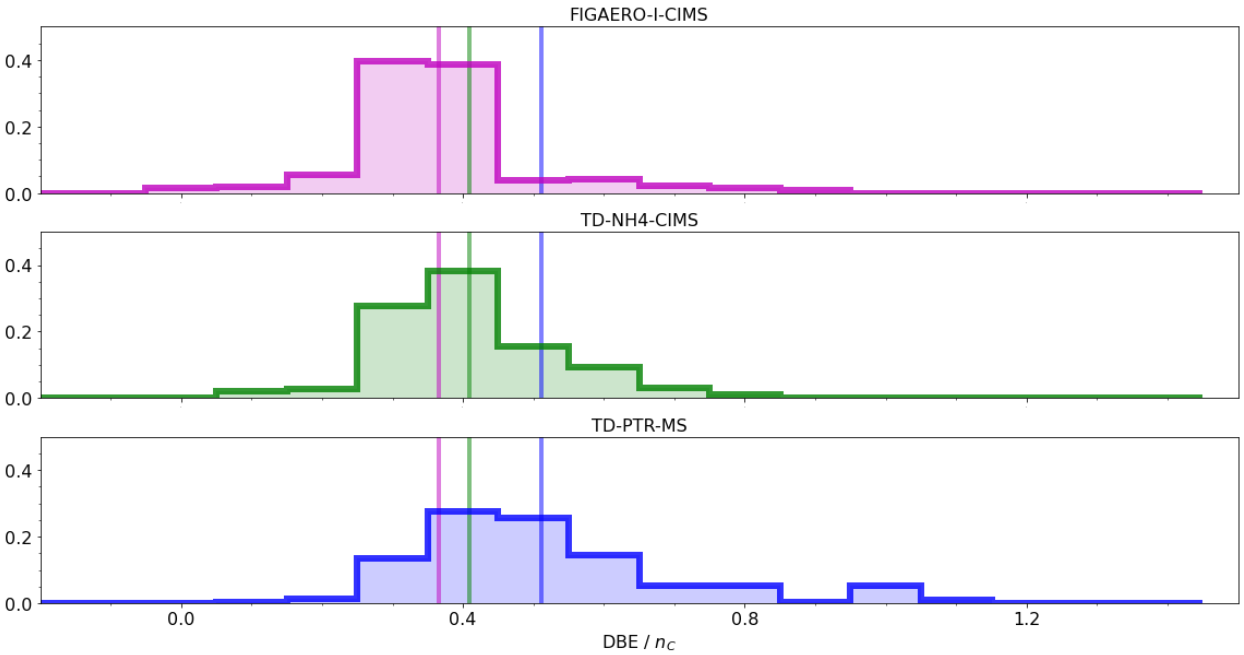

Figure 3.A.8: DBE per carbon number histograms for α-pinene experiment.

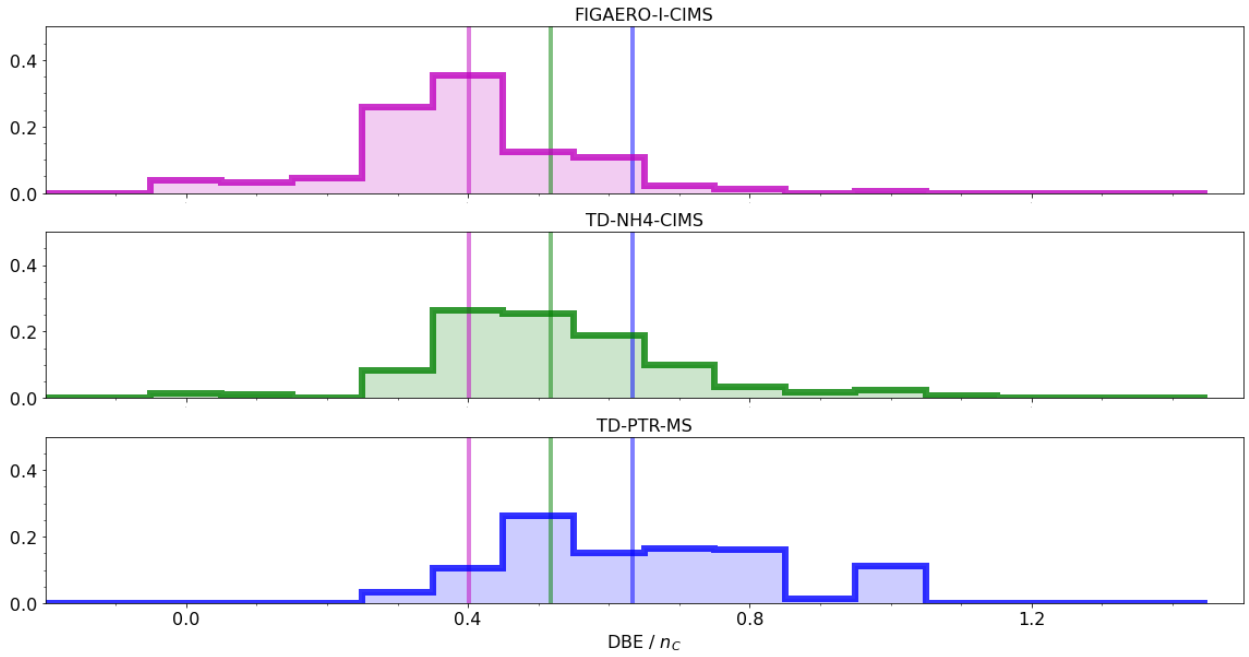

Figure 3.A.9: DBE per carbon number histograms for 1,2,4-TMB experiment.

Chapter 4: Impacts of Varying Multiple Peroxy Radical Pathways on Secondary Organic Aerosol Composition

4.1 Chapter Abstract

The fates of organic peroxy radicals (RO_2) represent key branch points in the formation of reaction products, including low-volatility species that contribute to secondary organic aerosol (SOA), a major fraction of atmospheric particulate matter. Though aerosol composition has long been studied both in field measurements and laboratory studies, there has been relatively little systematic exploration of how variations in RO_2 chemistry influence the chemical composition of the SOA. To investigate these impacts, we conducted a series of α-pinene oxidation chamber experiments, in which oxidation conditions were chosen to promote different relative rates for the RO_2+NO, RO_2+HO_2, RO_2+RO_2, and isomerization pathways, respectively. These experiments include limiting cases dominated by the RO_2+NO and RO_2+HO_2 pathways, as well as intermediate cases where more RO_2+RO_2 chemistry is accessed. Extractive Electrospray Ionization Time of Flight Mass Spectrometer (EESI-ToF-MS) is used to monitor the composition of SOA in real time. Differences in particle-phase products, particularly nitrates, hydroperoxides, and dimers, make the dependence of initial SOA composition on RO_2 pathways clear. We discuss the evolution of SOA with time, which shows that changes in the particle composition tend to increase the convergence of spectra formed under different RO_2 regimes, though some differences persist. This study emphasizes the importance of considering contributions of different RO_2 pathways when designing simulations of oxidation conditions and SOA formation.

4.2 Introduction

Secondary organic aerosol (SOA), consisting of low volatility species produced from the oxidation of volatile organic compounds (VOCs), is a major contributor to global particulate matter. Aerosols are an important risk factor for human health (Landrigan et al., 2018; Pozzer et al., 2023), and they influence the climate through direct and indirect effects (Intergovernmental Panel On Climate Change (IPCC), 2023). Despite its identification as a major contributor to pollutant formation, the chemical behavior of VOCs, spanning up to hundreds of thousands of unique compounds, is difficult to assess systematically or represent in chemical mechanisms, as most reactions are unconstrained. While identification of every reaction is infeasible, branch points in chemistry of VOC reactions are useful areas of study for increasing our knowledge about common aerosol forming systems and for reproducing their behavior more accurately in models.

Reactions of VOCs with the hydroxyl radical OH (though other species such as O_3 and NO_3 are can also serve as oxidants) form an alkyl radical, followed by the rapid addition of O_2 to produce a peroxy radical (RO_2) (Atkinson, 1986). The fate of the reactive intermediate peroxy radical is a key branching point in the degradation mechanism and so determines the functional forms of the chemical products produced, as shown in Figure 4.1. When NO_x is present, RO_2 reaction with nitric oxide (NO) will produce alkoxy radicals (RO) or organic nitrates ($RONO_2$). Reaction with the hydroperoxyl radical (HO_2) produces hydroperoxyl-acids (ROOH). The lower potential volatilities resulting from nitrate and hydroperoxyl groups have led to focuses on these

products and their impact on SOA (Capouet & Müller, 2006; Matsunaga & Ziemann, 2009; Lee et al., 2016). Reaction with other RO_2 species can produce a dimer recombination product (ROOR), form an aldehyde (R=O) and alcohol (ROH), or produce two alkoxy radicals (Salo et al., 2022). Dimeric compounds and other accretion products such as esters are similarly identified as an SOA forming pathway (Ehn et al., 2012; Peräkylä et al., 2023). Finally, isomerization, a class of unimolecular rearrangements such as hydrogen shifts, is a pathway that results in subsequent peroxide group formation ($R'O_2$). Multiple isomerization reactions can proceed sequentially, leading to highly oxygenated molecules (HOMs) and contributing to SOA (Peeters et al., 2009; Crounse et al., 2013; Bianchi et al., 2019). For RO_2 with certain functional groups such as carbonyls, additional chemical pathways are relevant (Barber & Kroll, 2021). If the RO_2 produced is an acylperoxy radical (R-C(O)O_2), reaction with NO_2 can produce peroxyacetyl nitrates (PANs), which are important atmospheric reservoirs of reactive nitrogen, though these products can easily thermally decompose at warmer temperatures (Singh & Hanst, 1981; Nozière & Barnes, 1998). Acylperoxy radicals may also react with HO_2 to form alcohols or alkoxy radicals (Tomas et al., 2001; Sulbaek Andersen et al., 2003; Hasson et al., 2004). Alkoxy radicals quickly isomerize to another alkyl radical and produce a subsequent peroxy radical ($R'O_2$), therefore allowing for sequential radical reactions and additional oxidation. Variation in oxidation conditions, depending on the relative rates and branching ratios for a given VOC, may therefore result in different classes of products from differing RO_2 fates contributing to SOA formation.

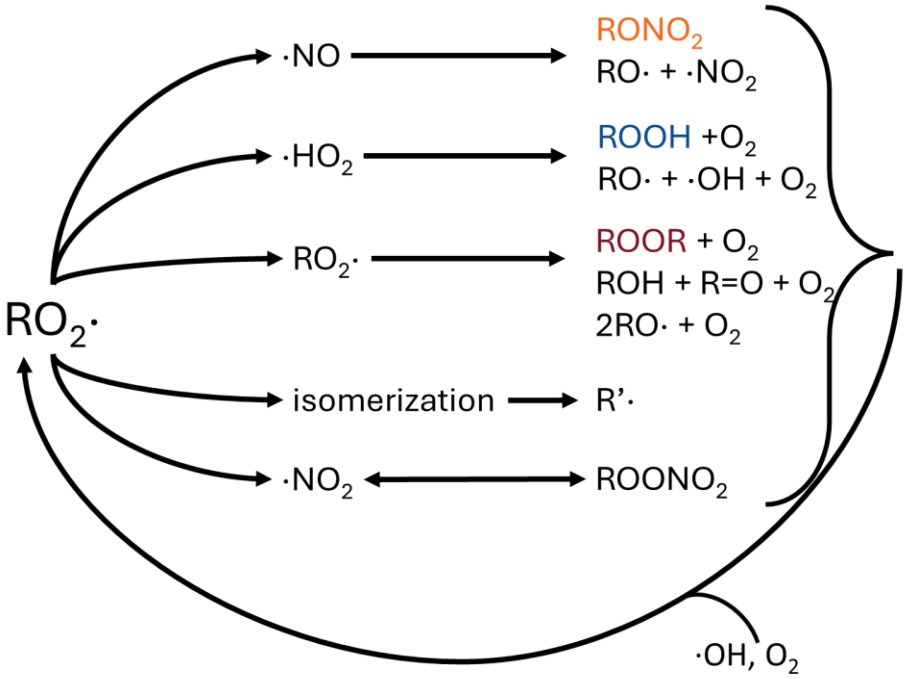

Figure 4.1: Major unimolecular and bimolecular fates of RO_2 radicals. Key functionalized compounds are nitrates ($RONO_{2,}$) hydroperoxides (ROOH), and dimers (ROOR).

Because only sufficiently low volatility oxidation products will contribute to the overall burden of SOA, identifying RO_2 pathways which favor aerosol production has been a topic of interest since the identification of NO_x as a controlling influence on SOA chemistry (Presto et al.,

2009). Atmospheric chamber studies of the formation of different secondary organic aerosols were used to characterize yields of SOA formation from isoprene, monoterpenes such as α-pinene, and aromatic hydrocarbons (Kroll et al., 2005, 2006; Presto et al., 2005; Surratt et al., 2006; Ng, Kroll, et al., 2007; Chan et al., 2009). These yields were generally calculated in experiments under low and high NO_x conditions, assuming that under low NO_x conditions peroxy radicals would react with HO_2, and under high NO_x conditions, they would react with NO. When implemented in models, intermediate conditions between the low and high NOx pathways were linearly parameterized as a combination of these limiting conditions (Henze et al., 2008; Pye et al., 2010). Under this framework, intermediate RO_2 conditions can be described by the branching ratio β between NO and HO_2 rates:

$$\beta = \frac{k_{RO_2+NO}[NO]}{k_{RO_2+NO}[NO] + k_{RO_2+HO_2}[HO_2]} \qquad (4.1)$$

Products in the gas- and particle-phase are then derived from the high- and low-NO_x parameterizations in proportion to β. Including branching pathways for aerosol yield based upon RO_2 fate had differing implications for yields from isoprene (higher at low-NO_x) and for monoterpenes and aromatic hydrocarbons (higher at high-NO_x). Nevertheless, if this assumption holds, then aerosol formation should be accurately generalizable, assuming representative VOC oxidation systems are studied under both high and low NO_x conditions. As implemented, there are still large uncertainties in constraining SOA burdens in models, which do not necessarily improve with more descriptive chemistry models (Pai et al., 2020). One potential problem with these prior parameterizations is that limitations of chamber dilution and instrument sensitivity required experiments to be conducted with high oxidant and precursor levels, likely limiting the influence of isomerization reactions. Therefore, the role of additional RO_2 pathways is potentially missing from model parameterizations of SOA.

Though the importance of composition for aerosol properties such as toxicity, optical scattering/absorption, and hygroscopicity is well understood, SOA composition as a function of RO_2 chemistry has been relatively unexamined compared to gas-phase oxidation products. Particle-phase products have been analyzed in prior studies of OH oxidation of terpenes such as α-pinene under different NOx conditions by offline techniques following filter collection (Ng, Chhabra, et al., 2007; Eddingsaas et al., 2012). Other studies have focused upon the identification of specific isomerization pathways of RO_2 radicals in order to generate HOMs (Xu et al., 2019; Lee et al., 2023; H. Yang et al., 2025). Dimerized compounds arising from RO_2 reactions with other RO_2 have been similarly recognized as an efficient path for lowering the volatility of the aerosol species (Ehn et al., 2014), though concern has been expressed over this pathway being overrepresented in laboratory experiments (Schervish & Donahue, 2021; Baker et al., 2024). Studies which identified the significance of RO_2 fate for particle-phase composition have tended to focus on limiting conditions (Bates et al., 2022; Day et al., 2022; Q. Ye et al., 2022; D. Li et al., 2024). The implications of intermediate conditions for the particle phase have been primarily focused on yields, rather than compositional effects. Newer studies have emphasized the utility of online measurements for tracking the evolution of particle-phase composition (Pospisilova et al., 2020) but to our knowledge, there has not been a study investigating the impact of RO_2 chemistry on the real-time composition of SOA. Potential changes in the chemistry of SOA from

the multiple available RO_2 pathways are under-constrained. Furthermore, the possibility of nonlinear chemistry, in which compounds resulting from cross reactions of different radical paths contribute to particle composition, has not been explored.

We conducted a series of OH-oxidation experiments of α-pinene in order to investigate the role of RO_2 conditions in modifying gas- and particle-phase chemistry. These experiments survey competition between the two pathways (at both limiting and intermediate values of β). Additionally, we survey changes in the overall rates of both reaction pathways, represented by a second chemical parameter, $\tau_{NO,HO2}$, the combined bimolecular lifetime of RO_2+NO and RO_2+HO_2 reactions:

$$\tau_{NO,HO_2} = \frac{1}{k_{RO_2+NO}[NO] + k_{RO_2+HO_2}[HO_2]} \qquad (4.2)$$

At longer values of $\tau_{NO,HO2,}$ various isomerization, RO_2+RO_2 and RO_2+NO_2 reactions limited under higher oxidant concentrations may become competitive with the RO_2+NO and RO_2+HO_2 pathways (Teng et al., 2017). In order to explore the impacts on particle-phase products, extractive electrospray ionization time of flight mass spectrometry (EESI-ToF-MS), a particle-phase measurement with low reported fragmentation rates, monitored SOA composition in real time (Lopez-Hilfiker et al., 2019). We compare the spectra measured in different experiments to investigate how the branch point of peroxy radical chemistry controls SOA composition. We look at the differences in the major products detected, and at the relative formation of organic nitrates, hydroperoxides, and dimers. We then discuss the evolution of the SOA composition in time, and the possibility of using compositional markers of RO_2 formation conditions in studies of ambient aerosol.

4.3 Methods

In all experiments, α-pinene was oxidized by OH in the MIT environmental chamber (Hunter et al., 2014). Experiments were performed in semi-batch mode. The chamber was filled with clean air from a zero-air generator (Tisch Environmental 737 Series) and replenished at a rate of 12 liters per minute, replacing the sample intake flow to the instruments used. The chamber was humidified to 60% by flowing a portion of the clean air stream through a bubbler containing Milli-q water.

Before each experiment, dry ammonium sulfate seed aerosol was introduced into the chamber by bubbling ammonium sulfate solution through an atomizer and drier for several minutes. Then, hexafluorobenzene was added to serve as a dilution tracer by gas-tight syringe injection, followed by 70-180 ppb of α-pinene added by gas-tight syringe injection through an inlet heated to 100°C. After the concentration of α-pinene stabilized, oxidant precursors were added to the chamber, usually in the order of nitrous acid (HONO), nitric oxide, and hydrogen peroxide; concentrations were chosen to access a particular RO_2 fate, as discussed below. OH was generated by two methods depending on the experiment: photolysis of HONO and H_2O_2. HONO was produced by addition of sulfuric acid to a sodium nitrite aqueous solution in an airtight flask and sampling the headspace. H_2O_2 was added by a single gas-tight syringe injection to an input flow stream. Nitric oxide was introduced by adding a controlled flow from a gas standard.

HONO concentrations were estimated from the difference between the NO_2 measurement in a chemiluminescence instrument (Thermo Scientific), which is cross-sensitive to NO_y, and the NO_2 concentration measured by a CAPS NO_2 instrument (Aerodyne Research). NO concentrations were also monitored with the chemiluminescence monitor. A measurement of H_2O_2 concentrations was not available, so initial concentrations were estimated based upon the volume of H_2O_2 solution injected into the chamber. Photochemistry was initiated by the 40 UV lights surrounding the chamber, each centered around a 245 nm wavelength. Once all of these components were added and baseline concentrations had been established, the UV lights were turned on, initiating chemistry in the chamber, and the experiment was run for 7 to 8 hours.

A suite of instruments was used to monitor gas- and particle-phase composition of the α-pinene oxidation system. A Vocus-PTR (Aerodyne Research) was used to monitor the decay of α-pinene (J. Krechmer et al., 2018). Particle-phase composition was measured by an Aerosol Mass Spectrometer (DeCarlo et al., 2006) and an EESI-ToF-MS (EESI) (DeCarlo et al., 2006; Lopez-Hilfiker et al., 2019). The EESI removes gas-phase species by passing an inlet flow through a charcoal denuder. After this, a spray of sodium iodide salt in acetonitrile and water solution to dissolve and ionize soluble components of the sampled particles. This stream passes through a capillary heated to 190°C, evaporating the solvent and producing an ion gas of adducts of Na^+ and the particle-phase compounds. The EESI was optimized for product signal to noise by sampling a levoglucosan ($C_6H_{10}O_5$) standard and optimizing the average levoglucosan-sodium adduct mass signal (counts per second) for differing voltage settings in the mass-spectrometer with the Thuner software. Both particle-phase composition measurements sampled chamber air downstream of a thermodenuder (Huffman et al., 2008). This permitted regular switching between a high temperature sampling line and a bypass. The volatilized species produced a characteristic pattern in the signals detected in the EESI, facilitating identification of particle-phase signals from instrument background signals. High resolution analysis of the aerosol peaks was performed using Tofware v4.0.1. Peaks were included in this analysis if they responded to the changes in the thermodenuder and fitted as sodium adducts to closed shell organic molecules with formulas corresponding to $(Na)C_{3\text{-}22}H_{0\text{-}34}N_{0\text{-}1}O_{0\text{-}12}^+$ (Figures 4.A.1 and 4.A.2). The average signal before the chemistry is initiated is subtracted as background from each timeseries. The EESI varies in sensitivity to different compounds by orders of magnitude (Lopez-Hilfiker et al., 2019), so the analysis performed here is of relative signal intensities between experiments, rather than calibrated concentrations.

In order to control the RO_2 chemistry in each experiment and determine appropriate concentrations of the oxidant precursors, we use a modeling approach for designing experiments described in a prior publication (Kenagy et al., 2024). Iterative F0AM chemical modeling, using the Master Chemical Mechanism version 3.3.1 was used to simulate chamber RO_2 chemistry under a range differing initial conditions (Wolfe et al., 2016). Chemistry was simulated in each experiment for 8 hours of oxidation under dilution and UV flux conditions matching the MIT chamber. Final concentrations of α-pinene, the median OH exposure, and the relative rates of RO_2+NO, RO_2+HO_2, RO_2+RO_2 and known isomerization reactions were saved. From these rates, β was calculated by integrating the NO and HO_2 rates over the entire experiment time and then combining them as in Equation 4.1. A median $\tau_{NO,HO2}$ was calculated from the combined rates of the NO and HO_2 reactions as in Equation 4.2. Both parameters evolve over time due to changing

concentrations of RO_2 and the various oxidants. Experimental initial conditions were chosen in order to achieve a full range of β values from 0 to 1, and at least two orders of magnitude in $\tau_{NO,HO2}$, from 0.1-100s. Following each experiment, the measured concentrations in the laboratory chamber would be used to rerun F0AM simulations, reproducing the most accurate estimation of β and $\tau_{NO,HO2}$. Limiting experiments with primarily RO_2+NO chemistry β=1 and a short $\tau_{NO,HO2}$=0.1-10s and RO_2+HO_2 chemistry β=0 and a short $\tau_{NO,HO2}$=0.1-10s could then be compared to experiments with intermediate values of β and longer $\tau_{NO,HO2}$ on the order of 10-100s. Aerosol is generated in all experiments, corresponding to increases in organic signal in the AMS and growth of organic ion signals in the EESI. In order to achieve the desired peroxy radical fates, overall OH exposure varied between experiments. Consequently, there was variation in the decay of α-pinene from experiment to experiment (Figure 4.A.3). In order to compare similar rates of oxidation, different experiments are compared at equivalent levels of α-pinene decay measured by the Vocus-PTR. In Experiments 1 and 2, the furthest extent of oxidation achieved was 60%, so this is the extent of oxidation examined in this study.

Concentrations of ozone increased over most experiments as a byproduct of OH oxidation with α-pinene, with final concentrations as high as 50 ppb in one experiment. Reaction with O_3 was never a major channel for α-pinene loss; modeling suggests this accounts for less than 10% off the overall oxidation of α-pinene in all experiments. Similarly, the modeled loss to NO_3 accounted for less than 10% of the total reaction. Therefore, the SOA produced primarily reflects the products from the OH+α-pinene reaction, especially during earlier periods of the experiment (Figure 4.A.4).

4.4 Results and Discussion

4.4.1 Estimation of RO_2 Conditions

The initial conditions and estimated chemical parameters of all experiments are listed in Table 1. The values of β and $\tau_{NO,HO2}$ are reported at 10% and 60% of α-pinene loss. β is calculated as the integrated ratio of primary RO_2 fates for each experiment between the NO and HO_2 pathways, whereas $\tau_{NO,HO2}$ is described as the median lifetime from the start of oxidation to the cutoff reflective of a given amount of oxidation. The experiments span a range in β from 0.11 to 0.99, including both near-limiting and intermediate cases for the competition between NO and HO_2 for reaction with RO_2. Residual HONO off-gassing from the chamber walls is likely responsible for residual NO concentrations in experiments 1 and 7, where HONO and NO were not added: this results in higher β values than anticipated. The experiments cover 2 orders of magnitude in $\tau_{NO,HO2}$ from 0.29-111.0s.

Expt.	$\beta_{10\%}$	$\beta_{60\%}$	$\tau_{NO,HO2\ 10\%}$ (s)	$\tau_{NO,HO2\ 60\%}$ (s)	α-pinene (ppb)	O_3 (ppb)	HONO (ppb)	NO (ppb)	NO_2 (ppb)	H_2O_2 (ppb)	$NH_4(SO_4)_2$ (μg/m^3)
1	0.16	0.07	10.3	11.0	124.4	3.0	0.03	1.8	1.0	6458	27.7
2	0.21	0.11	9.5	10.6	126.6	1.7	0.4	2.8	1.6	6458	25.4
3	0.62	0.39	17.3	111.0	136.1	0.5	3.9	1.3	2.7	1256	29.4
4	0.52	0.45	14.0	26.3	137	2.3	9.3	0.7	3.1	2321	26.6
5	0.73	0.70	8.7	12.4	98.6	2.5	20.6	1.2	4.1	850	30.4
6	0.99	0.73	0.5	68.2	178.3	0.6	0.7	19.3	4.4	300	33.1
7	0.95	0.82	2.4	6.7	75.2	2.1	8.8	3.0	21.4	950	26.7
8	0.99	0.85	0.4	6.4	141.5	0.7	24.7	23.2	6.6	353	24.4
9	0.99	0.99	0.06	0.29	110.7	0.5	40.0	83.8	11.5	31	24.0

Table 4.1: Summary of Experimental Conditions. Initial concentrations of α-pinene, O_3, HONO, NO, NO_2, estimated H_2O_2, and $NH_4(SO_4)_2$. β and $\tau_{NO,HO2}$ are reported at 10% and 60% of α-pinene loss.

Figure 4.2 shows the RO_2 experiments in Table 4.1 plotted in chemical space by their estimated β and $\tau_{NO,HO2}$. To demonstrate the changes in RO_2 chemistry that occur over the course of the experiments, each experiment is plotted at 10% increments of precursor loss. For the low β experiments (#1 & 2) there is little change in $\tau_{NO,HO2}$ but a decrease of about 0.1 in β. For the high β (Experiment 9), $\tau_{NO,HO2}$ increases from a value of 0.06s to 0.29s. In most other intermediate cases (Experiments 3-4 & 6-8) there is a combination of decreases in β on the order of 0.1-0.2 and increases in $\tau_{NO,HO2}$ of up to 60-100s. When comparing the SOA spectra recorded at initial conditions, as well as changes in composition over time, the evolution of the RO_2 regime needs to be taken into consideration.

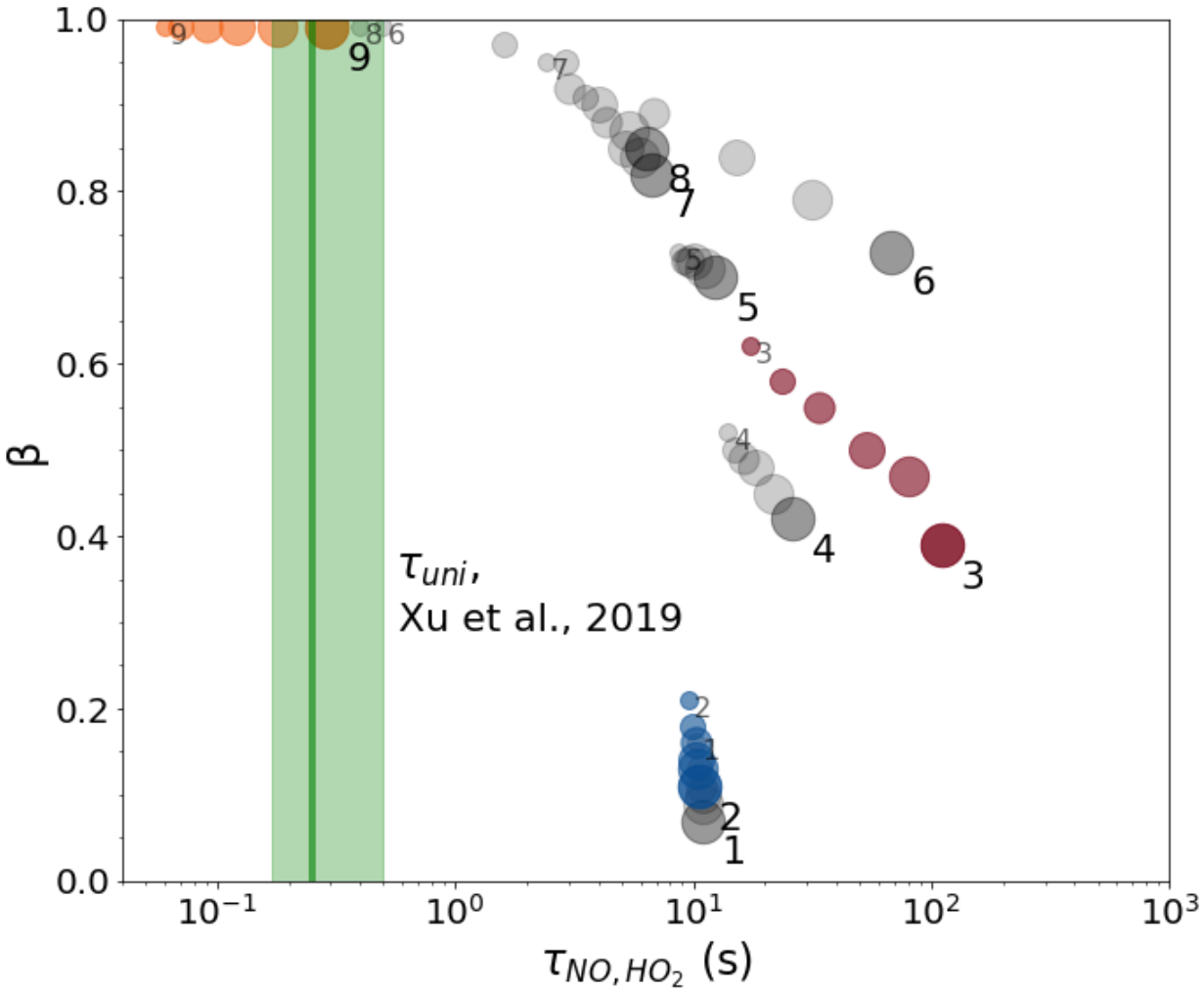

Figure 4.2: Evolution of chemical regime in β and $\tau_{NO,HO2}$ space for each experiment in Table 1 from 10% precursor oxidized to 60% precursor oxidized, with the points increasing in size and darkening with further oxidation. Case experiments 1 (blue) 3 (brown) and 9 (orange) are highlighted.

Some constraints from existing work inform the possible role of isomerization for the α-pinene peroxy radicals generated in this study, which are shown in Figure 4.3. Xu et al., 2019 determined a rate for isomerization for the ring opened peroxy radical (Figure 4.3c) of 4 ± 2 s^{-1}. This isomerization lifetime is shaded in green on Figure 4.2 (0.17-0.5s). With the exception of the high β, low $\tau_{NO,HO2}$ experiment (9) and the initial conditions in experiments 6 and 8, the bimolecular RO_2 pathways should not be competitive with isomerization for this peroxy radical, and therefore all products of this pathway should result from the isomerization reaction. The Xu et al. results suggest that the two other OH-addition derived peroxy radicals (Figure 4.3a and 4.3b), which make up 66% of the peroxy radical yields, do not have isomerization pathways which are competitive with a τ_{NO} of 3-40s, and so these pathways should be available for reaction with NO, HO_2, and other RO_2. Even longer isomerization rates could become competitive at longer values for $\tau_{NO,HO2}$ that were achieved in the experiments in this study; however they would still be competing with reactions of RO_2+RO_2, a parameter which was not constrained by $\tau_{NO,HO2}$. To

our knowledge, no isomerization reactions have been proposed or measured for the peroxy radicals resulting from hydrogen abstraction (Figure 4.3d and 4.3e), which should make up 12% of the derived peroxy radicals, so these fates are not constrained for the range of $\tau_{NO,HO2}$ values accessed.

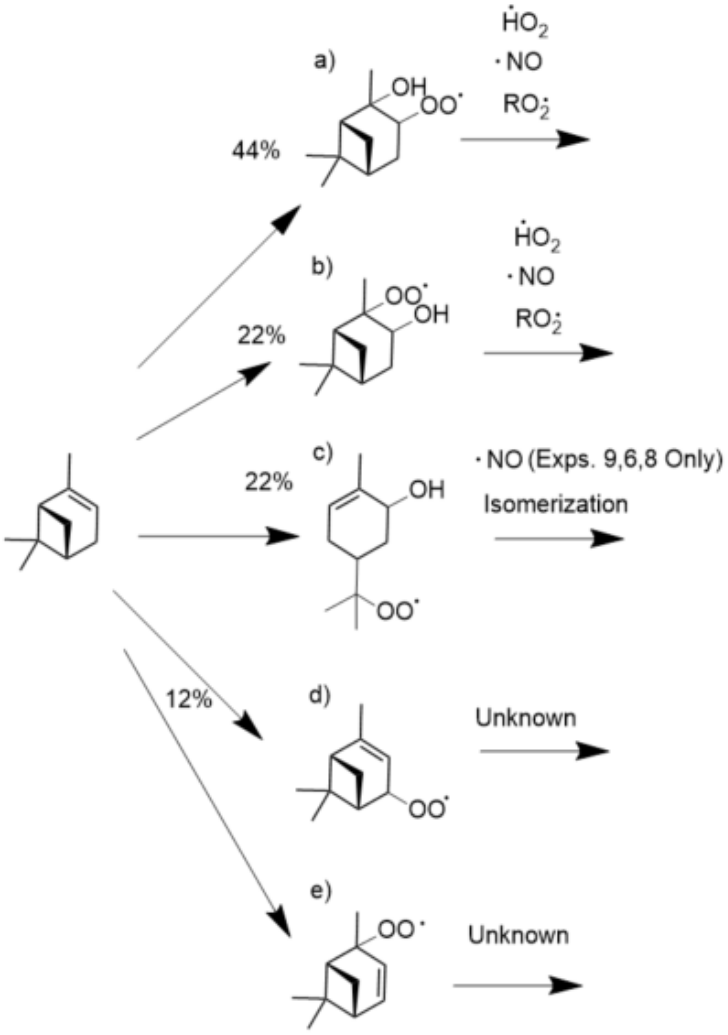

Figure 4.3: Available reaction pathways for α-pinene derived peroxy radicals. The two peroxy radicals from OH addition (a,b) have been found to not isomerize, and therefore may react with NO, HO_2, or other RO_2 radicals over the range of chemical conditions in this study. The ring opened peroxy radical (c) has been characterized as quickly isomerizing, though RO_2+NO in experiment 9 (and during initial conditions in experiments 6 and 8) would be competitive. Isomerization rates for the hydrogen abstraction derived peroxy radicals (d,e) have not been experimentally constrained to our knowledge (Capouet et al., 2004; Xu et al., 2019; Berndt, 2021; Salo et al., 2022; Shen et al., 2022).

4.4.2 Dependence of SOA composition on RO_2 chemistry

Figure 4.4 shows EESI mass spectra of SOA formed early in the experiment (10% α-pinene consumed), for three different experiments: a) one at high β (Expt. 2, β=0.21, $\tau_{NO,HO2}$=9.5s), b) one at low β (Expt. 9, β=0.99, $\tau_{NO,HO2}$=0.06s), and c) one at mid-β and high-$\tau_{NO,HO2}$ (Expt. 3, β=0.62, $\tau_{NO,HO2}$=17.3s). Each spectrum is weighted by carbon number and then normalized to the total product signal. The high β experiment takes place in conditions favoring reactions of RO_2 with HO_2. The spectrum in this experiment at this stage is largely dominated by just two particle-phase products, $C_{10}H_{18}O_6$, and $C_{10}H_{18}O_7$. The addition of two hydrogen atoms to the parent molecule ($C_{10}H_{16}$) is key to understanding the RO_2 formation chemistry, which implies the addition of a hydroperoxide or alcohol group to the peroxy radical by reaction with HO_2. Because there are more than the 3 oxygens which would be attached by OH and HO_2 addition, some isomerization step is likely also involved to increase the oxygen numbers of these formulas. One additional possibility is that diols from an RO_2+RO_2 reaction, which would form one alcohol (ROH) and one aldehyde (R=O), could produce $C_{10}H_{18}O_x$ formulas, but the absence of dimerized (ROOR) products at higher molecular weights (m/z~300-450) suggests relatively little RO_2+RO_2 chemistry is occurring under these conditions.

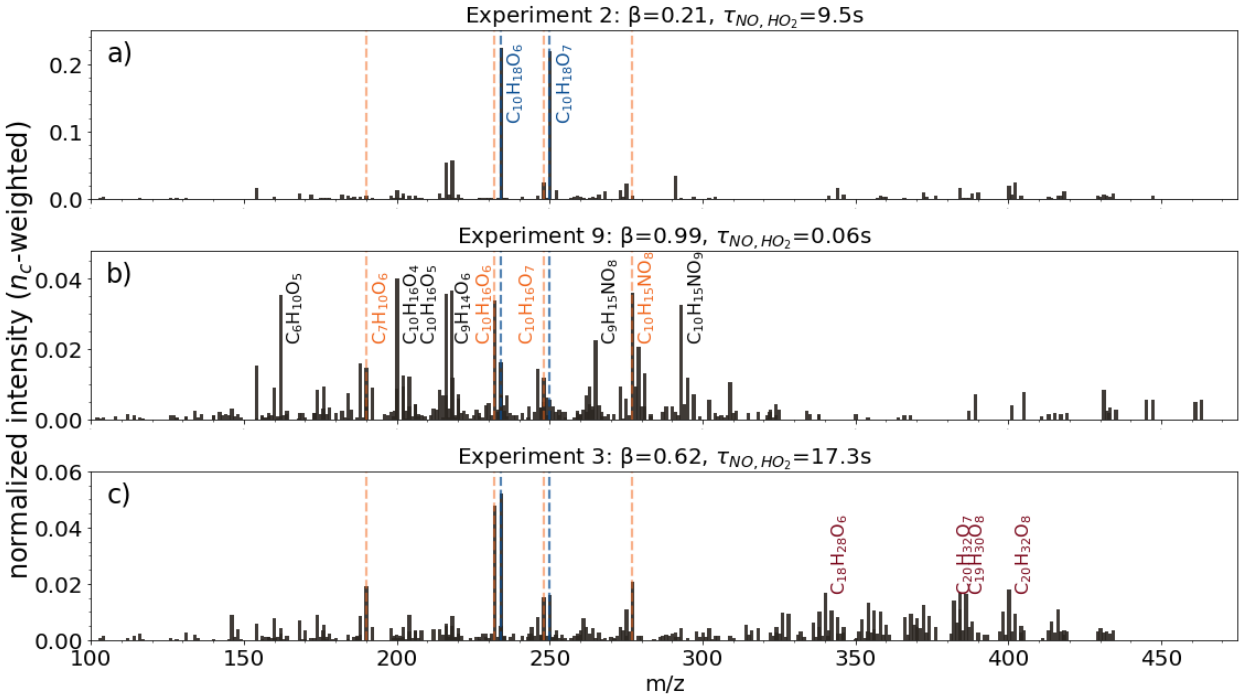

Figure 4.4: Spectra at 10% precursor decay for a) Experiment 2, β=0.21, $\tau_{NO,HO2}$=9.5s, b) Experiment. 9, β=0.99, $\tau_{NO,HO2}$=0.06s, and c) Experiment 3, β=0.62, $\tau_{NO,HO2}$=17.3s. Prominent peaks common to experiments 2 and 3 are marked with blue vertical lines and peaks common to experiments 9 and 3 are marked with orange vertical lines. Signals are the average spectrum during a 10-minute window centered around the time of 10% precursor reaction, weighted by carbon number and then normalized to the total product signal. For simplicity, the sodium ion adduct mass has been removed for every species.

The high β experiment (Figure 4.4b, β=0.99, $\tau_{NO,HO2}$=0.06s) heavily favors RO_2 reaction with NO. The dominance of organic nitrates $C_{10}H_{15}NO_8$, $C_{10}H_{15}NO_9$ and $C_9H_{15}NO_8$ demonstrates the importance of pathways incorporating a nitrate functional group. Non-nitrogen containing products such as $C_6H_{10}O_5$, $C_7H_{10}O_6$, $C_9H_{14}O_6$, and $C_{10}H_{16}O_{4-7}$ are also prominent features of this spectrum. The lower carbon and hydrogen content of the $C_{<10}$ species, resulting from fragmentation, implies chemistry proceeding from alkoxy radical formation, which is most likely to occur from reaction with NO. As discussed earlier, alkoxy radicals may also arise from the RO_2+RO_2 pathway or the HO_2 pathway under certain conditions. There is some signal detected from $C_{10}H_{18}O_{6-7}$ in this experiment, but compared with the low β experiment, it is a much smaller signal. Similarly, there is not much signal detected in the higher mass region, limiting the evidence for RO_2+RO_2 chemistry.

Finally the higher $\tau_{NO,HO2}$ experiment (Figure 4.4c, β=0.62, $\tau_{NO,HO2}$=17.3s) represents a mixed case, with competition between HO_2 and NO, and the longest $\tau_{NO,HO2}$. Higher molecular weight species (m/z~300-450) were prominent in this spectrum compared to the limiting cases: the largest signals observed were $C_{20}H_{32}O_{7-8}$, $C_{19}H_{30}O_8$, and $C_{18}H_{28}O_6$. The dimerized species are a result either of particle-phase oligomerization or gas-phase RO_2+RO_2 chemistry. Additionally, large signals in the early spectra of both the low β ($C_{10}H_{18}O_{6-7}$) and high β ($C_7H_{10}O_6$, $C_{10}H_{16}O_{6-7}$, $C_{10}H_{15}NO_8$) appear as well in this experiment, although the relative ratios of these products are not reproduced, and some prominent products in the high β experiment are absent. All of these differences imply that the chemistry involved in this higher $\tau_{NO,HO2}$ experiment did involve some common RO_2 pathways to the limiting case experiments but also experienced differing chemistry resulting in the formation of dimers.

Figure 4.5 shows a Generalized Kendrick Analysis (GKA) plots for the 3 aforementioned experiments at 10% precursor decay (Alton et al., 2023). Each plot is characterized by 4 regions of products: monomeric compounds with formulas $C_{2-10}H_yO_z$ in the upper left quadrant, nitrates $C_{2-}10H_yNO_z$ in the the lower left, and dimeric compounds $C_{11-20}H_yO_z$ and $C_{11-20}H_yNO_z$ in the upper and lower right quadrants. The differences in mass defect are scaled in a manner that preserves double bond equivalence. In effect, this creates horizontal lines corresponding to different oxygen numbers, i.e. a line of $C_{10}H_{16}O_z$, etc. It is easy to visualize the differences in RO_2 chemistry resulting from fragmentation, dimerization, and incorporation of nitrate groups. For the low β experiment, where RO_2+HO_2 dominates (Figure 4.5a), there are relatively few organic nitrates – about 18% of the carbon weighted instrument signal. Dimer products also make up about 23% of the instrument signal. For the high β, where RO_2+NO is the dominant pathway, organic-nitrate signal represents nearly 40% of the instrument response after the initiation of photochemistry. The monomeric island in the upper left quadrant is lower in mass than in the low β experiment, suggesting more fragmentation. For the longer $\tau_{NO,HO2}$ experiment (Figure 4.5c), the most prominent feature of the spectrum is the high abundance of dimers ($C_{>10}H_yO_z$ and $C_{>10}H_yNO_z$), which account for 51% of the signal.

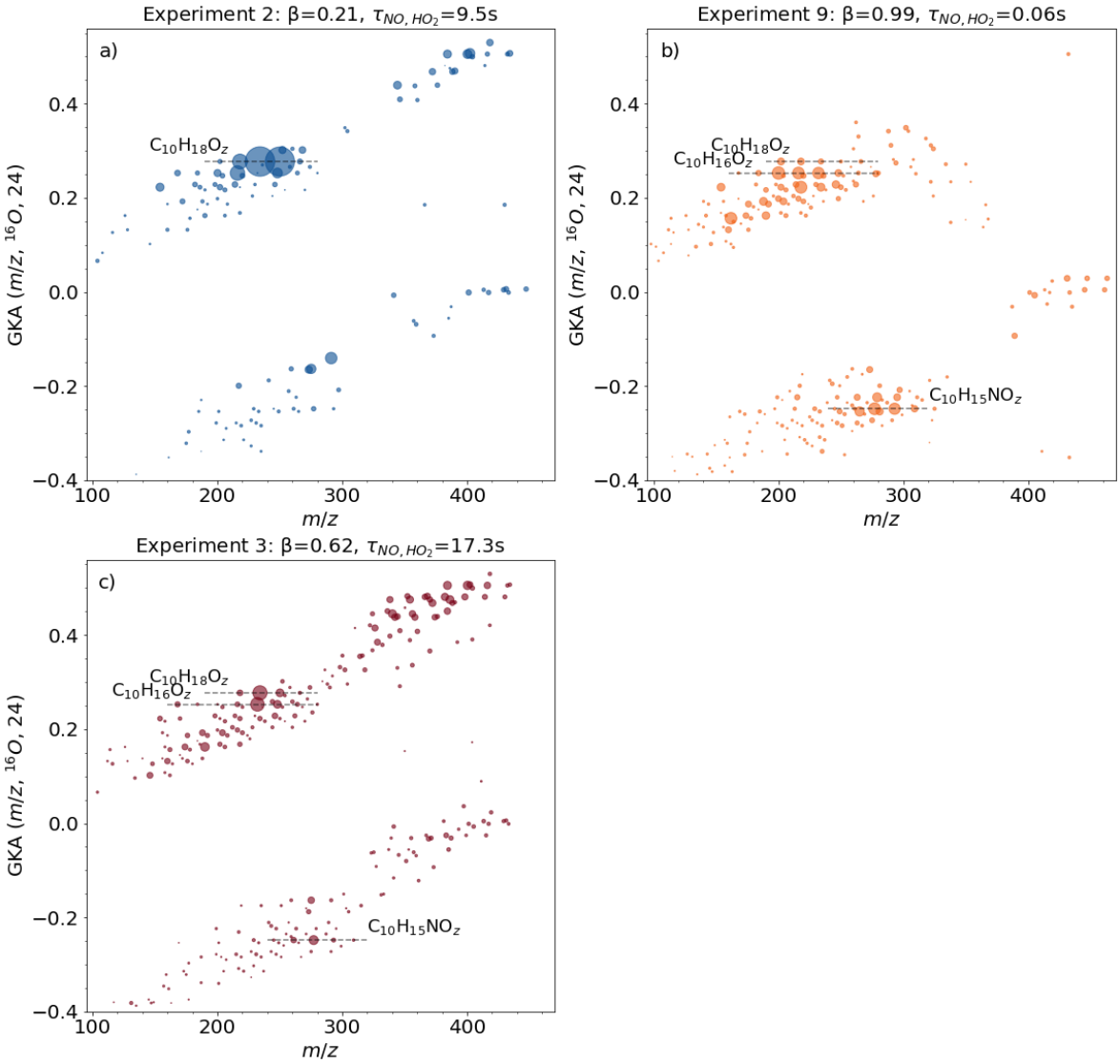

Figure 4.5: Generalized Kendrick Analysis Spectra for a 10% precursor decay for a) Experiment 2, β=0.21, $\tau_{NO,HO2}$=9.5s, b) Experiment. 9, β=0.99, $\tau_{NO,HO2}$=0.06s, and c) Experiment 3, β=0.62, $\tau_{NO,HO2}$=17.3s. Prominent differences in the three spectra include the prominence of $C_{10}H_{18}O_z$ species in experiment 2, the distribution of nitrate species (lower quadrants) in experiment 9, and more dimerized species (right quadrants) in experiment 3.

To investigate the validitiy of using β as a linear parameter to extrapolate the gas-phase chemistry and SOA composition from extreme cases to mixed RO_2 regimes, we construct an intermediate spectrum from our high and low β in linear combination to match the β value estimated in our high $\tau_{NO,HO2}$ experiment. This mimics the approach of parameterizing an intermediate oxidation regime, similar to the approach in treating RO_2 fates commonly used in treatments of gas-phase chemistry in models of the atmosphere. Figure 4.6 displays the difference between this approximated spectrum and the EESI spectrum from the high $\tau_{NO,HO2}$ experiment. Differences between the two spectra indicate that the linear combination diverges from the experimental results. This is easiest to see in the higher mass region corresponding to dimers (m/z ~325-425) where RO_2+RO_2 chemistry is necessary to produce the larger compounds,

but there are also some considerable differences in the monomeric compounds: the approximation predicts more of the hydroperoxides $C_{10}H_{18}O_{6\text{-}8}$ than is measured and also there are mismatches in the $C_{10}H_{16}O_{4\text{-}6}$ peaks – the measured $C_{10}H_{16}O_6$ signal is much greater than predicted by this linear combination of extreme β values.

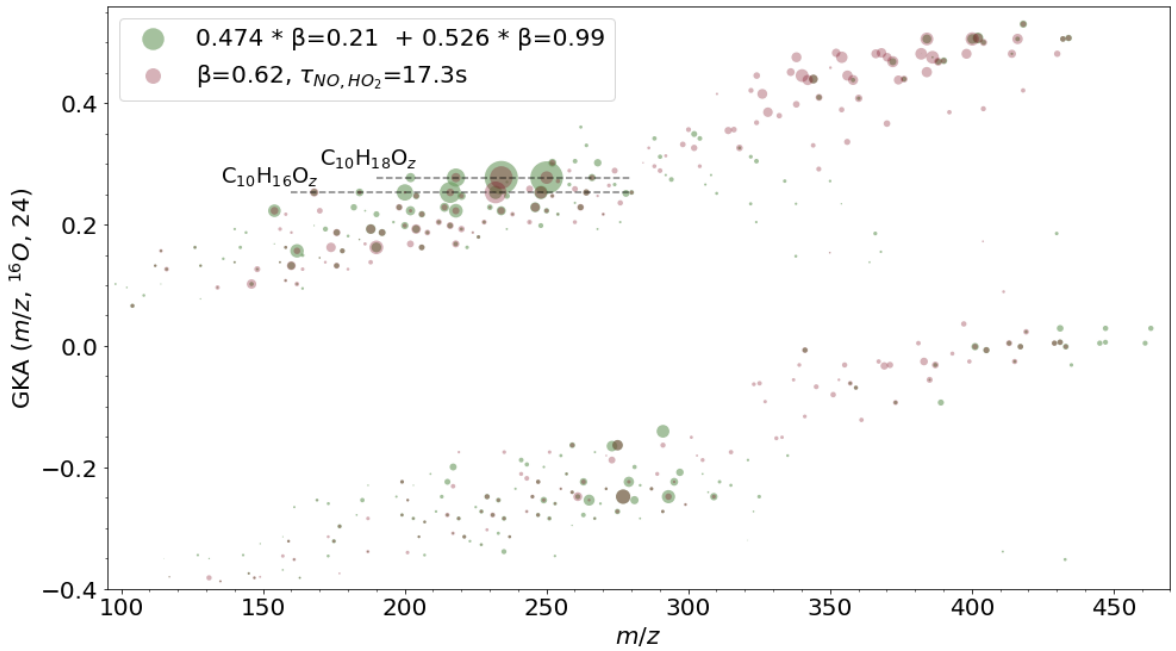

Figure 4.6: GKA plot of Experiment 3, β=0.62, $\tau_{NO,HO2}$=17.3s and linear approximation from high and low β experiments. Differences between the real spectrum and the approximation represent nonlinearities arising in the longer $\tau_{NO,HO2}$ experiment from a mixed RO_2 regime.

We observe similar trends in the relationship between our estimation of RO_2 conditions and the products detected in the other 6 experiments (Figure 4.A.5). The intermediate β experiments contain common formulas to those in the high and low β experiments discussed. Furthermore, the experiments with longer estimations of $\tau_{NO,HO2}$ include higher levels of dimers. The overall composition across experiments will be discussed in a later section.

4.4.3 Evolution of aerosol composition

As each experiment proceeds, the spectra detected in the EESI changes, with new compounds absent during early oxidation conditions growing in. By 60% consumption of the precursor, there are major differences from the spectra shown in Figure 4.4. Figure 4.7 shows the same experiments at 60% loss of α-pinene for the low β (β=0.11, $\tau_{NO,HO2}$=10.6s), higher β (β=0.99, $\tau_{NO,HO2}$=0.29s), and higher $\tau_{NO,HO2}$ (β=0.39, $\tau_{NO,HO2}$=111.0s) experiments (note that values β and $\tau_{NO,HO2}$ have changed as shown in Table 4.1/Figure 4.2). The most prominent peaks in the low β experiment are $C_{10}H_{16}O_{4\text{-}7}$ and $C_{10}H_{18}O_{4\text{-}7}$, along with the standout peak corresponding to a fragmentation product, $C_9H_{14}O_2$. In experiment 3, $C_{10}H_{15}NO_7$ and $C_8H_{12}O_5$, are now the largest peaks, which were not prominent in the spectra detected at 10% precursor loss. Other major signals, ($C_9H_{14}O_6$, $C_{10}H_{16}O_{4\text{-}6}$, and $C_{10}H_{15}NO_{8\text{-}9}$), are common to both spectra. Some shared formulas are present between the high β or low β experiment and the longer $\tau_{NO,HO2}$ (highlights/vertical lines in Figure 4.7b) – but the distribution is dominated by the $C_{10}H_{16}O_6$ peak

out of proportion to either high or low β experiment. The signals of $C_7H_{10}O_{5\text{-}6}$ are higher than either of the limiting experiments. Lastly, the distribution of dimer signals has shifted towards lower masses ($C_{18}H_{28}O_{6\text{-}7}$) than the spectra at 10% precursor loss. This trend towards lower masses/carbon number dimeric compounds over time is consistent with results from α-pinene ozonolysis experiments reported by Pospisilova et al., 2020, which were suggested to be the result of particle-phase accretion reactions and decomposition of the C_{20} compounds. The increase in $\tau_{NO,HO2}$ for experiment 5 (17.3s to 111.0s) did not result in a relative increase in the abundance of dimer signal detected. Though there are still clear differences between all 3 experiments, the spectra are more similar to each other than during initial conditions shown in Figure 4.4. The main exceptions to this are the high organic nitrate signals in the high β experiment, and the $C_7H_{10}O_{5\text{-}6}$ peaks in the higher $\tau_{NO,HO2}$ experiment. Other distinguishing features such as the hydroperoxide and dimer peaks are relatively diminished, suggesting that some of the defining products from specific RO_2 pathways conditions may be removed by other processes over time.

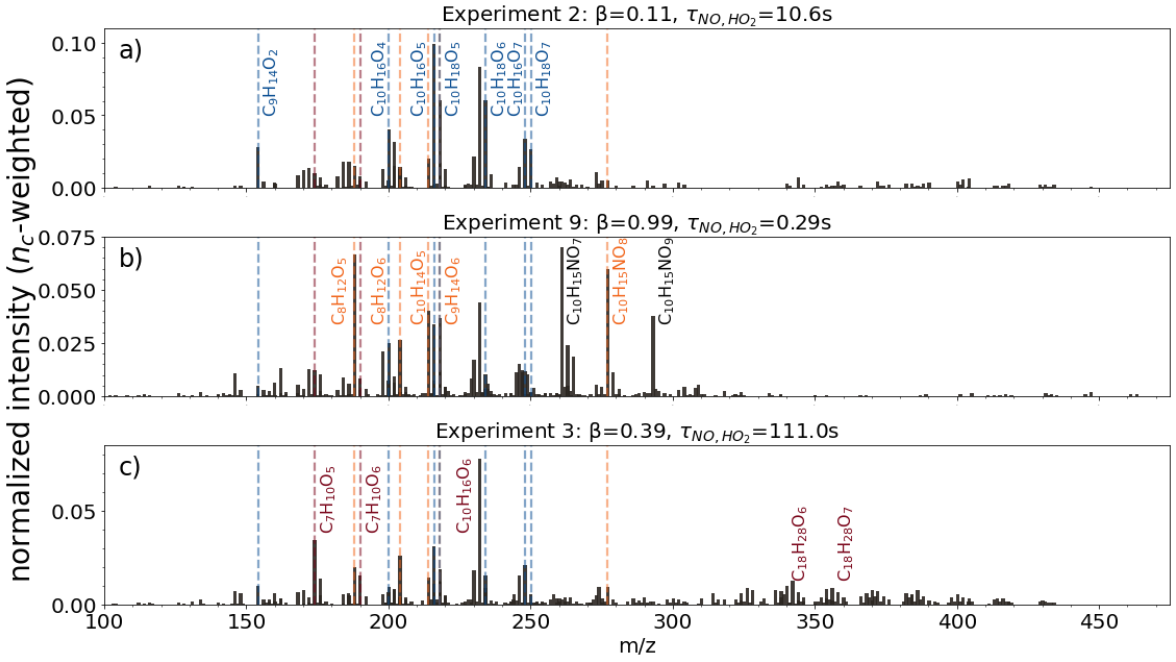

Figure 4.7: Spectra at 60% precursor decay for a a) Experiment 2, β=0.11, $\tau_{NO,HO2}$=10.6s, b) Experiment. 9, β=0.99, $\tau_{NO,HO2}$=0.29s, and c) Experiment 3, β=0.39, $\tau_{NO,HO2}$=111.0s. Prominent peaks common to experiments 2 and 3 are highlighted in blue and peaks common to experiments 9 and 3 are highlighted in orange.

Finally, we examine trends in the key categories of products (nitrates, dimers, and hydroperoxides) in β and $\tau_{NO,HO2}$ for all 9 experiments. Figure 4.8 shows scatterplots of a) organic nitrate ($C_xH_yNO_z$) signal intensity versus β, b) dimer ($C_{>10}H_xN_yO_z$) signal intensity versus $\tau_{NO,HO2}$, and c) hydroperoxide ($C_{10}H_{18}O_z$) signal intensity versus β. The correlation between β and the fraction of organic nitrate signal remains robust (R^2=0.9) at 60% precursor loss. This linearity is preserved despite the evidence of RO_2+RO_2 chemistry in longer tau experiments at intermediate cases. In fact, the correlation improves with further oxidation, perhaps because the fraction of

signal corresponding to dimers decreases with further oxidation, as shown in Fig.8b. The fraction of dimers is positively correlated with $\tau_{NO,HO2,}$ with some relative outliers, such as the second longest $\tau_{NO,HO2}$ experiment. The decrease in the fraction of instrument signal contained in dimeric compounds between 10% and 60% oxidation suggests that these compounds are formed quickly during initial RO_2 conditions and potentially lost to further chemistry, as discussed for Figure 4.7c. Finally, the fraction of hydroperoxide ($C_{10}H_{18}O_z$) species is correlated with lower values of β but does not display a linear relationship in intermediate cases. Besides this, the overall fraction of $C_{10}H_{18}O_z$ signal decreased with successive oxidation, suggesting that this signature of RO_2+HO_2 chemistry may be increasingly hard to distinguish in aged aerosol. Overall, the correlations between the parameters for estimating RO_2 fate correspond to the predicted trends in key classes of SOA products. For organic nitrates, the overall level of nitrate formation appears to validate the assumption that mixed cases of RO_2+HO_2 and RO_2+NO chemistry can be approximated by product yields determined at linear cases. However, for both dimers and peroxides, it looks like further parameterizations may be necessary to describe the range of RO_2 oxidation conditions.

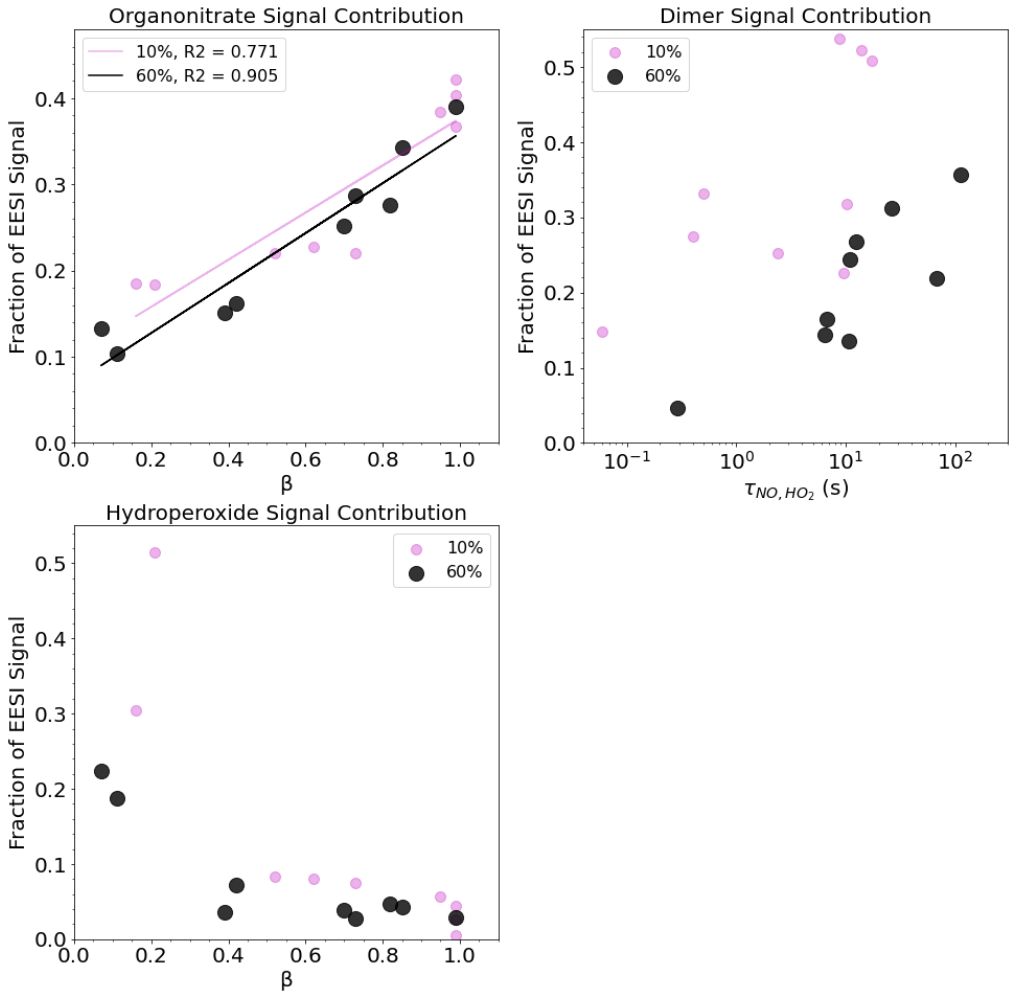

Figure 4.8: Trends in relative fraction of RO_2 pathway dependent product classes versus β and $\tau_{NO,HO2}$. a) Scatterplot of $C_xH_yNO_z$ species (fraction of EESI signal intensity) versus β b) Scatterplot of $C_{>10}H_xN_yO_z$. versus $\tau_{NO,HO2}$ c) Scatterplot of $C_{10}H_{18}O_x$ versus β.

In general, as the spectra evolve with further oxidation, the products detected in all experiments become more similar to one another. Figure 4.9 shows cosine similarities (explain) between all experiments at 10%, 35%, and 60% precursor oxidation. As the extent of oxidation increases, so do the cosine similarities, suggesting increasing convergence of the spectra. Nevertheless, some differences persist between the high and low β conditions, as shown in Figure 4.7. Experiments 2 and 9 only had a cosine similarity of 0.52 at 60% oxidation. The greater importance of β than $\tau_{NO,HO2}$ (correlation in β indicated by coherence of color gradient, see Figure 4.A.8 for arrangement by $\tau_{NO,HO2}$) for differences in correlation might be due to the relatively lower intensity of signal from dimerized compounds at higher masses contributing a small overall portion of the measurement response.

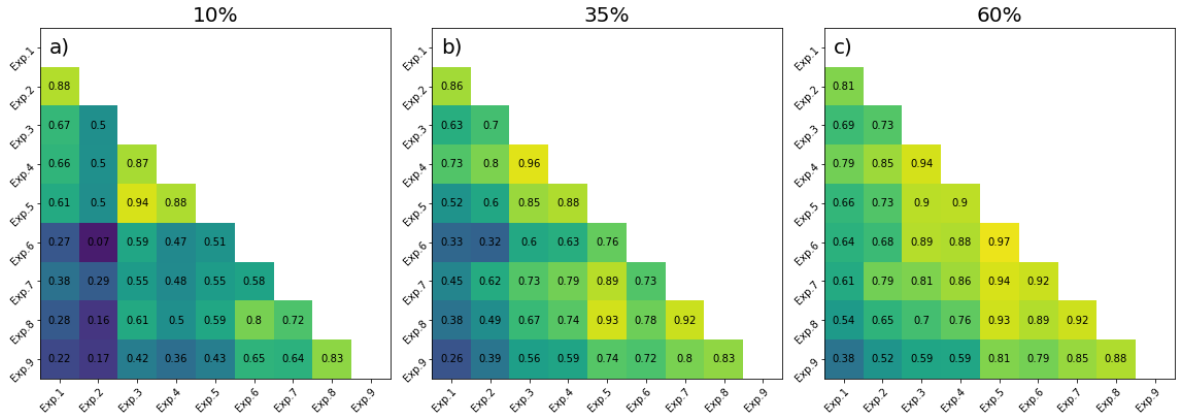

Figure 4.9: Cosine similarity matrix of the experiments in Table 4.1, at a) 10% precursor decay, b) 35% precursor decay, and c) 60% precursory decay. By 60% α-pinene decay, the cosine similarities between experiments are greater, suggesting convergences between the detected spectra in each experiment.

As the SOA products evolve over each experiment, there are multiple processes which may be responsible for the changes observed in both newer species growing in and rapidly formed species decreasing. The first is that the gas-phase oxidation regime, which is reflected in the peroxy radical fates, are changing over the course of a chamber experiment – this is both due to the shifting balance of radicals in the chamber and the relative concentration of peroxy radicals. Changes in the RO_2 regime can then result in different products forming and partitioning to the particle phase. The second possibility that second-generation products start to contribute to the aerosol composition as they are formed and in turn oxidized by OH. Eddingsaas et al., 2012 noted the contribution of oxidation products of pinonaldehyde to SOA in the α-pinene oxidation system, which is reported to from both the RO_2+NO and RO_2+HO_2 pathways. Finally, particle-phase heterogenous or aqueous-phase reactions may be responsible for the formation or decomposition of specific species as the aerosols age. We can assess the likelihood of changes in RO_2 regime influencing the chemical evolution of SOA in the experiments discussed above. As Figure 4.2 shows, there are order of magnitude changes in $\tau_{NO,HO2}$ in some experiments, including in the highest $\tau_{NO,HO2}$ experiment (3). Except for the high β experiment (9), there are also

decreases in β as each experiment progresses. In the high $\tau_{NO,HO2}$ experiment (Fig. 4c,7c), the organonitrate peak corresponding to $C_{10}H_{15}NO_8$ is present early in the experiment (Fig 4c.), when β is higher, but becomes less prominent by 60% oxidation, when β is lower. The difference in relative concentration of the $C_{10}H_{15}NO_8$ signal may therefore be related to the availability of the RO_2+NO pathway decreasing. Overall, the decreases in relative nitrate signal across experiments are also consistent with decreases in β, as shown in Figure 4.8c. On the other hand, the changes in composition occurring in the low β experiment (2) between Figures 4.4a and 4.7a, for instance, do not correspond to a change in $\tau_{NO,HO2}$, and the decrease in β would imply more preferential formation of hydroperoxides relative to conditions at 10% oxidation, which is not observed. Therefore, the changes in the low β composition are presumably not due to changes in RO_2 regime and may be from secondary product oxidation or particle-phase processes. Some combination of these processes is likely responsible for the overall changes in composition which are observed.

The impact of isomerization reactions on the SOA in these experiments is more difficult to determine, since the rates of potential isomerization for some peroxy radicals (Figure 4.3d-e) are currently unconstrained and there are no specific formula types that suggest primary isomerization reaction products to the exclusion of other pathways. Xu et al., 2019 identified a number of products from the ring-opened peroxy radical (Figure 4.3c) which included multiple isomers of an organic nitrate $C_{10}H_{17}NO_6$, a peroxide ketone $C_{10}H_{16}O_3$, and an endoperoxide dialdehyde, $C_{10}H_{16}O_4$. Reaction of the secondary peroxy radical formed from this isomerization pathway could produce a peroxide with the formula $C_{10}H_{18}O_5$, and the combination of two such secondary peroxy radicals could combine to form a dimer with the formula $C_{20}H_{34}O_8$. Products with all of these formulas were detected in the EESI, but without information for distinguishing isomers, it is not possible to ascertain whether these products are formed from the ring-opened peroxy radical versus another pathway, or how efficiently these products will partition into the particle phase. Formulas with 6 or more oxygens are likely to involve either an initial or secondary isomerization step (following generation of an alkoxy radical). These more oxygenated products may only otherwise be formed from secondary generations of oxidation that would proceed at a slower rate. The higher oxygen number species detected in Figure 4.4 at an early stage of oxidation are therefore likely to have resulted from processes involving some isomerization. With only information about formulas of the SOA products, it is not straightforward to describe the mixed influence present of isomerization alongside other peroxy radical pathways.

4.5 Conclusions

We performed a series of α-pinene oxidation experiments with the aim of systematically altering the gas-phase RO_2 fates and monitored the changes in secondary organic aerosol composition in real time with EESI-ToF-MS. This revealed that RO_2 oxidation conditions can have dramatic influences on the products which condense into the particle phase. The formulas of some of the detected products corroborate the expected RO_2 chemistry. While the overall differences in composition between all experiments decreased with oxidation exposure, large differences in the spectra between extremes in β persisted. The overall level of organonitrate signals observed in each experiment correlated with β, and differences in $\tau_{NO,HO2}$ values, especially initial conditions, impacted overall formation of dimer products. The clearest markers of HO_2

chemistry, formulas likely corresponding to hydroperoxides, decreased overall relative to early oxidation conditions. Though further study will be needed to determine the longevity of certain particle-phase compounds, it is possible to identify marker species which could be adapted to identify RO_2 formation chemistry in ambient conditions.

The changes over time in RO_2 conditions within the chamber trend towards longer values of $\tau_{NO,HO2}$ and lower values of β, which is similar to conditions experienced by a plume of air travelling away from a source of NO_x and VOCs. Nevertheless, it will be useful to disentangle changes in RO_2 regime from other processes such as particle-phase reactions for describing the evolution of SOA. This will require targeted studies with more careful control of RO_2 conditions, as well as studies of aerosol aging following formation under differing RO_2 regimes. Isolation and identification of specific isomerization rates for all α-pinene derived peroxy radicals will be crucial for a more precise description of RO_2 fates as a function of $\tau_{NO,HO2}$. In addition to identification of initial RO_2 pathways and rates, a more comprehensive description of RO_2 fate will greatly improve knowledge of key chemical processes. Cross reactions of NO and HO_2, which are more likely to occur in mixed β conditions, may be absent from limiting experiments. Another challenge for connecting the chemical parameters straightforwardly to RO_2 fate is that while $\tau_{NO,HO2}$ may increase as a result of decreasing oxidant concentrations, the overall rates of RO_2+RO_2 reactions may also decrease at the same time, owing to decreased RO_2 concentrations, and therefore not see a relative increase in RO_2 derived products. Finally, assessing the impacts of atmospherically relevant RO_2 composition (arising from other VOCs) and concentrations will better constrain RO_2+RO_2 chemistry.

There are important considerations before using the results of this kind of study to parameterize models of SOA composition across different chemical regimes. The timescales of oxidation examined in these experiments corresponded to a few hours, only a fraction of the modeled SOA lifetime in the atmosphere of 4-6 days (Pai et al., 2020). Therefore the composition reported in this study alone will not be able to characterize the evolution of SOA as further atmospheric aging processes are likely to modify the particle composition. Results from these experiments suggest that classes of compounds such as organic nitrates could be described using a β mixing parameter, which describes the competition of the NO- and HO_2-driven RO_2 pathways in intermediate conditions. The nonlinear features of intermediate-regime experiments require an additional variable to describe the results shown in this study. $\tau_{NO,HO2}$ is one such candidate for a more complete description of RO_2 regimes. However, this parameter leaves the relative rates of other pathways such as isomerization unconstrained. Furthermore, it is likely to introduce overestimations of the rates of precursor-derived RO_2+RO_2 products reported in laboratory studies and omit cross reactions with other non-monoterpene peroxy radicals found in the atmosphere. Ideally, implementation of additional RO_2 pathways in models would draw from a more complete description of RO_2 fates, rather than β and $\tau_{NO,HO2}$ alone.

The particle-phase spectra produced from these experiments demonstrate that with instrumentation capable of resolving particle-phase composition such as the EESI, it is possible to track changes in the composition of secondary organic aerosol as a result of the gas-phase peroxy radical chemistry. To our knowledge, this is the first time techniques such as EESI-ToF-MS have been used to examine the connection between RO_2 chemistry and particle-phase

composition. In real time, the aerosol composition formed reflects differences in the RO_2 regime, and these differences, especially in β values, can persist to the extent of oxidation shown in this experiment. The importance of peroxy radical fates can be shown in some important features of the different spectra, as well as in the nonlinearities between limiting RO_2 cases and experiments with lower ranges of $\tau_{NO,HO2}$. The assumptions about product branching ratios and SOA yields from VOC chemistry which currently parameterize the most commonly used earth system models should be thoroughly tested for applicability in conditions where $\tau_{NO,HO2}$ is higher than in historical laboratory studies. As it is clear that specific RO_2 pathways can be essential to the identity of the species that condense into particles, careful consideration should be given to oxidation conditions under which SOA formation processes are studied.

4.A Appendix

4.A.1 TD-EESI-Signal

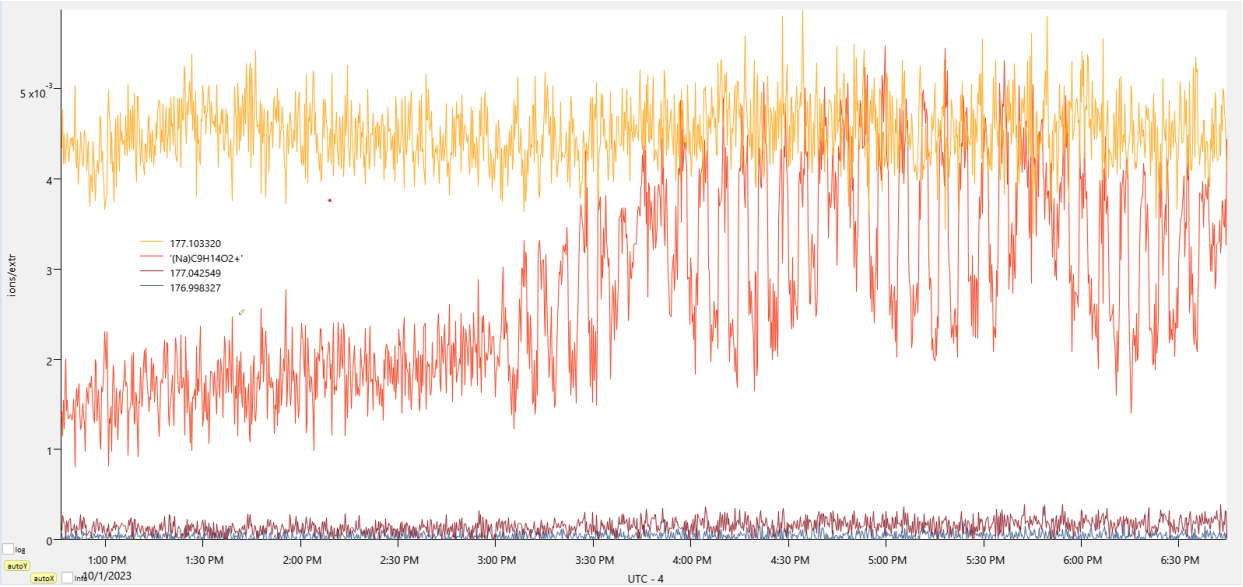

Figure 4.A.1: Timeseries of a product ion (orange) with a background peak at the same unit mass (yellow). The rapid decrease and increase indicates a response to the operation of the thermodenuder – the fluctuation of the lower value on hourly timescales reflects the changing fraction of aerosol lost at different thermodenuder temperatures.

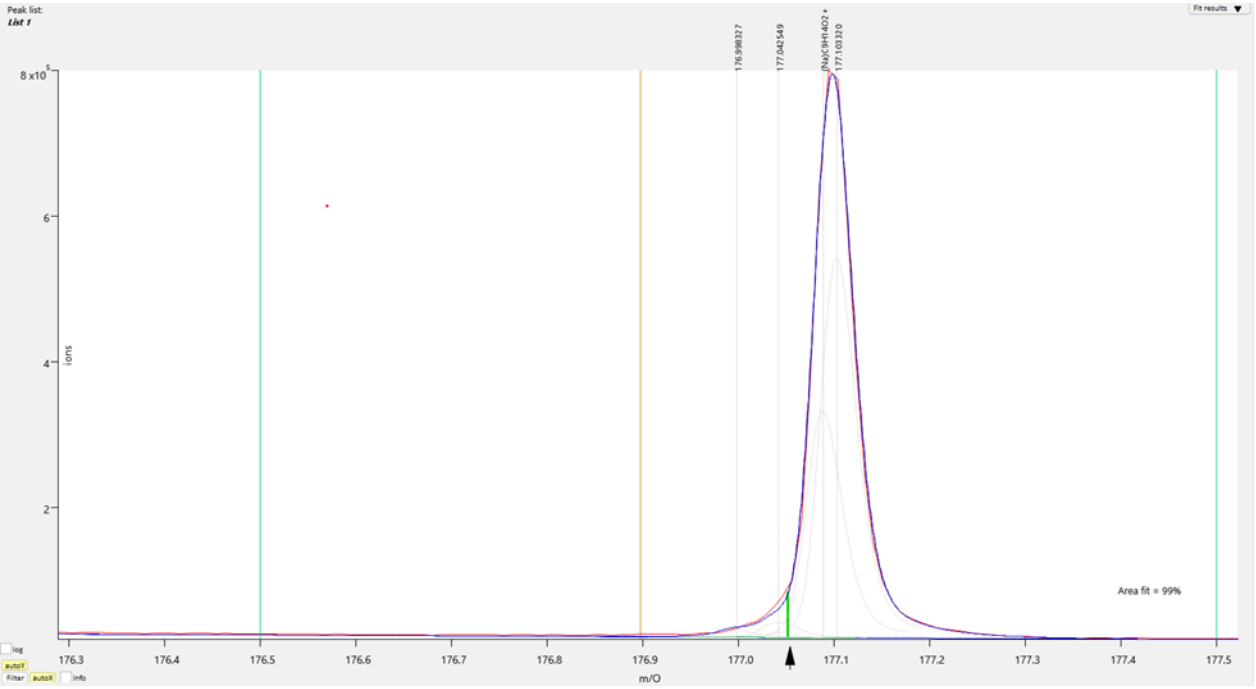

Figure 4.A.2: Peak fit of species shown in Figure 4.A.1. Only the peaks with timeseries reflecting a response to the TD are assigned formulas.

4.A.2. Experiment Modeling

The initial concentration of α-pinene was set to 100ppb for each experiment, and initial concentrations of HONO, NO, and H_2O_2 were modified over multiple orders of magnitude. NO concentrations were varied lognormally in 6 iterations from 10ppt to 1000ppb, HONO concentrations in 20 lognormal iterations from 5ppb to 5000ppb, and H_2O_2 concentrations in 20 lognormal iterations from 5ppb to 50,000ppb.

4.A.3 Precursor Oxidation and SOA Spectra

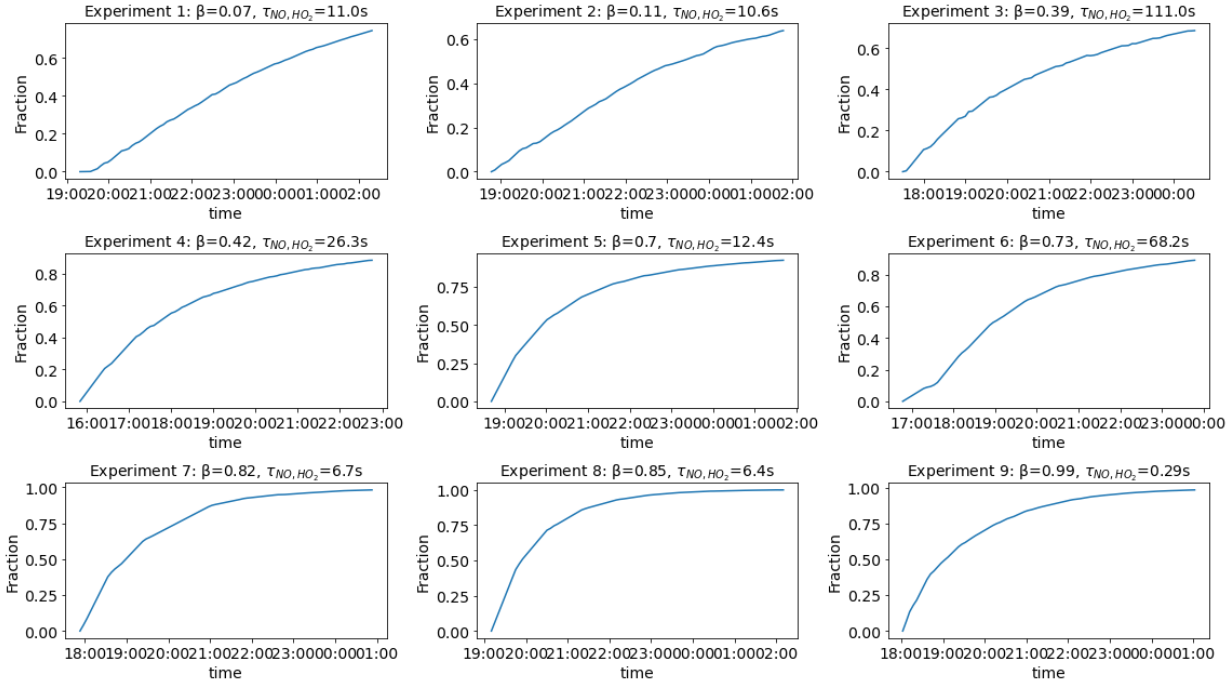

Figure 4.A.3: Fraction of α-pinene decay versus time for each experiment.

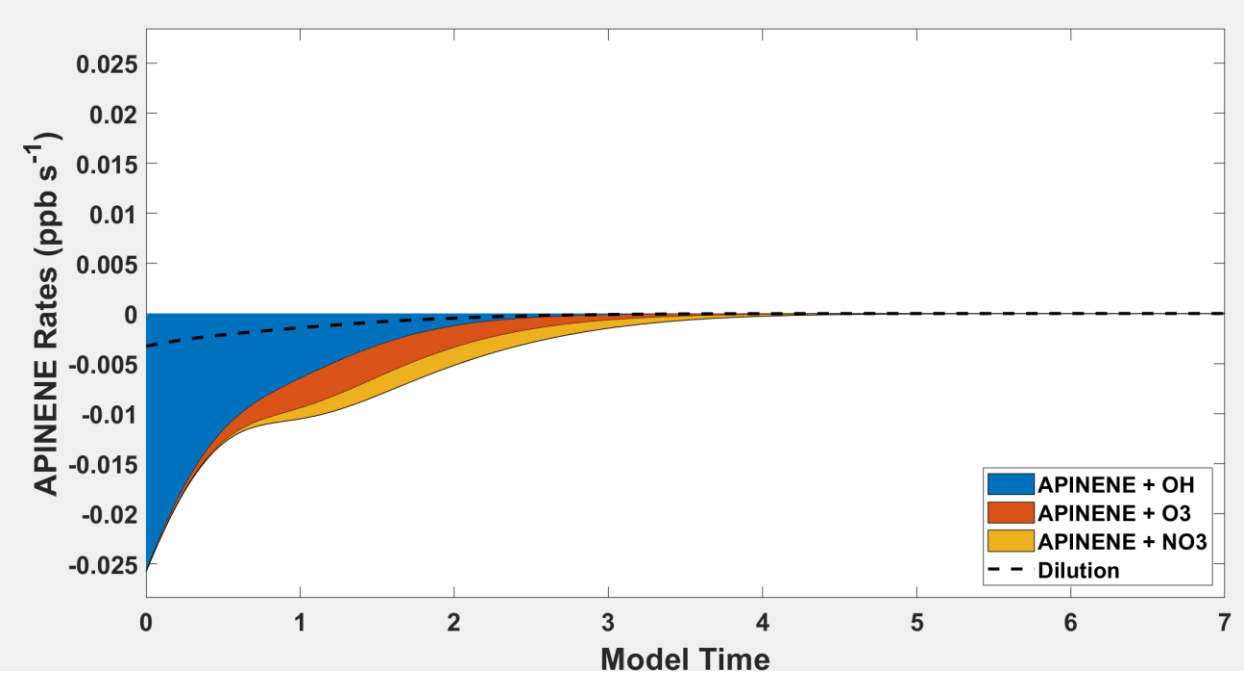

Figure 4.A.4: Example contributions to loss pathways for α-pinene from OH, O_3, and NO_3 in experiment 9 from table 4.1. Early composition is less affected by ozone and nitrate chemical pathways than later oxidation.

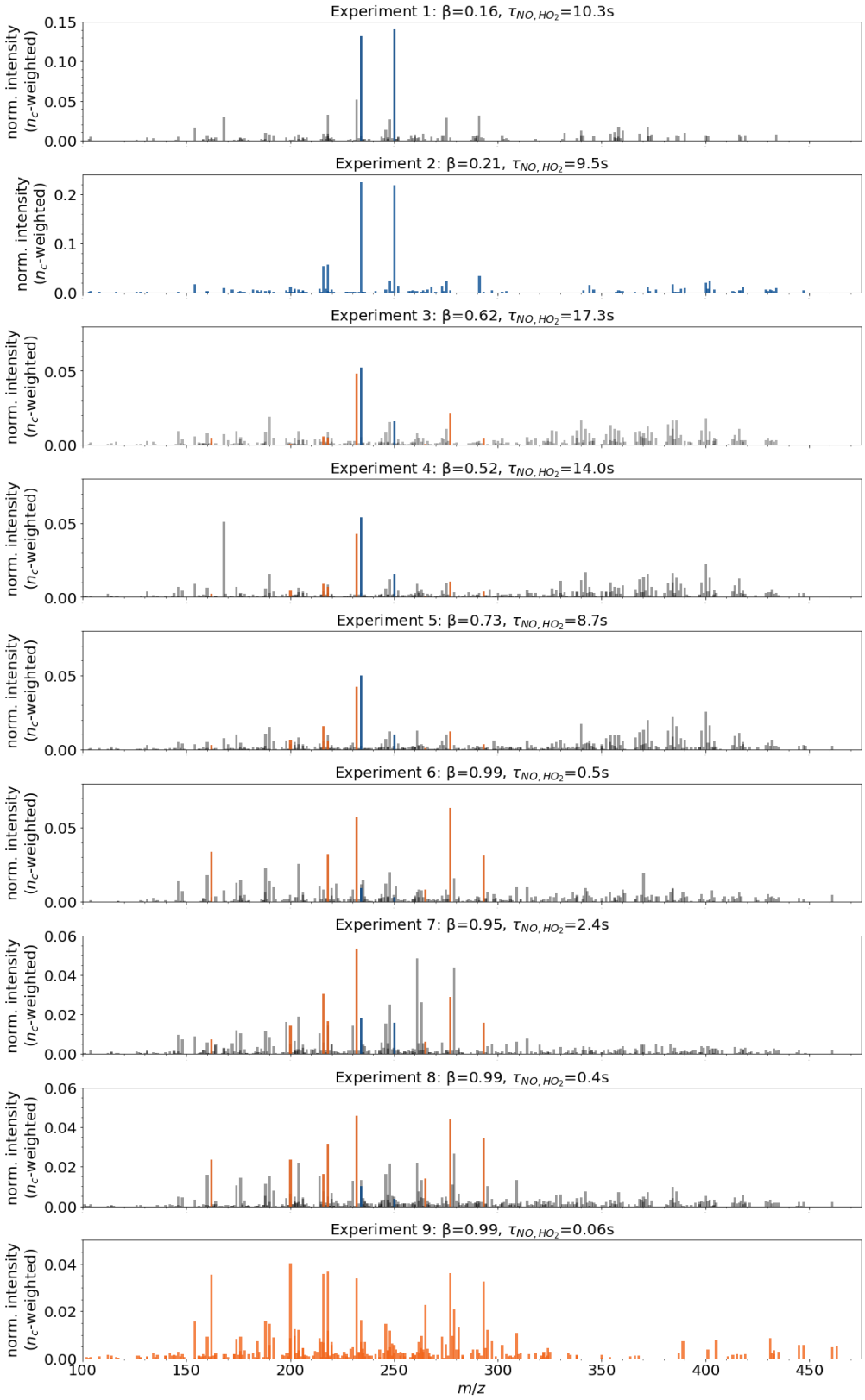

Figure 4.A.5: Spectra of all experiments at 10% precursor loss.

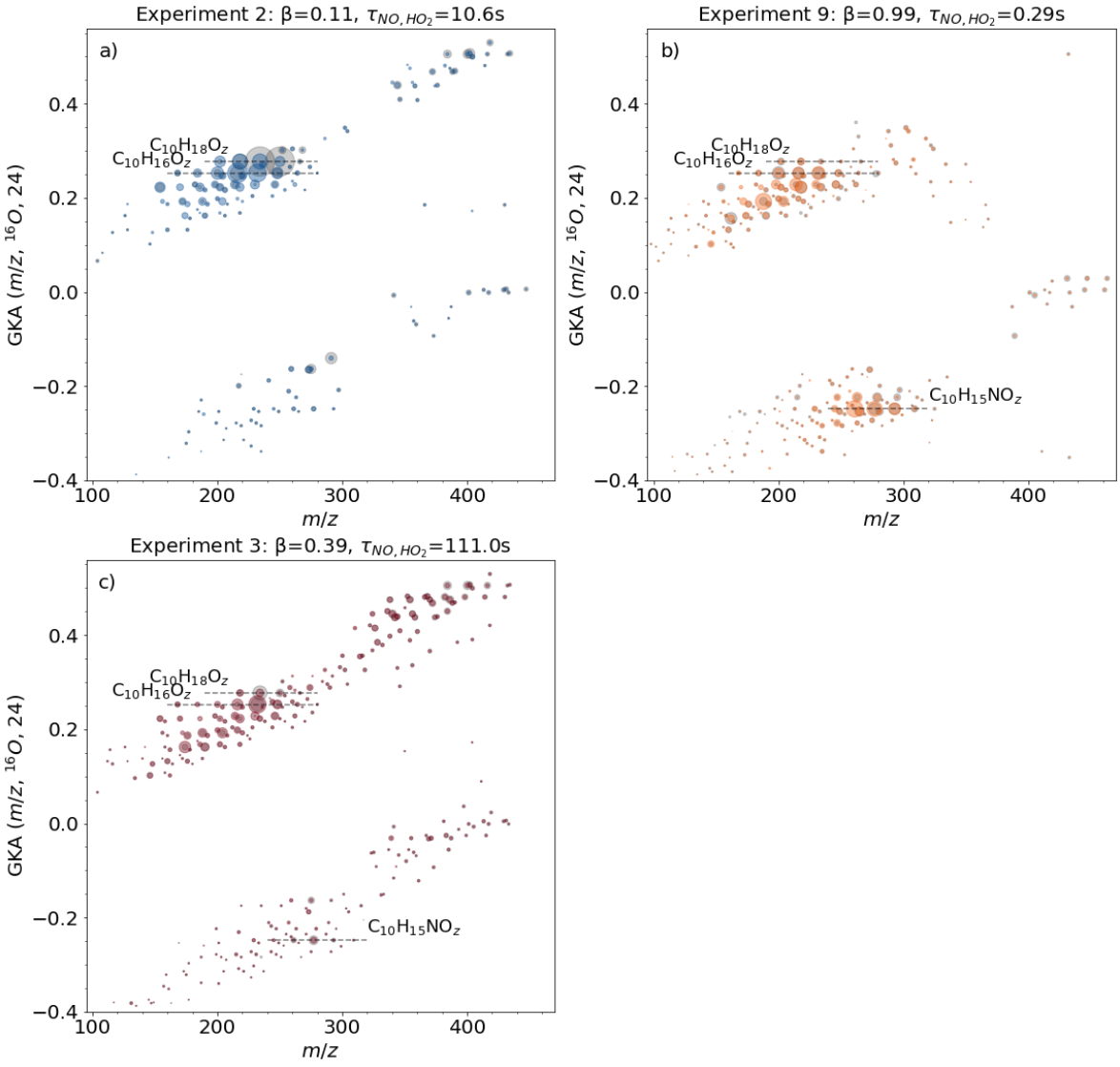

Figure 4.A.6: GKA Spectra for 3 experiments at 60% precursor decay: a) Experiment 2, β=0.11, $\tau_{NO,HO2}$=10.6s, b) Experiment. 9, β=0.99, $\tau_{NO,HO2}$=0.29s, and c) Experiment 3, β=0.39, $\tau_{NO,HO2}$=111.0s. Note chemical parameters have changed relative to 10% precursor decay.

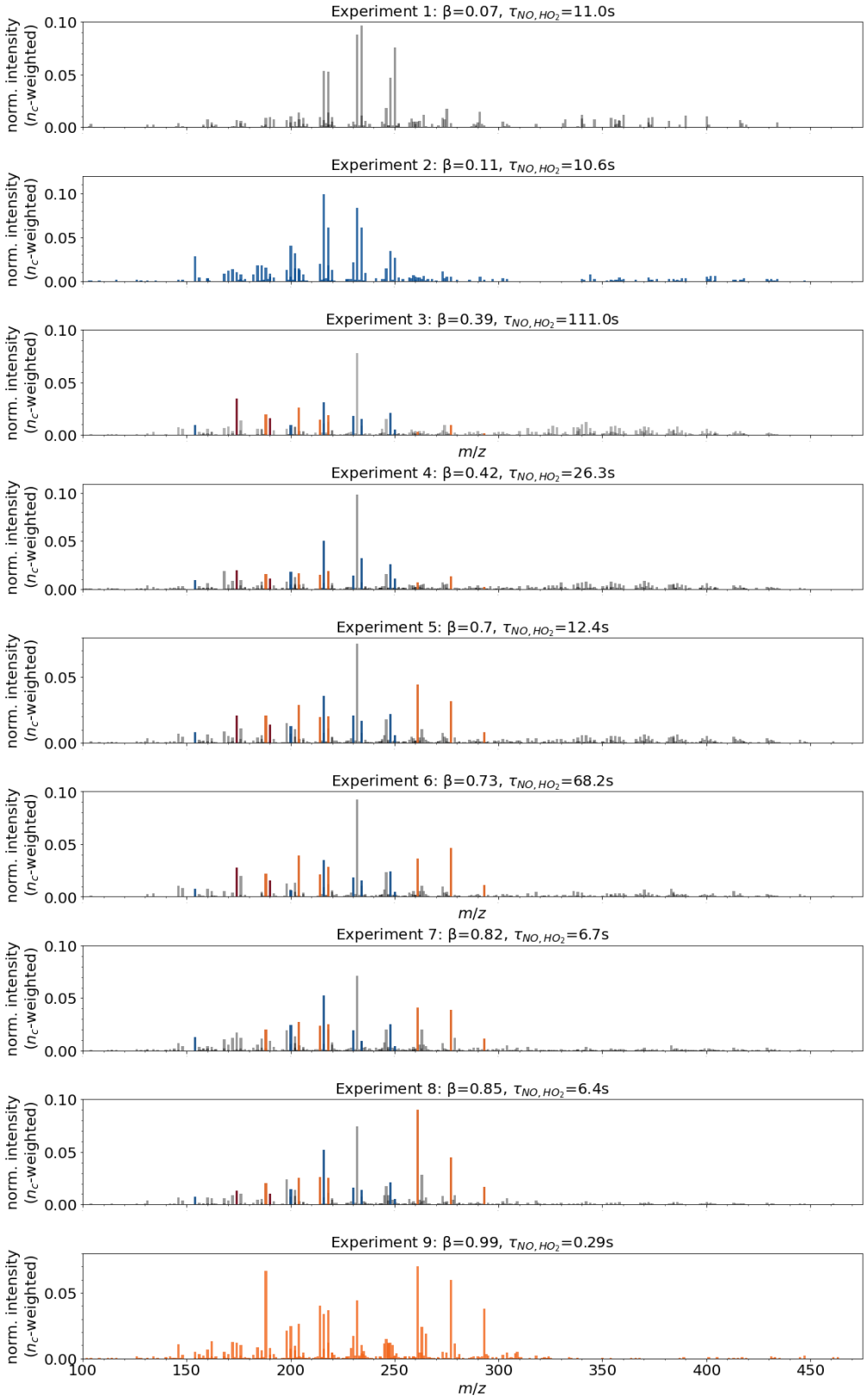

Figure 4.A.7: Spectra of all experiments at 60% precursor loss.

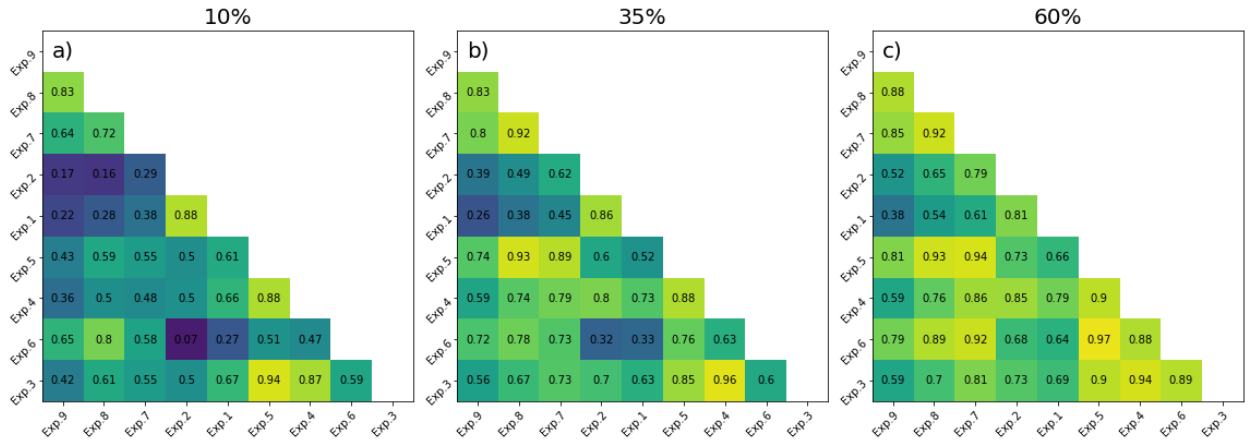

Figure 4.A.8: Cosine similarity matrix of the experiments in Table 4.1, at a)10% precursor decay, b) 35% precursor decay, and c) 60% precursory decay. Experiments are ordered by increasing $\tau_{NO,HO2}$.

Chapter 5: Conclusions and Further Directions

5.1 Main Findings

Advancements in measurement techniques for atmospheric trace constituents have expanded the range of reactive organic carbon which can be detected, both in the gas phase and particle phase, albeit with uncertainties. In this thesis, we adapted these newer measurement techniques to laboratory studies of reactive organic chemistry. We demonstrated improved tools for constraining and investigating VOC oxidation and the composition of SOA.

In Chapter 2, a total suspended carbon measurement technique was adapted for use in laboratory chamber studies. The conversion of all suspended carbon to CO_2 and its detection above reference concentrations enhanced our ability to constrain the overall level of carbon in a chamber experiment. We demonstrated the response of the TOC measurement to a variety of compounds relevant to the ROC system in both the gas and particle phase against a reference instrument. The measurement was able to monitor the overall concentration of a ROC system undergoing chemical transformations and demonstrated the potential to measure secondary CO_2 production, an element of the oxidation system usually overlooked in laboratory experiments. This demonstrates the possibility of applying a top-down constraint on ROC levels in a reliable manner for future chamber experiments aiming to assess carbon closure, as well as the impacts of wall losses.

In Chapter 3, we assessed the ability of different particle-phase measurement techniques to characterize the composition of commonly studied SOA systems. The comparison of three CIMS techniques demonstrated variations in the classes of compounds detected across instruments arising from differences in instrument selectivity. We also provide comparisons to the AMS, a bulk measurement of aerosol composition which mostly fragments the analyzed species. Each of the CIMS techniques demonstrates the potential to better identify chemical functionalization by direct detection of SOA components. However, similarly to assessments of chemical selectivity identified in the gas phase for different CIMS, the relative detection sensitivity of compounds of interest in particle-phase CIMS measurements should be carefully considered when analyzing SOA measurements, as well as the possibility of some fraction of unmeasured products.

In Chapter 4, we applied another new particle-phase measurement technique, extractive electrospray time of flight mass spectrometry (EESI), to monitor the composition of the SOA produced from the gas-phase OH oxidation of α-pinene under different peroxy radical regimes. The experiments demonstrated clearly that the peroxy radical fate can alter the chemical constituents produced. Over time, there are changes in the RO_2 chemical regime as oxidant concentrations change. These differences along with oxidative aging processes in the particle phase contribute to altering the particle composition over time. Though these processes dilute the imprint of differing RO_2 pathways on the SOA products, there are key influences that remain,

especially in the case of species formed from reaction with NO versus reaction with HO_2. The chemical parameters used to characterize the peroxy radical regime correlate with some features of the spectra across experiments, such as the overall level of organic nitrate species. Other nonlinear responses in intermediate regimes highlight the potential importance of RO_2 + RO_2 and isomerization reactions to the composition of SOA.

5.2 Future directions

5.2.1 Carbon Closure/Wall Loss Experiments

The completeness of gas- and particle-phase measurements can be assessed through carbon closure experiments that account for the overall transformation of carbon from a single VOC to various oxidation products. Full carbon closure within measurement error has been achieved in laboratory studies after 6 hours of oxidation, but with a fraction of intermediate carbon species remaining unmeasured or deposited on walls (Isaacman-VanWertz et al., 2018). Wall loss processes in the chamber are one of the challenges to a robust assessment of the overall reactive carbon budget. Although the impact of a delayed instrument response to high loadings of aerosol would complicate analysis of the unmeasured fraction of carbon, adding a particle filter upstream of the catalyst would provide a total gas phase measurement. Combining this with a bulk aerosol measurement such as the AMS would facilitate this real time measurement of all ROC in the chamber. This setup should be used to constrain the extent of wall losses and applied broadly across future chamber experiments alongside speciated instrumentation in order to assess carbon closure and develop depositional corrections to yields of aerosol formation.

5.2.2 Calibrated comparisons of CIMS SOA measurements

The comparison of multiple collocated aerosol CIMS measurements identified clear differences between the types of formulas detected by individual ionization schemes. However, without directly determining the concentrations of specific species, it is difficult to assess the completeness of the measurements performed. It is understood that sensitivity to species by CIMS instruments can vary by orders of magnitude, so the distribution of product signal measured can be easily skewed by compounds whose sensitivities are relatively low or high. There are some possibilities for carrying out calibrations which do not require exhaustive generations of authentic standards. One such technique would involve the use of collision induced dissociation (CID) to determine the relative binding energy of ion-adduct complexes. This can then be related to the binding energy of select species with calibration standards to determine a broad estimation of instrument sensitivity across all species (Zaytsev, Breitenlechner, et al., 2019). By correcting distributions of both gas- and particle-phase species to absolute concentrations, the chemical properties of SOA and the mixture of oxidized ROC can be more accurately assessed, facilitating more accurate analyses of the chemical system.

5.2.3 Future peroxy radical experiments

Further study of the impacts of peroxy radical regimes on composition will need to disentangle the impacts of RO_2 chemistry changes (especially in mixed RO_2 regimes) from other

processes such as particle-phase reactions. Some changes in RO_2 regime are likely unavoidable for experiments run in batch mode, where the relative concentrations of RO_2 available for cross reactions will naturally decrease as a fixed amount of VOC precursor is oxidized. Better techniques for controlling the levels of NO, NO_2, and HO_2 could potentially help stabilize β conditions. This might be accomplished with a continuous or programmed addition of varying levels of oxidant precursors over time, or possibly a feedback program incorporating the real-time measurements of NO_x in the chamber. Steady-state reaction experiments (e.g., as conducted in flow reactors) could also facilitate improved control over RO_2 conditions and isolate potential markers of specific pathways, while suppressing the extent of aging processes. Likewise, more careful study of aerosol aging will be key to determining the viability of particle-phase tracers for RO_2 conditions. Tracer species need to be chemically stable enough to detect downwind of their formation conditions. Isolation of aerosol aging could be accomplished with multi-stage experiments, where the aerosol is first generated and collected in a specific RO_2 regime, and subsequently aged under conditions that simulate the overall levels of oxidation exposure for typical particles in the atmosphere.

In addition to identification of specific RO_2 pathways and rates, a more comprehensive description of RO_2 fate will greatly improve knowledge of key chemical processes. The parameters in chemical space calculated for this study do not account for differences in the fate of subsequent peroxy radical generations, which can form from all of the bimolecular pathways when they produce alkoxy radicals. Cross reactions of NO and HO_2, which are more likely to occur in mixed β conditions, may be absent from limiting experiments. These pathways are another possible contributor to the nonlinear responses observed in intermediate case experiments, rather than from either isomerization reactions, RO_2+RO_2 or RO_2+NO_2 chemistry.

Lastly, large precursor concentrations high bias the rates of RO_2+RO_2 reactions chamber experiments, increasing the formation of dimer products. Concurrently, while smaller peroxy radical species such as alkyl peroxy or isoprene-derived peroxy radicals are common in the atmosphere, these species are absent in single precursor oxidation experiments of monoterpenes. Therefore, the C_{15} compounds from isoprene and monoterpene peroxy radical cross reactions or the C_{11} or C_{13} compounds from reactions with methylperoxy radical or propylperoxy radical are overlooked. The trade-off between isolating α-pinene (or any VOC) oxidation products and assessing more atmospherically relevant RO_2 regimes must be addressed separately by different studies. Furthermore, targeted experiments with synthesized intermediates, and measurement techniques that permit the identification of isomers, would be essential for identifying path dependencies and the robustness of our conclusions about specific aerosol compound tracers of RO_2 chemistry.

All of the speciated measurements for the oxidation products detailed in this thesis are presented as formulas of organic molecules. They lack structural information and calibrations with authentic standards. Calibrations of individual compounds are essential for quantifying the relative abundance of specific products within the overall chemical system. Without better

techniques for quantifying the concentrations of key compounds of interest, such as dimers, organic nitrates, or highly oxidized molecules, the overall importance of these classes of compounds cannot be properly assessed. Furthermore, the lack of structural information prevents identification of specific isomers. In addition to confirming the identity of a given product and facilitating mechanism development, the ability to separate isomers by structural information also matters for proper calibrations whenever multiple isomers vary in sensitivity. The quantification of the components of aerosol particles identified with mass spectrometric techniques will need to be more robustly characterized with advances in instrumentation and methodology. These improvements will allow us to more accurately contextualize studies of SOA chemistry before application to models.

The emissions, oxidation conditions, and fates of ROC need to be more systematically studied. Constraining the potential importance of understudied pathways such as isomerization and multiphase reactions are critical to understanding the fates of these VOCs and their oxidation products in the atmosphere, especially the formation and evolution of SOA. This more complete description of aerosol chemistry will facilitate representation of secondary organic aerosol concentrations in models, which will ideally increase the accuracy of projections of aerosols across scales in future scenarios. Developing the capacity to forecast the impacts of changing emissions and land use will better steer policies which might mitigate the most deleterious impacts of climate- and human-driven changes to atmospheric composition, public health, and ecosystems.

References

Aiken, A. C., DeCarlo, P. F., Kroll, J. H., Worsnop, D. R., Huffman, J. A., Docherty, K. S., Ulbrich, I. M., Mohr, C., Kimmel, J. R., Sueper, D., Sun, Y., Zhang, Q., Trimborn, A., Northway, M., Ziemann, P. J., Canagaratna, M. R., Onasch, T. B., Alfarra, M. R., Prevot, A. S. H., … Jimenez, J. L. (2008). O/C and OM/OC Ratios of Primary, Secondary, and Ambient Organic Aerosols with High-Resolution Time-of-Flight Aerosol Mass Spectrometry. *Environmental Science & Technology*, *42*(12), 4478–4485. https://doi.org/10.1021/es703009q

Aljawhary, D., Lee, A. K. Y., & Abbatt, J. P. D. (2013). High-resolution chemical ionization mass spectrometry (ToF-CIMS): Application to study SOA composition and processing. *Atmospheric Measurement Techniques*, *6*(11), 3211–3224. https://doi.org/10.5194/amt-6-3211-2013

Alton, M. W., Stark, H. J., Canagaratna, M. R., & Browne, E. C. (2023). Generalized Kendrick analysis for improved visualization of atmospheric mass spectral data. *Atmospheric Measurement Techniques*, *16*(12), 3273–3282. https://doi.org/10.5194/amt-16-3273-2023

Anderson, J. G. (1987). Free Radicals in the Earth's Atmosphere: Their Measurement and Interpretation. *Annual Review of Physical Chemistry*, *38*(Volume 38,), 489–520. https://doi.org/10.1146/annurev.pc.38.100187.002421

Atkinson, R. (1986). Kinetics and mechanisms of the gas-phase reactions of the hydroxyl radical with organic compounds under atmospheric conditions. *Chemical Reviews*, *86*(1), 69–201. https://doi.org/10.1021/cr00071a004

Baker, Y., Kang, S., Wang, H., Wu, R., Xu, J., Zanders, A., He, Q., Hohaus, T., Ziehm, T., Geretti, V., Bannan, T. J., O'Meara, S. P., Voliotis, A., Hallquist, M., McFiggans, G., Zorn, S. R., Wahner, A., & Mentel, T. F. (2024). Impact of HO_2/RO_2 ratio on highly oxygenated α-pinene photooxidation products and secondary organic aerosol formation potential. *Atmospheric Chemistry and Physics*, *24*(8), 4789–4807. https://doi.org/10.5194/acp-24-4789-2024

Barber, V. P., & Kroll, J. H. (2021). Chemistry of Functionalized Reactive Organic Intermediates in the Earth's Atmosphere: Impact, Challenges, and Progress. *The Journal of Physical Chemistry A*, *125*(48), 10264–10279. https://doi.org/10.1021/acs.jpca.1c08221

Bates, K. H., Burke, G. J. P., Cope, J. D., & Nguyen, T. B. (2022). Secondary organic aerosol and organic nitrogen yields from the nitrate radical (NO_3) oxidation of alpha-pinene from various RO_2 fates. *Atmospheric Chemistry and Physics*, *22*(2), 1467–1482. https://doi.org/10.5194/acp-22-1467-2022

Berndt, T. (2021). Peroxy Radical Processes and Product Formation in the OH Radical-Initiated Oxidation of α-Pinene for Near-Atmospheric Conditions. *The Journal of Physical Chemistry A*, *125*(41), 9151–9160. https://doi.org/10.1021/acs.jpca.1c05576

Bertram, T. H., Kimmel, J. R., Crisp, T. A., Ryder, O. S., Yatavelli, R. L. N., Thornton, J. A., Cubison, M. J., Gonin, M., & Worsnop, D. R. (2011). A field-deployable, chemical ionization time-of-flight mass spectrometer. *Atmospheric Measurement Techniques*, *4*(7), Article 7. https://doi.org/10.5194/amt-4-1471-2011

Bi, C., & Isaacman-VanWertz, G. (2025). Formation of late-generation atmospheric compounds inhibited by rapid deposition. *Nature Geoscience*, 1–6. https://doi.org/10.1038/s41561-025-01650-2

Bianchi, F., Kurtén, T., Riva, M., Mohr, C., Rissanen, M. P., Roldin, P., Berndt, T., Crounse, J. D., Wennberg, P. O., Mentel, T. F., Wildt, J., Junninen, H., Jokinen, T., Kulmala, M., Worsnop, D. R., Thornton, J. A., Donahue, N., Kjaergaard, H. G., & Ehn, M. (2019). Highly Oxygenated Organic Molecules (HOM) from Gas-Phase Autoxidation Involving Peroxy Radicals: A Key Contributor to Atmospheric Aerosol. *Chemical Reviews*, *119*(6), 3472–3509. https://doi.org/10.1021/acs.chemrev.8b00395

Blake, R. S., Whyte, C., Hughes, C. O., Ellis, A. M., & Monks, P. S. (2004). Demonstration of Proton-Transfer Reaction Time-of-Flight Mass Spectrometry for Real-Time Analysis of Trace Volatile Organic Compounds. *Analytical Chemistry*, *76*(13), 3841–3845. https://doi.org/10.1021/ac0498260

Blake, R. S., Wyche, K. P., Ellis, A. M., & Monks, P. S. (2006). Chemical ionization reaction time-of-flight mass spectrometry: Multi-reagent analysis for determination of trace gas composition. *International Journal of Mass Spectrometry*, *254*(1), 85–93. https://doi.org/10.1016/j.ijms.2006.05.021

Breitenlechner, M., Fischer, L., Hainer, M., Heinritzi, M., Curtius, J., & Hansel, A. (2017). PTR3: An Instrument for Studying the Lifecycle of Reactive Organic Carbon in the Atmosphere. *Analytical Chemistry*, *89*(11), Article 11. https://doi.org/10.1021/acs.analchem.6b05110

Burnett, R. T., Spadaro, J. V., Garcia, G. R., & Pope, C. A. (2022). Designing health impact functions to assess marginal changes in outdoor fine particulate matter. *Environmental Research*, *204*, 112245. https://doi.org/10.1016/j.envres.2021.112245

Cai, M., Ye, C., Yuan, B., Huang, S., Zheng, E., Yang, S., Wang, Z., Lin, Y., Li, T., Hu, W., Chen, W., Song, Q., Li, W., Peng, Y., Liang, B., Sun, Q., Zhao, J., Chen, D., Sun, J., … Shao, M. (2024). Enhanced daytime secondary aerosol formation driven by gas–particle partitioning in downwind urban plumes. *Atmospheric Chemistry and Physics*, *24*(22), 13065–13079. https://doi.org/10.5194/acp-24-13065-2024

Calvo, A. I., Alves, C., Castro, A., Pont, V., Vicente, A. M., & Fraile, R. (2013). Research on aerosol sources and chemical composition: Past, current and emerging issues. *Atmospheric Research*, *120–121*, 1–28. https://doi.org/10.1016/j.atmosres.2012.09.021

Canagaratna, M. R., Jayne, J. t., Jimenez, J. l., Allan, J. d., Alfarra, M. r., Zhang, Q., Onasch, T. b., Drewnick, F., Coe, H., Middlebrook, A., Delia, A., Williams, L. r., Trimborn, A. m., Northway, M. j., DeCarlo, P. f., Kolb, C. e., Davidovits, P., & Worsnop, D. r. (2007). Chemical and microphysical characterization of ambient aerosols with the aerodyne aerosol mass spectrometer. *Mass Spectrometry Reviews*, *26*(2), 185–222. https://doi.org/10.1002/mas.20115

Canagaratna, M. R., Jimenez, J. L., Kroll, J. H., Chen, Q., Kessler, S. H., Massoli, P., Hildebrandt Ruiz, L., Fortner, E., Williams, L. R., Wilson, K. R., Surratt, J. D., Donahue, N. M., Jayne, J. T., & Worsnop, D. R. (2015). Elemental ratio measurements of organic compounds using aerosol mass spectrometry: Characterization, improved calibration, and implications. *Atmospheric Chemistry and Physics*, *15*(1), 253–272. https://doi.org/10.5194/acp-15-253-2015

Capouet, M., & Müller, J.-F. (2006). A group contribution method for estimating the vapour pressures of α-pinene oxidation products. *Atmospheric Chemistry and Physics*, *6*(6), 1455–1467. https://doi.org/10.5194/acp-6-1455-2006

Capouet, M., Peeters, J., Nozi`ere, B., & Müller, J.-F. (2004). Alpha-pinene oxidation by OH: Simulations of laboratory experiments. *Atmospheric Chemistry and Physics*, *4*(9/10), 2285–2311. https://doi.org/10.5194/acp-4-2285-2004

Chan, A. W. H., Kautzman, K. E., Chhabra, P. S., Surratt, J. D., Chan, M. N., Crounse, J. D., Kürten, A., Wennberg, P. O., Flagan, R. C., & Seinfeld, J. H. (2009). Secondary organic aerosol formation from photooxidation of naphthalene and alkylnaphthalenes: Implications for oxidation of intermediate volatility organic compounds (IVOCs). *Atmospheric Chemistry and Physics*, *9*(9), 3049–3060. https://doi.org/10.5194/acp-9-3049-2009

Charlson, R. J., Langner, J., & Rodhe, H. (1990). Sulphate aerosol and climate. *Nature*, *348*(6296), 22–22. https://doi.org/10.1038/348022a0

Chen, W., Hu, W., Tao, Z., Cai, Y., Cai, M., Zhu, M., Ye, Y., Zhou, H., Jiang, H., Li, J., Song, W., Zhou, J., Huang, S., Yuan, B., Shao, M., Feng, Q., Li, Y., Isaacman-VanWertz, G., Stark, H., … Wang, X. (2024). Quantitative Characterization of the Volatility Distribution of Organic Aerosols in a Polluted Urban Area: Intercomparison Between Thermodenuder and Molecular Measurements. *Journal of Geophysical Research: Atmospheres*, *129*(4), e2023JD040284. https://doi.org/10.1029/2023JD040284

Chow, J. C. (1995). Measurement Methods to Determine Compliance with Ambient Air Quality Standards for Suspended Particles. *Journal of the Air & Waste Management Association*, *45*(5), 320–382. https://doi.org/10.1080/10473289.1995.10467369

Crounse, J. D., Nielsen, L. B., Jørgensen, S., Kjaergaard, H. G., & Wennberg, P. O. (2013). Autoxidation of Organic Compounds in the Atmosphere. *The Journal of Physical Chemistry Letters*, *4*(20), 3513–3520. https://doi.org/10.1021/jz4019207

D'Ambro, E. L., Lee, B. H., Liu, J., Shilling, J. E., Gaston, C. J., Lopez-Hilfiker, F. D., Schobesberger, S., Zaveri, R. A., Mohr, C., Lutz, A., Zhang, Z., Gold, A., Surratt, J. D., Rivera-Rios, J. C., Keutsch, F. N., & Thornton, J. A. (2017). Molecular composition and volatility of isoprene photochemical oxidation secondary organic aerosol under low- and high-NO_x conditions. *Atmospheric Chemistry and Physics*, *17*(1), 159–174. https://doi.org/10.5194/acp-17-159-2017

Day, D. A., Fry, J. L., Kang, H. G., Krechmer, J. E., Ayres, B. R., Keehan, N. I., Thompson, S. L., Hu, W., Campuzano-Jost, P., Schroder, J. C., Stark, H., DeVault, M. P., Ziemann, P. J., Zarzana, K. J., Wild, R. J., Dubè, W. P., Brown, S. S., & Jimenez, J. L. (2022). Secondary Organic Aerosol Mass Yields from NO3 Oxidation of α-Pinene and Δ-Carene: Effect of RO2 Radical Fate. *The Journal of Physical Chemistry A*, *126*(40), 7309–7330. https://doi.org/10.1021/acs.jpca.2c04419

De Gouw, J., & Jimenez, J. L. (2009). Organic Aerosols in the Earth's Atmosphere. *Environmental Science & Technology*, *43*(20), 7614–7618. https://doi.org/10.1021/es9006004

DeCarlo, P. F., Kimmel, J. R., Trimborn, A., Northway, M. J., Jayne, J. T., Aiken, A. C., Gonin, M., Fuhrer, K., Horvath, T., Docherty, K. S., Worsnop, D. R., & Jimenez, J. L. (2006). Field-Deployable, High-Resolution, Time-of-Flight Aerosol Mass Spectrometer. *Analytical Chemistry*, *78*(24), Article 24. https://doi.org/10.1021/ac061249n

Dobracki, A., Lewis, E. R., Sedlacek III, A. J., Tatro, T., Zawadowicz, M. A., & Zuidema, P. (2025). Burning conditions and transportation pathways determine biomass-burning aerosol properties in the Ascension Island marine boundary layer. *Atmospheric Chemistry and Physics*, *25*(4), 2333–2363. https://doi.org/10.5194/acp-25-2333-2025

Eddingsaas, N. C., Loza, C. L., Yee, L. D., Chan, M., Schilling, K. A., Chhabra, P. S., Seinfeld, J. H., & Wennberg, P. O. (2012). α-pinene photooxidation under controlled chemical conditions – Part 2: SOA yield and composition in low- and high-NO_x environments. *Atmospheric Chemistry and Physics*, *12*(16), 7413–7427. https://doi.org/10.5194/acp-12-7413-2012

Ehn, M., Kleist, E., Junninen, H., Petäjä, T., Lönn, G., Schobesberger, S., Dal Maso, M., Trimborn, A., Kulmala, M., Worsnop, D. R., Wahner, A., Wildt, J., & Mentel, T. F. (2012). Gas phase formation of extremely oxidized pinene reaction products in chamber and ambient air. *Atmospheric Chemistry and Physics*, *12*(11), 5113–5127. https://doi.org/10.5194/acp-12-5113-2012

Ehn, M., Thornton, J. A., Kleist, E., Sipilä, M., Junninen, H., Pullinen, I., Springer, M., Rubach, F., Tillmann, R., Lee, B., Lopez-Hilfiker, F., Andres, S., Acir, I.-H., Rissanen, M., Jokinen, T., Schobesberger, S., Kangasluoma, J., Kontkanen, J., Nieminen, T., … Mentel, T. F. (2014). A large source of low-volatility secondary organic aerosol. *Nature*, *506*(7489), 476–479. https://doi.org/10.1038/nature13032

Eichler, P., Müller, M., D'Anna, B., & Wisthaler, A. (2015). A novel inlet system for online chemical analysis of semi-volatile submicron particulate matter. *Atmospheric Measurement Techniques*, *8*(3), 1353–1360. https://doi.org/10.5194/amt-8-1353-2015

Fishman, J., Ramanathan, V., Crutzen, P. J., & Liu, S. C. (1979). Tropospheric ozone and climate. *Nature*, *282*(5741), 818–820. https://doi.org/10.1038/282818a0

Furlani, T. C., Ye, R., Stewart, J., Crilley, L. R., Edwards, P. M., Kahan, T. F., & Young, C. J. (2023). Development and validation of a new in situ technique to measure total gaseous chlorine in air. *Atmospheric Measurement Techniques*, *16*(1), 181–193. https://doi.org/10.5194/amt-16-181-2023

Gkatzelis, G. I., Tillmann, R., Hohaus, T., Müller, M., Eichler, P., Xu, K.-M., Schlag, P., Schmitt, S. H., Wegener, R., Kaminski, M., Holzinger, R., Wisthaler, A., & Kiendler-Scharr, A. (2018). Comparison of three aerosol chemical characterization techniques utilizing PTR-ToF-MS: A study on freshly formed and aged biogenic SOA. *Atmospheric Measurement Techniques*, *11*(3), 1481–1500. https://doi.org/10.5194/amt-11-1481-2018

Goldstein, A. H., & Galbally, I. E. (2007). Known and Unexplored Organic Constituents in the Earth's Atmosphere. *Environmental Science & Technology*, *41*(5), Article 5. https://doi.org/10.1021/es072476p

Haagen-Smit, A. J. (1952). Chemistry and Physiology of Los Angeles Smog. *Industrial & Engineering Chemistry*, *44*(6), 1342–1346. https://doi.org/10.1021/ie50510a045

Hasson, A. S., Tyndall, G. S., & Orlando, J. J. (2004). A Product Yield Study of the Reaction of HO2 Radicals with Ethyl Peroxy (C2H5O2), Acetyl Peroxy (CH3C(O)O2), and Acetonyl Peroxy (CH3C(O)CH2O2) Radicals. *The Journal of Physical Chemistry A*, *108*(28), 5979–5989. https://doi.org/10.1021/jp048873t

Hayden, K. L., Li, S.-M., Liggio, J., Wheeler, M. J., Wentzell, J. J. B., Leithead, A., Brickell, P., Mittermeier, R. L., Oldham, Z., Mihele, C. M., Staebler, R. M., Moussa, S. G., Darlington,

A., Wolde, M., Thompson, D., Chen, J., Griffin, D., Eckert, E., Ditto, J. C., … Gentner, D. R. (2022). Reconciling the total carbon budget for boreal forest wildfire emissions using airborne observations. *Atmospheric Chemistry and Physics*, *22*(18), 12493–12523. https://doi.org/10.5194/acp-22-12493-2022

He, L., Liu, W., Li, Y., Wang, J., Kuwata, M., & Liu, Y. (2024). Wall loss of semi-volatile organic compounds in a Teflon bag chamber for the temperature range of 262–298 K: Mechanistic insight on temperature dependence. *Atmospheric Measurement Techniques*, *17*(2), 755–764. https://doi.org/10.5194/amt-17-755-2024

He, M., Ditto, J. C., Gardner, L., Machesky, J., Hass-Mitchell, T. N., Chen, C., Khare, P., Sahin, B., Fortner, J. D., Plata, D. L., Drollette, B. D., Hayden, K. L., Wentzell, J. J. B., Mittermeier, R. L., Leithead, A., Lee, P., Darlington, A., Wren, S. N., Zhang, J., … Gentner, D. R. (2024). Total organic carbon measurements reveal major gaps in petrochemical emissions reporting. *Science*, *383*(6681), 426–432. https://doi.org/10.1126/science.adj6233

Heald, C. L., Goldstein, A. H., Allan, J. D., Aiken, A. C., Apel, E., Atlas, E. L., Baker, A. K., Bates, T. S., Beyersdorf, A. J., Blake, D. R., Campos, T., Coe, H., Crounse, J. D., DeCarlo, P. F., de Gouw, J. A., Dunlea, E. J., Flocke, F. M., Fried, A., Goldan, P., … Zheng, W. (2008). Total observed organic carbon (TOOC) in the atmosphere: A synthesis of North American observations. *Atmospheric Chemistry and Physics*, *8*(7), 2007–2025. https://doi.org/10.5194/acp-8-2007-2008

Heald, C. L., & Kroll, J. H. (2020). The fuel of atmospheric chemistry: Toward a complete description of reactive organic carbon. *Science Advances*, *6*(6), Article 6. https://doi.org/10.1126/sciadv.aay8967

Hellén, H., Dommen, J., Metzger, A., Gascho, A., Duplissy, J., Tritscher, T., Prevot, A. S. H., & Baltensperger, U. (2008). Using Proton Transfer Reaction Mass Spectrometry for Online Analysis of Secondary Organic Aerosols. *Environmental Science & Technology*, *42*(19), Article 19. https://doi.org/10.1021/es801279m

Henze, D. K., Seinfeld, J. H., Ng, N. L., Kroll, J. H., Fu, T.-M., Jacob, D. J., & Heald, C. L. (2008). Global modeling of secondary organic aerosol formation from aromatic hydrocarbons: High- vs. low-yield pathways. *Atmospheric Chemistry and Physics*, *8*(9), 2405–2420. https://doi.org/10.5194/acp-8-2405-2008

Holzinger, R., Williams, J., Herrmann, F., Lelieveld, J., Donahue, N. M., & Röckmann, T. (2010). Aerosol analysis using a Thermal-Desorption Proton-Transfer-Reaction Mass Spectrometer (TD-PTR-MS): A new approach to study processing of organic aerosols. *Atmospheric Chemistry and Physics*, *10*(5), 2257–2267. https://doi.org/10.5194/acp-10-2257-2010

Huang, W., Saathoff, H., Shen, X., Ramisetty, R., Leisner, T., & Mohr, C. (2019). Chemical Characterization of Highly Functionalized Organonitrates Contributing to Night-Time Organic Aerosol Mass Loadings and Particle Growth. *Environmental Science & Technology*, *53*(3), 1165–1174. https://doi.org/10.1021/acs.est.8b05826

Huang, Y., Kenseth, C. M., Dalleska, N. F., & Seinfeld, J. H. (2020). Coupling Filter-Based Thermal Desorption Chemical Ionization Mass Spectrometry with Liquid Chromatography/Electrospray Ionization Mass Spectrometry for Molecular Analysis of Secondary Organic Aerosol. *Environmental Science & Technology*, *54*(20), 13238–13248. https://doi.org/10.1021/acs.est.0c01779

Huey, L. G., Hanson, D. R., & Howard, C. J. (1995). Reactions of SF6- and I- with Atmospheric Trace Gases. *The Journal of Physical Chemistry*, *99*(14), 5001–5008. https://doi.org/10.1021/j100014a021

Huffman, J. A., Ziemann ,Paul J., Jayne ,John T., Worsnop ,Douglas R., & and Jimenez, J. L. (2008). Development and Characterization of a Fast-Stepping/Scanning Thermodenuder for Chemically-Resolved Aerosol Volatility Measurements. *Aerosol Science and Technology*, *42*(5), 395–407. https://doi.org/10.1080/02786820802104981

Hunter, J. F., Carrasquillo, A. J., Daumit, K. E., & Kroll, J. H. (2014). Secondary Organic Aerosol Formation from Acyclic, Monocyclic, and Polycyclic Alkanes. *Environmental Science & Technology*, *48*(17), 10227–10234. https://doi.org/10.1021/es502674s

Hunter, J. F., Day, D. A., Palm, B. B., Yatavelli, R. L. N., Chan, A. W. H., Kaser, L., Cappellin, L., Hayes, P. L., Cross, E. S., Carrasquillo, A. J., Campuzano-Jost, P., Stark, H., Zhao, Y., Hohaus, T., Smith, J. N., Hansel, A., Karl, T., Goldstein, A. H., Guenther, A., … Kroll, J. H. (2017). Comprehensive characterization of atmospheric organic carbon at a forested site. *Nature Geoscience*, *10*(10), Article 10. https://doi.org/10.1038/ngeo3018

Intergovernmental Panel On Climate Change (IPCC). (2023). *Climate Change 2021 – The Physical Science Basis: Working Group I Contribution to the Sixth Assessment Report of the Intergovernmental Panel on Climate Change* (1st ed.). Cambridge University Press. https://doi.org/10.1017/9781009157896

Isaacman-VanWertz, G., Massoli, P., O'Brien, R. E., Nowak, J. B., Canagaratna, M. R., Jayne, J. T., Worsnop, D. R., Su, L., Knopf, D. A., Misztal, P. K., Arata, C., Goldstein, A. H., & Kroll, J. H. (2017). Using advanced mass spectrometry techniques to fully characterize atmospheric organic carbon: Current capabilities and remaining gaps. *Faraday Discussions*, *200*(0), Article 0. https://doi.org/10.1039/C7FD00021A

Isaacman-VanWertz, G., Massoli, P., O'Brien, R., Lim, C., Franklin, J. P., Moss, J. A., Hunter, J. F., Nowak, J. B., Canagaratna, M. R., Misztal, P. K., Arata, C., Roscioli, J. R., Herndon, S. T., Onasch, T. B., Lambe, A. T., Jayne, J. T., Su, L., Knopf, D. A., Goldstein, A. H., … Kroll, J. H. (2018). Chemical evolution of atmospheric organic carbon over multiple generations of oxidation. *Nature Chemistry*, *10*(4), 462–468. https://doi.org/10.1038/s41557-018-0002-2

Jimenez, J. L., Jayne, J. T., Shi, Q., Kolb, C. E., Worsnop, D. R., Yourshaw, I., Seinfeld, J. H., Flagan, R. C., Zhang, X., Smith, K. A., Morris, J. W., & Davidovits, P. (2003). Ambient aerosol sampling using the Aerodyne Aerosol Mass Spectrometer. *Journal of Geophysical Research: Atmospheres*, *108*(D7). https://doi.org/10.1029/2001JD001213

Johnson, R. L., Shah, J. J., Cary, R. A., & Huntzicker, J. J. (1981). An Automated Thermal-Optical Method for the Analysis of Carbonaceous Aerosol. In *Atmospheric Aerosol* (Vol. 167, pp. 223–233). AMERICAN CHEMICAL SOCIETY. https://doi.org/10.1021/bk-1981-0167.ch012

Jokinen, T., Sipilä, M., Junninen, H., Ehn, M., Lönn, G., Hakala, J., Petäjä, T., Mauldin, R. L. I., Kulmala, M., & Worsnop, D. R. (2012). Atmospheric sulphuric acid and neutral cluster measurements using CI-APi-TOF. *Atmospheric Chemistry and Physics*, *12*(9), 4117–4125. https://doi.org/10.5194/acp-12-4117-2012

Jordan, A., Haidacher, S., Hanel, G., Hartungen, E., Märk, L., Seehauser, H., Schottkowsky, R., Sulzer, P., & Märk, T. D. (2009). A high resolution and high sensitivity proton-transfer-

reaction time-of-flight mass spectrometer (PTR-TOF-MS). *International Journal of Mass Spectrometry*, *286*(2), 122–128. https://doi.org/10.1016/j.ijms.2009.07.005

Junninen, H., Ehn, M., Petäjä, T., Luosujärvi, L., Kotiaho, T., Kostiainen, R., Rohner, U., Gonin, M., Fuhrer, K., Kulmala, M., & Worsnop, D. R. (2010). A high-resolution mass spectrometer to measure atmospheric ion composition. *Atmospheric Measurement Techniques*, *3*(4), 1039–1053. https://doi.org/10.5194/amt-3-1039-2010

Kenagy, H. S., Heald, C. L., Tahsini, N., Goss, M. B., & Kroll, J. H. (2024). Can we achieve atmospheric chemical environments in the laboratory? An integrated model-measurement approach to chamber SOA studies. *Science Advances*, *10*(37), eado1482. https://doi.org/10.1126/sciadv.ado1482

Ketkar, S. N., Dulak, J. G., Dheandhanoo, S., & Fite, W. L. (1991). Benzene charge exchange at atmospheric pressure for low-level detection of pollutants in ambient air. *Analytica Chimica Acta*, *245*, 267–270. https://doi.org/10.1016/S0003-2670(00)80231-7

Koss, A. R., Canagaratna, M. R., Zaytsev, A., Krechmer, J. E., Breitenlechner, M., Nihill, K. J., Lim, C. Y., Rowe, J. C., Roscioli, J. R., Keutsch, F. N., & Kroll, J. H. (2020). Dimensionality-reduction techniques for complex mass spectrometric datasets: Application to laboratory atmospheric organic oxidation experiments. *Atmospheric Chemistry and Physics*, *20*(2), Article 2. https://doi.org/10.5194/acp-20-1021-2020

Krechmer, J. E., Pagonis, D., Ziemann, P. J., & Jimenez, J. L. (2016). Quantification of Gas-Wall Partitioning in Teflon Environmental Chambers Using Rapid Bursts of Low-Volatility Oxidized Species Generated in Situ. *Environmental Science & Technology*, *50*(11), 5757–5765. https://doi.org/10.1021/acs.est.6b00606

Krechmer, J., Lopez-Hilfiker, F., Koss, A., Hutterli, M., Stoermer, C., Deming, B., Kimmel, J., Warneke, C., Holzinger, R., Jayne, J., Worsnop, D., Fuhrer, K., Gonin, M., & de Gouw, J. (2018). Evaluation of a New Reagent-Ion Source and Focusing Ion–Molecule Reactor for Use in Proton-Transfer-Reaction Mass Spectrometry. *Analytical Chemistry*, *90*(20), Article 20. https://doi.org/10.1021/acs.analchem.8b02641

Kroll, J. H., Donahue, N. M., Jimenez, J. L., Kessler, S. H., Canagaratna, M. R., Wilson, K. R., Altieri, K. E., Mazzoleni, L. R., Wozniak, A. S., Bluhm, H., Mysak, E. R., Smith, J. D., Kolb, C. E., & Worsnop, D. R. (2011). Carbon oxidation state as a metric for describing the chemistry of atmospheric organic aerosol. *Nature Chemistry*, *3*(2), Article 2. https://doi.org/10.1038/nchem.948

Kroll, J. H., Ng, N. L., Murphy, S. M., Flagan, R. C., & Seinfeld, J. H. (2005). Secondary organic aerosol formation from isoprene photooxidation under high-NO conditions. *Geophysical Research Letters*, *32*(18). https://doi.org/10.1029/2005GL023637

Kroll, J. H., Ng, N. L., Murphy, S. M., Flagan, R. C., & Seinfeld, J. H. (2006). Secondary Organic Aerosol Formation from Isoprene Photooxidation. *Environmental Science & Technology*, *40*(6), 1869–1877. https://doi.org/10.1021/es0524301

Landrigan, P. J., Fuller, R., Acosta, N. J. R., Adeyi, O., Arnold, R., Basu, N. (Nil), Baldé, A. B., Bertollini, R., Bose-O'Reilly, S., Boufford, J. I., Breysse, P. N., Chiles, T., Mahidol, C., Coll-Seck, A. M., Cropper, M. L., Fobil, J., Fuster, V., Greenstone, M., Haines, A., … Zhong, M. (2018). The Lancet Commission on pollution and health. *The Lancet*, *391*(10119), Article 10119. https://doi.org/10.1016/S0140-6736(17)32345-0

Lee, B. H., Iyer, S., Kurtén, T., Varelas, J. G., Luo, J., Thomson, R. J., & Thornton, J. A. (2023). Ring-opening yields and auto-oxidation rates of the resulting peroxy radicals from OH-oxidation of α-pinene and β-pinene. *Environmental Science: Atmospheres*, *3*(2), 399–407. https://doi.org/10.1039/D2EA00133K

Lee, B. H., Lopez-Hilfiker, F. D., Mohr, C., Kurtén, T., Worsnop, D. R., & Thornton, J. A. (2014a). An Iodide-Adduct High-Resolution Time-of-Flight Chemical-Ionization Mass Spectrometer: Application to Atmospheric Inorganic and Organic Compounds. *Environmental Science & Technology*, *48*(11), 6309–6317. https://doi.org/10.1021/es500362a

Lee, B. H., Lopez-Hilfiker, F. D., Mohr, C., Kurtén, T., Worsnop, D. R., & Thornton, J. A. (2014b). An Iodide-Adduct High-Resolution Time-of-Flight Chemical-Ionization Mass Spectrometer: Application to Atmospheric Inorganic and Organic Compounds. *Environmental Science & Technology*, *48*(11), Article 11. https://doi.org/10.1021/es500362a

Lee, B. H., Mohr, C., Lopez-Hilfiker, F. D., Lutz, A., Hallquist, M., Lee, L., Romer, P., Cohen, R. C., Iyer, S., Kurtén, T., Hu, W., Day, D. A., Campuzano-Jost, P., Jimenez, J. L., Xu, L., Ng, N. L., Guo, H., Weber, R. J., Wild, R. J., … Thornton, J. A. (2016). Highly functionalized organic nitrates in the southeast United States: Contribution to secondary organic aerosol and reactive nitrogen budgets. *Proceedings of the National Academy of Sciences*, *113*(6), Article 6. https://doi.org/10.1073/pnas.1508108113

Leglise, J., Müller, M., Piel, F., Otto, T., & Wisthaler, A. (2019). Bulk Organic Aerosol Analysis by Proton-Transfer-Reaction Mass Spectrometry: An Improved Methodology for the Determination of Total Organic Mass, O:C and H:C Elemental Ratios, and the Average Molecular Formula. *Analytical Chemistry*, *91*(20), 12619–12624. https://doi.org/10.1021/acs.analchem.9b02949

Li, D., Huang, W., Wang, D., Wang, M., Thornton, J. A., Caudillo, L., Rörup, B., Marten, R., Scholz, W., Finkenzeller, H., Marie, G., Baltensperger, U., Bell, D. M., Brasseur, Z., Curtius, J., Dada, L., Duplissy, J., Gong, X., Hansel, A., … Riva, M. (2024). Nitrate Radicals Suppress Biogenic New Particle Formation from Monoterpene Oxidation. *Environmental Science & Technology*, *58*(3), 1601–1614. https://doi.org/10.1021/acs.est.3c07958

Li, K., Wentzell, J. J. B., Liu, Q., Leithead, A., Moussa, S. G., Wheeler, M. J., Han, C., Lee, P., Li, S.-M., & Liggio, J. (2021). Evolution of Atmospheric Total Organic Carbon from Petrochemical Mixtures. *Environmental Science & Technology*, *55*(19), 12841–12851. https://doi.org/10.1021/acs.est.1c02620

Li, K., Zhang, J., Bell, D. M., Wang, T., Lamkaddam, H., Cui, T., Qi, L., Surdu, M., Wang, D., Du, L., El Haddad, I., Slowik, J. G., & Prevot, A. S. H. (2024). Uncovering the dominant contribution of intermediate volatility compounds in secondary organic aerosol formation from biomass-burning emissions. *National Science Review*, *11*(3), nwae014. https://doi.org/10.1093/nsr/nwae014

Liggio, J., Makar, P., Li, S.-M., Hayden, K., Darlington, A., Moussa, S., Wren, S., Staebler, R., Wentzell, J., Wheeler, M., Leithead, A., Mittermeier, R., Narayan, J., Wolde, M., Blanchard, D., Aherne, J., Kirk, J., Lee, C., Stroud, C., … Gentner, D. R. (2025). Organic carbon dry deposition outpaces atmospheric processing with unaccounted implications

for air quality and freshwater ecosystems. *Science Advances*, *11*(1), eadr0259. https://doi.org/10.1126/sciadv.adr0259

Lindinger, W., & Hansel, A. (1997). Analysis of trace gases at ppb levels by proton transfer reaction mass spectrometry (PTR-MS). *Plasma Sources Science and Technology*, *6*(2), 111. https://doi.org/10.1088/0963-0252/6/2/004

Lindinger, W., Hansel, A., & Jordan, A. (1998). On-line monitoring of volatile organic compounds at pptv levels by means of proton-transfer-reaction mass spectrometry (PTR-MS) medical applications, food control and environmental research. *International Journal of Mass Spectrometry and Ion Processes*, *173*(3), 191–241. https://doi.org/10.1016/S0168-1176(97)00281-4

Liu, F., Joo, T., Ditto, J. C., Saavedra, M. G., Takeuchi, M., Boris, A. J., Yang, Y., Weber, R. J., Dillner, A. M., Gentner, D. R., & Ng, N. L. (2023). Oxidized and Unsaturated: Key Organic Aerosol Traits Associated with Cellular Reactive Oxygen Species Production in the Southeastern United States. *Environmental Science & Technology*, *57*(38), 14150–14161. https://doi.org/10.1021/acs.est.3c03641

Lopez-Hilfiker, F. D., Iyer, S., Mohr, C., Lee, B. H., D'Ambro, E. L., Kurtén, T., & Thornton, J. A. (2016). Constraining the sensitivity of iodide adduct chemical ionization mass spectrometry to multifunctional organic molecules using the collision limit and thermodynamic stability of iodide ion adducts. *Atmospheric Measurement Techniques*, *9*(4), 1505–1512. https://doi.org/10.5194/amt-9-1505-2016

Lopez-Hilfiker, F. D., Mohr, C., Ehn, M., Rubach, F., Kleist, E., Wildt, J., Mentel, T. F., Lutz, A., Hallquist, M., Worsnop, D., & Thornton, J. A. (2014). A novel method for online analysis of gas and particle composition: Description and evaluation of a Filter Inlet for Gases and AEROsols (FIGAERO). *Atmospheric Measurement Techniques*, *7*(4), Article 4. https://doi.org/10.5194/amt-7-983-2014

Lopez-Hilfiker, F. D., Pospisilova, V., Huang, W., Kalberer, M., Mohr, C., Stefenelli, G., Thornton, J. A., Baltensperger, U., Prevot, A. S. H., & Slowik, J. G. (2019). An extractive electrospray ionization time-of-flight mass spectrometer (EESI-TOF) for online measurement of atmospheric aerosol particles. *Atmospheric Measurement Techniques*, *12*(9), Article 9. https://doi.org/10.5194/amt-12-4867-2019

Maris, C., Chung, M. Y., Lueb, R., Krischke, U., Meller, R., Fox, M. J., & Paulson, S. E. (2003). Development of instrumentation for simultaneous analysis of total non-methane organic carbon and volatile organic compounds in ambient air. *Atmospheric Environment*, *37*, 149–158. https://doi.org/10.1016/S1352-2310(03)00387-X

Matsunaga, A., & Ziemann, P. J. (2009). Yields of β-Hydroxynitrates and Dihydroxynitrates in Aerosol Formed from OH Radical-Initiated Reactions of Linear Alkenes in the Presence of NOx. *The Journal of Physical Chemistry A*, *113*(3), 599–606. https://doi.org/10.1021/jp807764d

Mohr, C., Lopez-Hilfiker, F. D., Yli-Juuti, T., Heitto, A., Lutz, A., Hallquist, M., D'Ambro, E. L., Rissanen, M. P., Hao, L., Schobesberger, S., Kulmala, M., Mauldin III, R. L., Makkonen, U., Sipilä, M., Petäjä, T., & Thornton, J. A. (2017). Ambient observations of dimers from terpene oxidation in the gas phase: Implications for new particle formation and growth. *Geophysical Research Letters*, *44*(6), 2958–2966. https://doi.org/10.1002/2017GL072718

Müller, M., Eichler, P., D'Anna, B., Tan, W., & Wisthaler, A. (2017). Direct Sampling and Analysis of Atmospheric Particulate Organic Matter by Proton-Transfer-Reaction Mass Spectrometry. *Analytical Chemistry*, *89*(20), 10889–10897. https://doi.org/10.1021/acs.analchem.7b02582

Murphy, D. M., Cziczo, D. J., Froyd, K. D., Hudson, P. K., Matthew, B. M., Middlebrook, A. M., Peltier, R. E., Sullivan, A., Thomson, D. S., & Weber, R. J. (2006). Single-particle mass spectrometry of tropospheric aerosol particles. *Journal of Geophysical Research: Atmospheres*, *111*(D23). https://doi.org/10.1029/2006JD007340

Mutzel, A., Rodigast, M., Iinuma, Y., Böge, O., & Herrmann, H. (2016). Monoterpene SOA – Contribution of first-generation oxidation products to formation and chemical composition. *Atmospheric Environment*, *130*, 136–144. https://doi.org/10.1016/j.atmosenv.2015.10.080

Nah, T., McVay, R. C., Pierce, J. R., Seinfeld, J. H., & Ng, N. L. (2017). Constraining uncertainties in particle-wall deposition correction during SOA formation in chamber experiments. *Atmospheric Chemistry and Physics*, *17*(3), 2297–2310. https://doi.org/10.5194/acp-17-2297-2017

Ng, N. L., Chhabra, P. S., Chan, A. W. H., Surratt, J. D., Kroll, J. H., Kwan, A. J., McCabe, D. C., Wennberg, P. O., Sorooshian, A., Murphy, S. M., Dalleska, N. F., Flagan, R. C., & Seinfeld, J. H. (2007). Effect of NO_x level on secondary organic aerosol (SOA) formation from the photooxidation of terpenes. *Atmospheric Chemistry and Physics*, *7*(19), 5159–5174. https://doi.org/10.5194/acp-7-5159-2007

Ng, N. L., Kroll, J. H., Chan, A. W. H., Chhabra, P. S., Flagan, R. C., & Seinfeld, J. H. (2007). Secondary organic aerosol formation from *m*-xylene, toluene, and benzene. *Atmospheric Chemistry and Physics*, *7*(14), 3909–3922. https://doi.org/10.5194/acp-7-3909-2007

Nozière, B., & Barnes, I. (1998). Evidence for formation of a PAN analogue of pinonic structure and investigation of its thermal stability. *Journal of Geophysical Research: Atmospheres*, *103*(D19), 25587–25597. https://doi.org/10.1029/98JD01677

Orlando, J. J., & Tyndall, G. S. (2012). Laboratory studies of organic peroxy radical chemistry: An overview with emphasis on recent issues of atmospheric significance. *Chemical Society Reviews*, *41*(19), 6294–6317. https://doi.org/10.1039/C2CS35166H

Pai, S. J., Heald, C. L., Pierce, J. R., Farina, S. C., Marais, E. A., Jimenez, J. L., Campuzano-Jost, P., Nault, B. A., Middlebrook, A. M., Coe, H., Shilling, J. E., Bahreini, R., Dingle, J. H., & Vu, K. (2020). An evaluation of global organic aerosol schemes using airborne observations. *Atmospheric Chemistry and Physics*, *20*(5), Article 5. https://doi.org/10.5194/acp-20-2637-2020

Peeters, J., Nguyen, T. L., & Vereecken, L. (2009). HOx radical regeneration in the oxidation of isoprene. *Physical Chemistry Chemical Physics*, *11*(28), 5935–5939. https://doi.org/10.1039/B908511D

Peng, Y., Wang, H., Gao, Y., Jing, S., Zhu, S., Huang, D., Hao, P., Lou, S., Cheng, T., Huang, C., & Zhang, X. (2023). Real-time measurement of phase partitioning of organic compounds using a proton-transfer-reaction time-of-flight mass spectrometer coupled to a CHARON inlet. *Atmospheric Measurement Techniques*, *16*(1), 15–28. https://doi.org/10.5194/amt-16-15-2023

Peräkylä, O., Berndt, T., Franzon, L., Hasan, G., Meder, M., Valiev, R. R., Daub, C. D., Varelas, J. G., Geiger, F. M., Thomson, R. J., Rissanen, M., Kurtén, T., & Ehn, M. (2023). Large Gas-Phase Source of Esters and Other Accretion Products in the Atmosphere. *Journal of the American Chemical Society*, *145*(14), 7780–7790. https://doi.org/10.1021/jacs.2c10398

Piel, F., Müller, M., Mikoviny, T., Pusede, S. E., & Wisthaler, A. (2019). Airborne measurements of particulate organic matter by proton-transfer-reaction mass spectrometry (PTR-MS): A pilot study. *Atmospheric Measurement Techniques*, *12*(11), 5947–5958. https://doi.org/10.5194/amt-12-5947-2019

Pöschl, U. (2005). Atmospheric Aerosols: Composition, Transformation, Climate and Health Effects. *Angewandte Chemie International Edition*, *44*(46), 7520–7540. https://doi.org/10.1002/anie.200501122

Pospisilova, V., Lopez-Hilfiker, F. D., Bell, D. M., El Haddad, I., Mohr, C., Huang, W., Heikkinen, L., Xiao, M., Dommen, J., Prevot, A. S. H., Baltensperger, U., & Slowik, J. G. (2020). On the fate of oxygenated organic molecules in atmospheric aerosol particles. *Science Advances*, *6*(11), Article 11. https://doi.org/10.1126/sciadv.aax8922

Pozzer, A., Anenberg, S. C., Dey, S., Haines, A., Lelieveld, J., & Chowdhury, S. (2023). Mortality Attributable to Ambient Air Pollution: A Review of Global Estimates. *GeoHealth*, *7*(1), e2022GH000711. https://doi.org/10.1029/2022GH000711

Presto, A. A., Huff Hartz, K. E., & Donahue, N. M. (2005). Secondary Organic Aerosol Production from Terpene Ozonolysis. 2. Effect of NOx Concentration. *Environmental Science & Technology*, *39*(18), 7046–7054. https://doi.org/10.1021/es050400s

Presto, A. A., Miracolo, M. A., Kroll, J. H., Worsnop, D. R., Robinson, A. L., & Donahue, N. M. (2009). Intermediate-Volatility Organic Compounds: A Potential Source of Ambient Oxidized Organic Aerosol. *Environmental Science & Technology*, *43*(13), 4744–4749. https://doi.org/10.1021/es803219q

Price, D. J., Day, D. A., Pagonis, D., Stark, H., Algrim, L. B., Handschy, A. V., Liu, S., Krechmer, J. E., Miller, S. L., Hunter, J. F., de Gouw, J. A., Ziemann, P. J., & Jimenez, J. L. (2019). Budgets of Organic Carbon Composition and Oxidation in Indoor Air. *Environmental Science & Technology*, *53*(22), 13053–13063. https://doi.org/10.1021/acs.est.9b04689

Pye, H. O. T., Chan, A. W. H., Barkley, M. P., & Seinfeld, J. H. (2010). Global modeling of organic aerosol: The importance of reactive nitrogen (NO_x and NO_3). *Atmospheric Chemistry and Physics*, *10*(22), 11261–11276. https://doi.org/10.5194/acp-10-11261-2010

Pye, H. O. T., Ward-Caviness, C. K., Murphy, B. N., Appel, K. W., & Seltzer, K. M. (2021). Secondary organic aerosol association with cardiorespiratory disease mortality in the United States. *Nature Communications*, *12*(1), 7215. https://doi.org/10.1038/s41467-021-27484-1

Reinecke, T., Leiminger, M., Klinger, A., & Müller, M. (2024). Direct detection of polycyclic aromatic hydrocarbons on a molecular composition level in summertime ambient aerosol via proton transfer reaction mass spectrometry. *Aerosol Research*, *2*(2), 225–233. https://doi.org/10.5194/ar-2-225-2024

Rissanen, M. P., Mikkilä, J., Iyer, S., & Hakala, J. (2019). Multi-scheme chemical ionization inlet (MION) for fast switching of reagent ion chemistry in atmospheric pressure chemical ionization mass spectrometry (CIMS) applications. *Atmospheric Measurement Techniques*, *12*(12), 6635–6646. https://doi.org/10.5194/amt-12-6635-2019

Riva, M., Rantala, P., Krechmer, J. E., Peräkylä, O., Zhang, Y., Heikkinen, L., Garmash, O., Yan, C., Kulmala, M., Worsnop, D., & Ehn, M. (2019). Evaluating the performance of five different chemical ionization techniques for detecting gaseous oxygenated organic species. *Atmospheric Measurement Techniques*, *12*(4), 2403–2421. https://doi.org/10.5194/amt-12-2403-2019

Roberts, J. M., Bertman, S. B., Jobson, T., Niki, H., & Tanner, R. (1998). Measurement of total nonmethane organic carbon (Cy): Development and application at Chebogue Point, Nova Scotia, during the 1993 North Atlantic Regional Experiment campaign. *Journal of Geophysical Research: Atmospheres*, *103*(D11), 13581–13592. https://doi.org/10.1029/97JD02240

Safieddine, S. A., Heald, C. L., & Henderson, B. H. (2017). The global nonmethane reactive organic carbon budget: A modeling perspective. *Geophysical Research Letters*, *44*(8), Article 8. https://doi.org/10.1002/2017GL072602

Salo, V.-T., Valiev, R., Lehtola, S., & Kurtén, T. (2022). Gas-Phase Peroxyl Radical Recombination Reactions: A Computational Study of Formation and Decomposition of Tetroxides. *The Journal of Physical Chemistry A*, *126*(25), 4046–4056. https://doi.org/10.1021/acs.jpca.2c01321

Salvador, C. M., Ho, T.-T., Chou, C. C.-K., Chen, M.-J., Huang, W.-R., & Huang, S.-H. (2016). Characterization of the organic matter in submicron urban aerosols using a Thermo-Desorption Proton-Transfer-Reaction Time-of-Flight Mass Spectrometer (TD-PTR-TOF-MS). *Atmospheric Environment*, *140*, 565–575. https://doi.org/10.1016/j.atmosenv.2016.06.029

Sanchez, J., Tanner, D. J., Chen, D., Huey, L. G., & Ng, N. L. (2016). A new technique for the direct detection of HO_2 radicals using bromide chemical ionization mass spectrometry (Br-CIMS): Initial characterization. *Atmospheric Measurement Techniques*, *9*(8), 3851–3861. https://doi.org/10.5194/amt-9-3851-2016

Schervish, M., & Donahue, N. M. (2021). Peroxy radical kinetics and new particle formation. *Environmental Science: Atmospheres*, *1*(2), 79–92. https://doi.org/10.1039/D0EA00017E

Shen, H., Vereecken, L., Kang, S., Pullinen, I., Fuchs, H., Zhao, D., & Mentel, T. F. (2022). Unexpected significance of a minor reaction pathway in daytime formation of biogenic highly oxygenated organic compounds. *Science Advances*, *8*(42), eabp8702. https://doi.org/10.1126/sciadv.abp8702

Shrivastava, M., Cappa, C. D., Fan, J., Goldstein, A. H., Guenther, A. B., Jimenez, J. L., Kuang, C., Laskin, A., Martin, S. T., Ng, N. L., Petaja, T., Pierce, J. R., Rasch, P. J., Roldin, P., Seinfeld, J. H., Shilling, J., Smith, J. N., Thornton, J. A., Volkamer, R., … Zhang, Q. (2017). Recent advances in understanding secondary organic aerosol: Implications for global climate forcing. *Reviews of Geophysics*, *55*(2), 509–559. https://doi.org/10.1002/2016RG000540

Singh, H. B., & Hanst, P. L. (1981). Peroxyacetyl nitrate (PAN) in the unpolluted atmosphere: An important reservoir for nitrogen oxides. *Geophysical Research Letters*, *8*(8), 941–944. https://doi.org/10.1029/GL008i008p00941

Solomon, P. A., & Sioutas, C. (2008). Continuous and Semicontinuous Monitoring Techniques for Particulate Matter Mass and Chemical Components: A Synthesis of Findings from EPA's Particulate Matter Supersites Program and Related Studies. *Journal of the Air &*

Waste Management Association, *58*(2), 164–195. https://doi.org/10.3155/1047-3289.58.2.164

Song, J., Gkatzelis, G. I., Tillmann, R., Brüggemann, N., Leisner, T., & Saathoff, H. (2024). Characterization of biogenic volatile organic compounds and their oxidation products in a stressed spruce-dominated forest close to a biogas power plant. *Atmospheric Chemistry and Physics*, *24*(23), 13199–13217. https://doi.org/10.5194/acp-24-13199-2024

Song, J., Saathoff, H., Jiang, F., Gao, L., Zhang, H., & Leisner, T. (2024). Sources of organic gases and aerosol particles and their roles in nighttime particle growth at a rural forested site in southwest Germany. *Atmospheric Chemistry and Physics*, *24*(11), 6699–6717. https://doi.org/10.5194/acp-24-6699-2024

Stockwell, C. E., Kupc, A., Witkowski, B., Talukdar, R. K., Liu, Y., Selimovic, V., Zarzana, K. J., Sekimoto, K., Warneke, C., Washenfelder, R. A., Yokelson, R. J., Middlebrook, A. M., & Roberts, J. M. (2018). Characterization of a catalyst-based conversion technique to measure total particulate nitrogen and organic carbon and comparison to a particle mass measurement instrument. *Atmospheric Measurement Techniques*, *11*(5), 2749–2768. https://doi.org/10.5194/amt-11-2749-2018

Sulbaek Andersen, M. P., Hurley, M. D., Wallington, T. J., Ball, J. C., Martin, J. W., Ellis, D. A., & Mabury, S. A. (2003). Atmospheric chemistry of C2F5CHO: Mechanism of the C2F5C(O)O2 + HO2 reaction. *Chemical Physics Letters*, *381*(1), 14–21. https://doi.org/10.1016/j.cplett.2003.09.085

Sunner, Jan., Nicol, Gordon., & Kebarle, Paul. (1988). Factors determining relative sensitivity of analytes in positive mode atmospheric pressure ionization mass spectrometry. *Analytical Chemistry*, *60*(13), 1300–1307. https://doi.org/10.1021/ac00164a012

Surratt, J. D., Murphy, S. M., Kroll, J. H., Ng, N. L., Hildebrandt, L., Sorooshian, A., Szmigielski, R., Vermeylen, R., Maenhaut, W., Claeys, M., Flagan, R. C., & Seinfeld, J. H. (2006). Chemical Composition of Secondary Organic Aerosol Formed from the Photooxidation of Isoprene. *The Journal of Physical Chemistry A*, *110*(31), 9665–9690. https://doi.org/10.1021/jp061734m

Takeuchi, M., & Ng, N. L. (2019). Chemical composition and hydrolysis of organic nitrate aerosol formed from hydroxyl and nitrate radical oxidation of *α*-pinene and *β*-pinene. *Atmospheric Chemistry and Physics*, *19*(19), Article 19. https://doi.org/10.5194/acp-19-12749-2019

Tan, W., Zhu, L., Mikoviny, T., Nielsen, C. J., Tang, Y., Wisthaler, A., Eichler, P., Müller, M., D'Anna, B., Farren, N. J., Hamilton, J. F., Pettersson, J. B. C., Hallquist, M., Antonsen, S., & Stenstrøm, Y. (2021). Atmospheric Chemistry of 2-Amino-2-methyl-1-propanol: A Theoretical and Experimental Study of the OH-Initiated Degradation under Simulated Atmospheric Conditions. *The Journal of Physical Chemistry A*, *125*(34), 7502–7519. https://doi.org/10.1021/acs.jpca.1c04898

Teng, A. P., Crounse, J. D., & Wennberg, P. O. (2017). Isoprene Peroxy Radical Dynamics. *Journal of the American Chemical Society*, *139*(15), 5367–5377. https://doi.org/10.1021/jacs.6b12838

Thompson, S. L., Yatavelli, R. L. N., Stark, H., Kimmel, J. R., Krechmer, J. E., Day, D. A., Hu, W., Isaacman-VanWertz, G., Yee, L., Goldstein, A. H., Khan, M. A. H., Holzinger, R., Kreisberg,

N., Lopez-Hilfiker, F. D., Mohr, C., Thornton, J. A., Jayne, J. T., Canagaratna, M., Worsnop, D. R., & Jimenez, J. L. (2017). Field intercomparison of the gas/particle partitioning of oxygenated organics during the Southern Oxidant and Aerosol Study (SOAS) in 2013. *Aerosol Science and Technology*, *51*(1), 30–56. https://doi.org/10.1080/02786826.2016.1254719

Timkovsky, J., Chan, A. W. H., Dorst, T., Goldstein, A. H., Oyama, B., & Holzinger, R. (2015). Comparison of advanced offline and in situ techniques of organic aerosol composition measurement during the CalNex campaign. *Atmospheric Measurement Techniques*, *8*(12), 5177–5187. https://doi.org/10.5194/amt-8-5177-2015

Tomas, A., Villenave, E., & Lesclaux, R. (2001). Reactions of the HO2 Radical with CH3CHO and CH3C(O)O2 in the Gas Phase. *The Journal of Physical Chemistry A*, *105*(14), 3505–3514. https://doi.org/10.1021/jp003762p

Veres, P., Gilman, J. B., Roberts, J. M., Kuster, W. C., Warneke, C., Burling, I. R., & de Gouw, J. (2010). Development and validation of a portable gas phase standard generation and calibration system for volatile organic compounds. *Atmospheric Measurement Techniques*, *3*(3), Article 3. https://doi.org/10.5194/amt-3-683-2010

Veres, P., Roberts, J. M., Warneke, C., Welsh-Bon, D., Zahniser, M., Herndon, S., Fall, R., & de Gouw, J. (2008). Development of negative-ion proton-transfer chemical-ionization mass spectrometry (NI-PT-CIMS) for the measurement of gas-phase organic acids in the atmosphere. *International Journal of Mass Spectrometry*, *274*(1), 48–55. https://doi.org/10.1016/j.ijms.2008.04.032

Vogel, A. L., Schneider, J., Müller-Tautges, C., Phillips, G. J., Pöhlker, M. L., Rose, D., Zuth, C., Makkonen, U., Hakola, H., Crowley, J. N., Andreae, M. O., Pöschl, U., & Hoffmann, T. (2016). Aerosol Chemistry Resolved by Mass Spectrometry: Linking Field Measurements of Cloud Condensation Nuclei Activity to Organic Aerosol Composition. *Environmental Science & Technology*, *50*(20), 10823–10832. https://doi.org/10.1021/acs.est.6b01675

Wolfe, G. M., Marvin, M. R., Roberts, S. J., Travis, K. R., & Liao, J. (2016). The Framework for 0-D Atmospheric Modeling (F0AM) v3.1. *Geoscientific Model Development*, *9*(9), 3309–3319. https://doi.org/10.5194/gmd-9-3309-2016

Xin, X., Zhao, Y., Wan, Y., Zhang, H., & Yu, H. (2024). Molecular composition of organic aerosols in urban and marine atmosphere: A comparison study using FIGAERO-I-CIMS, ESI-FT-ICR MS, and GC × GC-EI-ToF-MS. *Aerosol Science and Technology*, *58*(10), 1142–1156. https://doi.org/10.1080/02786826.2024.2377394

Xu, L., Møller, K. H., Crounse, J. D., Otkjær, R. V., Kjaergaard, H. G., & Wennberg, P. O. (2019). Unimolecular Reactions of Peroxy Radicals Formed in the Oxidation of α-Pinene and β-Pinene by Hydroxyl Radicals. *The Journal of Physical Chemistry A*, *123*(8), 1661–1674. https://doi.org/10.1021/acs.jpca.8b11726

Yang, H., Raucci, U., Iyer, S., Hasan, G., Golin Almeida, T., Barua, S., Savolainen, A., Kangasluoma, J., Rissanen, M., Vehkamäki, H., & Kurtén, T. (2025). Molecular dynamics-guided reaction discovery reveals endoperoxide-to-alkoxy radical isomerization as key branching point in α-pinene ozonolysis. *Nature Communications*, *16*(1), 661. https://doi.org/10.1038/s41467-025-55985-w

Yang, M., & Fleming, Z. L. (2019). Estimation of atmospheric total organic carbon (TOC) – paving the path towards carbon budget closure. *Atmospheric Chemistry and Physics*, *19*(1), Article 1. https://doi.org/10.5194/acp-19-459-2019

Ye, Q., Goss, M. B., Krechmer, J. E., Majluf, F., Zaytsev, A., Li, Y., Roscioli, J. R., Canagaratna, M., Keutsch, F. N., Heald, C. L., & Kroll, J. H. (2022). Product distribution, kinetics, and aerosol formation from the OH oxidation of dimethyl sulfide under different RO_2 regimes. *Atmospheric Chemistry and Physics*, *22*(24), 16003–16015. https://doi.org/10.5194/acp-22-16003-2022

Ye, Q., Krechmer, J. E., Shutter, J. D., Barber, V. P., Li, Y., Helstrom, E., Franco, L. J., Cox, J. L., Hrdina, A. I. H., Goss, M. B., Tahsini, N., Canagaratna, M., Keutsch, F. N., & Kroll, J. H. (2021). Real-Time Laboratory Measurements of VOC Emissions, Removal Rates, and Byproduct Formation from Consumer-Grade Oxidation-Based Air Cleaners. *Environmental Science & Technology Letters*. https://doi.org/10.1021/acs.estlett.1c00773

Ye, Q., Wang, M., Hofbauer, V., Stolzenburg, D., Chen, D., Schervish, M., Vogel, A., Mauldin, R. L., Baalbaki, R., Brilke, S., Dada, L., Dias, A., Duplissy, J., El Haddad, I., Finkenzeller, H., Fischer, L., He, X., Kim, C., Kürten, A., … Donahue, N. M. (2019). Molecular Composition and Volatility of Nucleated Particles from α-Pinene Oxidation between −50 °C and +25 °C. *Environmental Science & Technology*, *53*(21), 12357–12365. https://doi.org/10.1021/acs.est.9b03265

Ye, R., Furlani, T. C., Folkerson, A. P., Mabury, S. A., VandenBoer, T. C., & Young, C. J. (2024). A Method to Measure Total Gaseous Fluorine. *Environmental Science & Technology Letters*, *11*(10), 1062–1067. https://doi.org/10.1021/acs.estlett.4c00553

Yeh, G. K., & and Ziemann, P. J. (2015). Gas-Wall Partitioning of Oxygenated Organic Compounds: Measurements, Structure–Activity Relationships, and Correlation with Gas Chromatographic Retention Factor. *Aerosol Science and Technology*, *49*(9), 727–738. https://doi.org/10.1080/02786826.2015.1068427

Zaytsev, A., Breitenlechner, M., Koss, A. R., Lim, C. Y., Rowe, J. C., Kroll, J. H., & Keutsch, F. N. (2019). Using collision-induced dissociation to constrain sensitivity of ammonia chemical ionization mass spectrometry (NH4+CIMS) to oxygenated volatile organic compounds. *Atmospheric Measurement Techniques*, *12*(3), Article 3. https://doi.org/10.5194/amt-12-1861-2019

Zaytsev, A., Koss, A. R., Breitenlechner, M., Krechmer, J. E., Nihill, K. J., Lim, C. Y., Rowe, J. C., Cox, J. L., Moss, J., Roscioli, J. R., Canagaratna, M. R., Worsnop, D. R., Kroll, J. H., & Keutsch, F. N. (2019). Mechanistic study of the formation of ring-retaining and ring-opening products from the oxidation of aromatic compounds under urban atmospheric conditions. *Atmospheric Chemistry and Physics*, *19*(23), 15117–15129. https://doi.org/10.5194/acp-19-15117-2019

Zhang, Q., Jimenez, J. L., Canagaratna, M. R., Allan, J. D., Coe, H., Ulbrich, I., Alfarra, M. R., Takami, A., Middlebrook, A. M., Sun, Y. L., Dzepina, K., Dunlea, E., Docherty, K., DeCarlo, P. F., Salcedo, D., Onasch, T., Jayne, J. T., Miyoshi, T., Shimono, A., … Worsnop, D. R. (2007). Ubiquity and dominance of oxygenated species in organic aerosols in anthropogenically-influenced Northern Hemisphere midlatitudes. *Geophysical Research Letters*, *34*(13). https://doi.org/10.1029/2007GL029979

Zhao, J., Mickwitz, V., Luo, Y., Häkkinen, E., Graeffe, F., Zhang, J., Timonen, H., Canagaratna, M., Krechmer, J. E., Zhang, Q., Kulmala, M., Kangasluoma, J., Worsnop, D., & Ehn, M. (2024). Characterization of the Vaporization Inlet for Aerosols (VIA) for online measurements of particulate highly oxygenated organic molecules (HOMs). *Atmospheric Measurement Techniques*, *17*(5), 1527–1543. https://doi.org/10.5194/amt-17-1527-2024

Ziemann, P. J., & Atkinson, R. (2012). Kinetics, products, and mechanisms of secondary organic aerosol formation. *Chemical Society Reviews*, *41*(19), 6582–6605. https://doi.org/10.1039/C2CS35122F